Development of a Terrain Pre-filtering Technique applicable to Probabilistic Terrain using Constraint Mode Tire Model

Rui Ma

Dissertation submitted to faculty of Virginia Polytechnic Institute and State University in partial fulfillment of the requirements for the degree of

Doctor of Philosophy

In

Mechanical Engineering

John B. Ferris

Saied Taheri

Corina Sandu

Robert L. West

Scott L. Hendricks

September 13, 2013

Blacksburg, VA

Keywords: Terrain, Gridding, Stochastic, Tire Model, Pre-filtering

Development of a Terrain Pre-filtering Technique applicable to Probabilistic Terrain using Constraint Mode Tire Model

Rui Ma

Abstract

The vertical force generated from terrain-tire interaction has long been of interest for vehicle dynamic simulations and chassis development. As the terrain serves as the main excitation to the suspension system through pneumatic tire, proper terrain and tire models are required to produce reliable vehicle response. Due to the high complexity of the tire structure and the immense size of a high fidelity terrain profile, it is not efficient to calculate the terrain-tire interaction at every location. The use of a simpler tire model (e.g. point follower tire model) and a pre-filtered terrain profile as equivalent input will considerably reduce the simulation time. The desired produced responses would be nearly identical to the ones using a complex tire model and unfiltered terrain, with a significant computational efficiency improvement.

In this work, a terrain pre-filtering technique is developed to improve simulation efficiency while still providing reliable load prediction. The work is divided into three parts. First a stochastic gridding method is developed to include the measurement uncertainties in the gridded terrain profile used as input to the vehicle simulation. The obtained uniformly spaced terrain is considered probabilistic, with a series of gridding nodes with heights represented by random variables. Next, a constraint mode tire model is proposed to emulate the tire radial displacement and the corresponding force given the terrain excitation. Finally, based on the constraint mode tire model, the pre-filtering technique is developed. At each

location along the tire's path, the tire center height is adjusted until the spindle load reaches a pre-designated constant load. The resultant tire center trajectory is the pre-filtered terrain profile and serves as an equivalent input to the simple tire model. The vehicle response produced by using the pre-filtered terrain profile and the simple tire model is analyzed for accuracy assessment. The computational efficiency improvement is also examined. The effectiveness of the pre-filtering technique is validated on probabilistic terrain by using different realizations of terrain profiles. It is shown through multiple profiles that the computational efficiency can be improved by three orders of magnitude with no statistically significant change in resulting loading.

Acknowledgements

First of all, I would like to express my deepest appreciation to my advisor, Dr. John B. Ferris, not only for his excellent academic guidance which makes this dissertation possible, but also for his continuous support, encouragement and patience over the last four years. His mentorship, like a torch, leads me through the graduate school and helps me find my research interest and future career path. I am deeply grateful for the opportunity to work with him. Thank you to all of my committee members, Dr. Taheri, Dr. Sandu, Dr. West and Dr. Hendricks for your time and advices helping me to finish the work.

Special acknowledgement to Chrysler and the Automotive Research Center (ARC), a U.S. Army center of excellence in modeling and simulation of ground vehicles, for their generous sponsorship for our research in Vehicle Terrain Performance Lab. Thank you Professor Schalk Els of the University of Pretoria for providing the tire experimental data used in this work.

Thank you to all my colleges in Vehicle Terrain Performance Lab. It is a pleasure to work with all of you. More thanks to my friends, whose support and encouragement always cheer me up. Specially, I would like to express gratitude to Dr. Yimin Gao for his insightful help on vehicle dynamics theory, and Mr. Lichen Song for his support on mathematics.

Finally I would like to express my sincerest gratefulness to my parents, for their unstopping support and understanding. They are the most important motivation in my life to keep me going forward towards my goal, no matter how rough the way is.

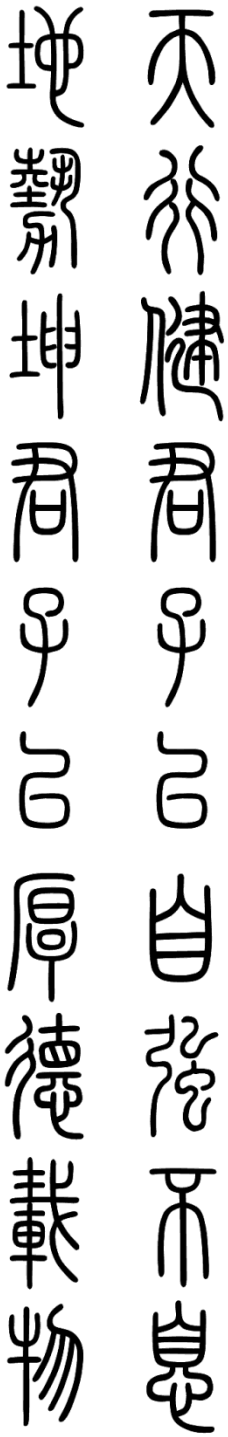
天行健君子以自強不息
地勢坤君子以厚德載物

Contents

List of Figures

List of Tables

Nomenclature

Parameter	Definition
κ	Radial spring rate density (F/m)
u	Radial deflection (m)
R	Undeflected tire radius (m)
F_n	Radial force acting on one single tire segment (N)
N	Total number of tire segments
f	Linear distributed load density (N/m)
l	Circumferential length of one tire segment ($l = \frac{2\pi R}{n}$) (m)
U_b	Bending potential energy of each tire segment (J)
M	Bending moment of each tire segment (Nm)
E	Elastic modulus (Pa)
I	Second moment of area for each tire segment (m^4)
ρ	Linear mass density (kg/m)
γ	Shear strain

U_s	Shear potential energy for each tire segment (J)
G	Shear modulus (Pa)
b	Width of one tire segment (m)
h	Thickness of one tire segment (m)
U_e	Elastic potential energy for each tire segment (J)
U_w	External work on each tire segment (J)
m	Total vehicle mass (kg)
m_s	Sprung mass (kg)
m_{us}	Unsprung mass of each wheel assembly (kg)
$k_{s,f}$	Front suspension stiffness (N/m)
$k_{s,r}$	Rear suspension stiffness (N/m)
k_t	Tire stiffness (N/m)
c_f	Damping coefficient front suspension N/(m/s)
c_r	Damping coefficient rear suspension N/(m/s)
a	Distance front axle to center of mass (m)

b	Distance rear axle to center of mass (m)
t_f	Track width front axle (m)
t_r	Track width rear axle (m)
I_p	Pitch inertia (kg-m2)
I_r	Roll inertia (kg-m2)
θ_s	Vehicle Pitch (rad)
ϕ_s	Vehicle Roll (rad)
z_s	Sprung Mass Displacement (m)
$z_{u,fr}$	Unsprung Mass Displacement (Front, Right) (m)
$z_{u,fl}$	Unsprung Mass Displacement (Front, Left) (m)
$z_{u,rr}$	Unsprung Mass Displacement (Rear, Right) (m)
$z_{u,rl}$	Unsprung Mass Displacement (Rear, Left) (m)
$z_{0,fr}$	Terrain Excitation (Front, Right) (m)
$z_{0,fl}$	Terrain Excitation (Front, Left) (m)
$z_{0,rr}$	Terrain Excitation (Rear, Right) (m)

$z_{0,rl}$	Terrain Excitation (Rear, Left) (m)

1. Introduction

1.1 Motivation

Chassis loads that represent severe customer usage are necessary throughout the vehicle design and development process to help the vehicle meet its performance and reliability objectives. Engineers are challenged with predicting these loads during early stages in the design process. However the true loads are available only at the conclusion of the program when the design is complete and it is difficult and expensive to make modifications. The difficulties in predicting these loads are exacerbated by the design process itself; the loads change as the design of the vehicle progresses. Therefore invariant excitations to the chassis are desirable as it makes the design process more tractable [1-6]. The main excitation to the vehicle is the terrain [7] to which the vehicle responds by developing forces, moments, etc. Since terrain features influence the suspension system through the tires, research on tire-terrain interaction is the basis to provide reliable load estimations to shorten the vehicle development time and reduce overall cost. Knowledge of the terrain should be applied in conjunction with compliant tire model in the vehicle dynamic simulation for suspension load estimation. Therefore it is advantageous to develop a computationally efficient yet accurate chassis simulation method to provide the designer with load information early in the design stages.

For reliability analysis and component fatigue calculations, vehicle dynamic simulations are performed over long and rough proving terrain profiles. The bridging and enveloping properties of the tire are important and cannot be neglected. Due to the complexity of the tire, it is time consuming to conduct the vehicle dynamic simulation coupled with a complex tire model over the proving terrain profile. An alternative method to accelerate the process with acceptable accuracy loss is to introduce an "Effective Road Profile". It serves as an input to a simplified tire model, such as the point follower tire model. The

effective road profile is generally a pre-filtered undulation trajectory from the original terrain profile. The bridging and enveloping properties are addressed through the offline pre-filtering process instead of the tire system. The usage of an effective profile coupled with a simplified tire model greatly improves the computational efficiency, but the issue of accuracy must be addressed.

1.2 Thesis statement

The thesis of this work is that an effective terrain pre-filtering technique based on a constraint mode tire model can be developed that is applicable to both deterministic and probabilistic terrain such that simple tire models can be used to predict spindle loads with high computational efficiency and no statistically significant accuracy loss.

1.3 Contributions

The following are the original contributions to the state-of-the-art that are developed in this work:

1. A stochastic gridding method to obtain the uniformly spaced probabilistic terrain

   The stochastic gridding method is developed to convert the measured irregularly spaced terrain points into a uniformly spaced format for storage and simulation efficiency purposes. This method is developed with the measurement uncertainty in the horizontal plane taken into consideration. The obtained terrain profile comprises a series of regularly spaced nodes and the corresponding heights as random variables. Different realizations can be generated using the marginal probability distribution functions and the dependency relationship between node heights provided by the stochastic gridding method.

2. A novel parameterization of a tire model whose radial deformation is represented by a set of constraint modes is developed such that it is completely parameterized by one overall stiffness parameter and two shape parameters. A region of admissible values for the shape parameters is developed as is a method for identifying these parameter values for a specific tire.

   A planar tire model is discretized into segments and modeled as consecutive Euler beams. The quasi-static constraint modes of the tire model are used to predict the tire deformation and the vertical spindle force. In this novel derivation, the final equation of motion is reduced to three parameters. The parameters are decoupled as an overall stiffness parameter and two shape parameters. A system identification process based on flat plate and cleat test result to calibrate the parameters is proposed. The admissible region of the shape parameters to determine the static tire shape is proposed. An parameter adjustment procedure is also provided to tune the tire parameters for different applications with different accuracy requirement. The model is validated with experimental results in terms of circumferential deformation and vertical force estimation.

3. A terrain pre-filtering technique that provides an equivalent terrain profile to a simplified tire model that results in an increase in computational efficiency of nearly three orders of magnitude without any statistically significant change in accuracy.

   The terrain pre-filtering technique is developed based on the constraint mode tire model to provide an equivalent terrain profile input to a simplified tire model to improve the simulation efficiency. At every location, the constraint mode tire model is assumed to convey a constant static load. The tire center height is adjusted until the spindle load reaches the pre-designated load. The trajectory of the tire center height undulation is considered to be the equivalent terrain profile. It is used as an input to a simplified tire model in the vehicle dynamic simulation. The computational efficiency increases about three orders of magnitude, without any statistically

significant change in accuracy. The pre-filtering technique can also be applied on probabilistic terrain, given the corresponding realizations.

1.4 Dissertation Outline

The work is organized as follows. First the literature about terrain measurement methods and data configurations, existing gridding methods, previous effective terrain profile computational algorithm, tire models concerned with radial deformation and stochastic terrain models is reviewed in chapter 2. In chapter 3, the stochastic gridding method and the concept of probabilistic terrain is developed. The cloud of irregularly spaced points computed directly from the laser profiler is gridded stochastically and the resultant terrain heights are represented by regular spaced random variables. The dependency between the adjacent nodal heights is defined and realizations of probabilistic terrain profiles are generated. In chapter 4, a constraint mode tire model is developed to capture the radial deformation given unilateral road constraints. The parameter identification process is provided to apply the model to different tires. Finally in chapter 5, a terrain pre-filtering technique based on constraint mode tire model is developed to improve the vehicle dynamic simulation efficiency and provide accurate spindle load estimation. The terrain pre-filtering technique can be applied either on deterministic terrain or probabilistic terrain (as developed in chapter 3).

1.5 Publications

Ma, R., Chemistruck, Heather., Ferris, John B.. State-of-the-art of terrain profile characterization models. International Journal of Vehicle Design, 2013. 61(1-4): p. 285 - 304 (20)

Ma, R. and J.B. Ferris, Terrain gridding using a stochastic weighting function, in ASME 2011 Dynamic Systems and Control Conference and Bath/ASME Symposium on Fluid Power and Motion Control (DSCC2011) 2011: October 31–November 2, 2011 , Arlington, Virginia, USA p. 375-381

Ma, R., A.A. Reid, and J.B. Ferris. *Capturing Plannar Tire Properties Using Static Constraint Modes*. Dynamic Systems and Control Conference and Bath/ASME Symposium on Fluid Power and Motion Control, 2012 October, Fort Lauderdale, FL.

Ma, R., A.A. Reid, Gorsich, D., and J.B. Ferris. *The Development of Constraint Mode Tire Model*. To be submitted to International Journal of Vehicle Design

Ma, R., and J.B. Ferris. *The Development of Terrain Pre-filtering technique based on Constraint Mode Tire Model*. To be submitted to SAE Congress 2014

2. Review of Literature

This chapter provides a literature review of previous contributions in terrain modeling, effective profile computation and tire modeling. First the terrain measurement methods and the coordinate system are introduced to provide a background of terrain measurement techniques and the resultant terrain surface data configuration. Next the gridding methods that convert the irregularly spaced data into regular spacing are provided. The review of previous stochastic terrain model follows. Then the tire models focusing on the radial deformation are discussed. Finally the survey on previous work to compute the effective road profile is presented.

2.1 Terrain Measurement

Terrain measurement technology has progressed from vehicle-response systems [8, 9] to vehicle-independent systems [10-14]. The vehicle-response system measures the terrain profile elevation based on transducers which sense the relative movement between the body and the ground, as shown in Figure 2.1 [15]. However, the accuracy of the method is highly dependent on the specific vehicle used, and in most cases the result has already been filtered by the whole vehicle system, including the tire and suspension models. The calibration and stability of the measuring system may also cause problems. Therefore, the data are typically used to study response of a particular vehicle to the terrain rather than drawing general conclusions.

Figure 2.1. ATC profiler: example of vehicle response measurement system [15]

The direct measurement method has been developed to address the limitations of response-type measurement systems. In the 1960s, General Motors Research (GMR) developed a high speed inertial profiler [16]. This profiler used a road-following wheel that extended below the body of either a vehicle or a trailer to which a linear potentiometer was attached to measure the relative distance between the body and the road surface. An accelerometer was attached to the body and the output signal is integrated twice to estimate the vertical position of the body in the established inertial reference frame. The difference of the two signals is the resulting road profile. The main drawback is that it only captures data in the frequency range corresponding to vehicle ride: the high frequency content is filtered by the mechanical system such as the tires. The low frequency content does not cause suspension travel and therefore cannot be detected by the potentiometer.

In 1987, the Australian Road Research Board (ARRB) introduced a laser-based highway-speed road profile measuring system [17], where the terrain is sampled optically, rather than mechanically as was the standard practice. Many advances were made because of this essential change, yet considerable research is required to understand the full implications of this shift. For example, the laser has a much finer resolution than the tire contact patch. It is capable of detecting small localized disturbances that would be enveloped or bridged by the tire; this problem had not surfaced previously because the tire in vehicle-response systems had acted as a mechanical filter between the terrain surface and vehicle chassis. The ARRB measuring system used a single-axis accelerometer to eliminate host vehicle dynamics in the vertical direction, but no other directions [18].

Currently, 3D terrain surface measurement systems as shown in Figure 2.2 obtain millimeter precision measurements across a four meter wide transverse path (encompassing both tire paths) [12, 14, 19]. These systems consist of a scanning laser and the some combination of an inertial navigation system, accelerometers, and a distance measurement instrument to track the position and orientation of the scanning laser in space. Typically, the scanning laser is affixed to the mounting structure at the rear of the vehicle. The vehicle motion is subtracted from the laser data to obtain the terrain height. These 3D scanners are capable of capturing both small localized disturbances that may affect friction and noise and disturbances that excite the vehicle chassis. Therefore the obtained terrain surface can be used as a input to vehicle dynamic simulation to accurately emulate the vehicle response [20].

Figure 2.2. Optical terrain measurement system with inertial navigator

2.2. Gridding Method

2.2.1 Defining a Curved Regular Grid in the Horizontal Plane

This terrain measurement system shown in Figure 2.2 collects data transversely through the application of a rotating prism [12, 21, 22]. As shown in Figure 2.3, the data are collected with an equal angle of rotation, not equal transverse spacing. Therefore the scanned points are more densely spaced near the center line directly below the laser. When vertical undulations are present, transverse spacing between points is not consistent (shown as the difference in transverse spacing between x_2 and x_1 versus between x_3 and x_2 in Figure 2.3). In the longitudinal direction, the spacing is dependent on the speed of the host vehicle and the scanning frequency. The pitch and roll motion of the vehicle also influence the spacing uniformity.

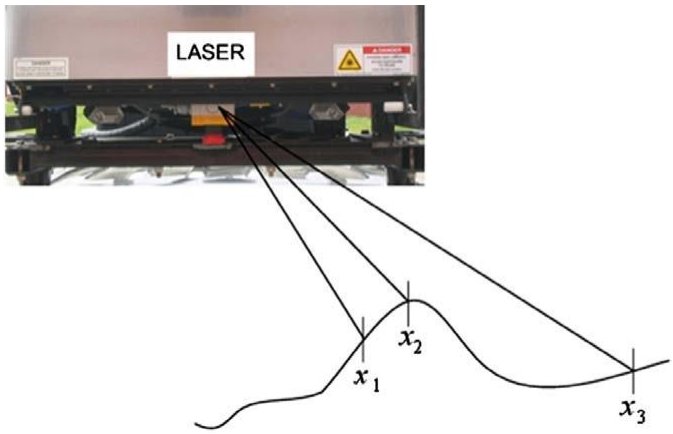

Figure 2.3. Difference in horizontal spacing due to undulations in topology

The resultant terrain surface forms a 'point cloud' of terrain height data at irregular locations in the horizontal plane, shown as blue dots in Figure 2.4. The black axes X and Y define the global coordinate system, typically Easting and Northing respectively. The red axes u and v represent a path-specific coordinate system in which u is the longitudinal path traversed by a vehicle and *v* is perpendicular to the path, *u*. Due to the large size of terrain profile data sets and computational power limitations, these irregularly spaced data are not typically used directly in the simulation process. A gridding process is necessary to generate a compact and effective terrain surface, and terrain profiles, readily accessible for simulation.

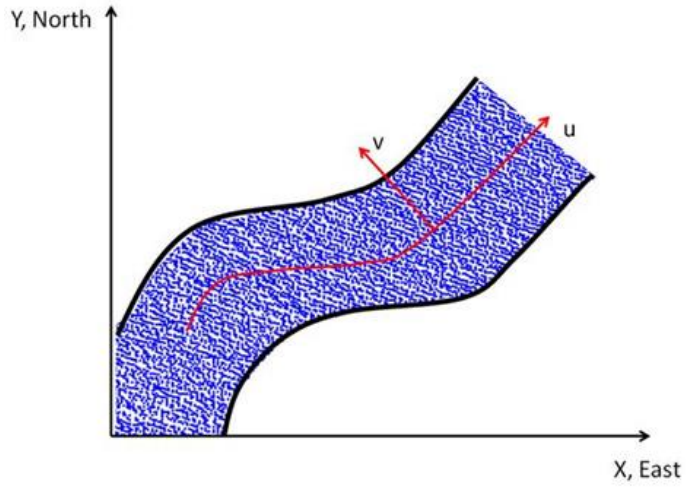

Figure 2.4. Irregularly spaced data obtained by terrain measurement system

Regularly spaced grid nodes are defined in the horizontal plane by introducing regularly spaced increments along path coordinate *u*. Consider the i^{th} grid node defined along coordinate *u*, u_i. There is a corresponding set of regularly spaced grid nodes along *v*, perpendicular to grid node u_i. In this way the horizontal locations of the grid nodes is defined. These discretized points along coordinates *u* and *v* form vectors that are indexed by *i* and *j* respectively. The measured 'point cloud' data set, shown in Figure 2.4 as blue dots, has been transformed to the path-specific curved regular grid coordinate system (u_i, v_j) in the horizontal plane, as shown in Figure 2.5. In this figure the intersection between the horizontal and vertical lines indicate the grid nodes. The uncertainty in these locations is addressed in this work.

The terrain undulations can be represented by interpolated heights at the gridding nodes. The terrain height corresponding to each regularly spaced grid point in the *(u, v)* coordinate system is the nodal height obtained by various gridding methods. It should be clear that the vertical deviations of the terrain surface along paths that are parallel to coordinate *u* are then the 'road profiles', or in general the terrain profiles.

The focus of most road modeling and characterization work is typically on those profiles that lie along the wheel tracks [12, 14].

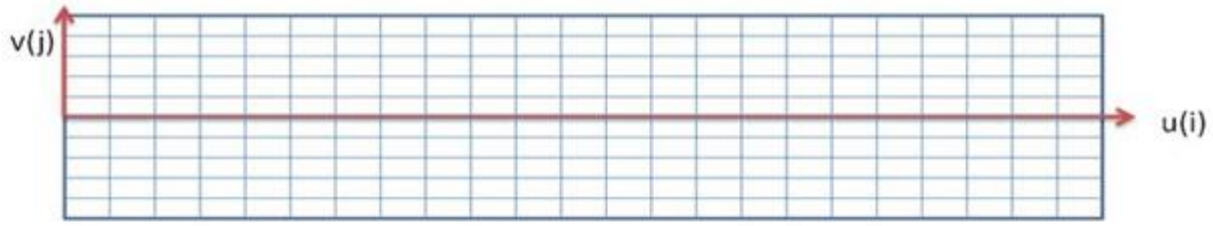

Figure 2.5. Curved regular grid example

2.2.2. Estimating Terrain Heights at Grid Nodes

One current gridding method to create a regularly spaced 3D terrain surface is Digital Terrain Modeling (DTM) [23]. The essential data of a DTM are the finite number of reference points interpolated by various methods with the surrounding terrain data points. Detweiler and Ferris compared four gridding interpolation methods for 3D high fidelity terrain profiles, including mean, median, inverse distance to a power and Kriging [21, 22]. The interpolated height at each grid node is obtained by applying the corresponding algorithm to the data points enclosed inside a search area from which the nodal height is computed, as shown in Figure 2.6. The red circle indicates the search radius within which the data points, shown as crosses, are evaluated. The computational efficiency and interpolation accuracy of each method is compared for different applications. These methods enable the conversion from non- regularly spaced data from the laser scanner to regularly spaced data. They also facilitate the use of high-fidelity 3D terrain measurements in various applications from simple road roughness evaluations to advanced tire modeling.

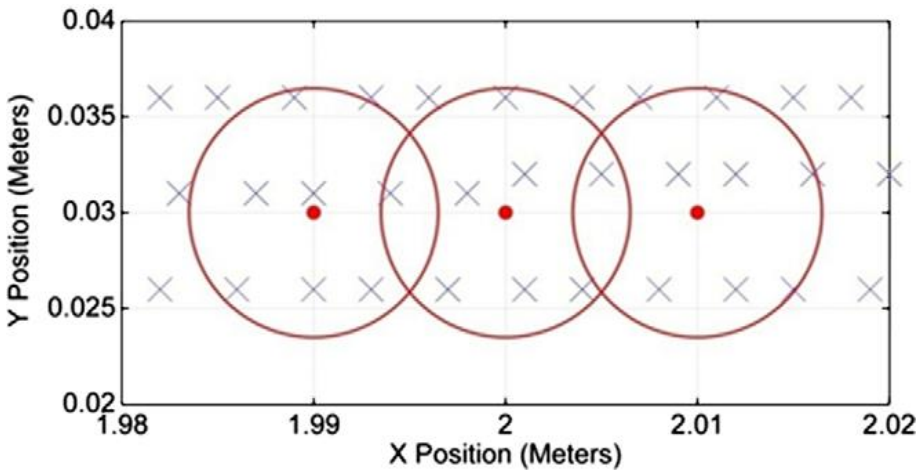

Figure 2.6. Regularly spaced grid example

Currently, the relative horizontal locations between the nodes and the data points are considered to be known exactly. That is, although the uncertainty in the *heights* of the measured data is considered uncertain in each of these interpolation methods, the *horizontal location* of the data are assumed to be known. In this work, a complementary method is developed in which the uncertainty in the horizontal location of the data points is considered and modeled. This leads to a new weighting function for the inverse-distance-to-a-power interpolation method.

2.3 Tire Models

The interaction between the tire and road has long been of interest for vehicle dynamic simulation and chassis design. Therefore, a proper tire model that captures the circumferential deformation and predicts the load is required. The tire model used for vehicle dynamic analysis can be generally categorized into three types as follows.

Analytical Tire Model – The model is developed on pure theoretical analysis of the physical tire structure. The analytical tire model possesses the accurate prediction ability and can be applied to any

situation. However the computational effort required is high due to the complexity and nonlinearity of the physical tire.

Empirical Tire Model – The model is based on the measurement data of the targeted tire behavior instead of analytical deduction. A regression or interpolation method is used to fit the measured data to obtain the model parameters. The model provides accurate results, but the calibration process for the tire parameter is laborious and no physical insight is gained in parameterizing the model.

Semi-empirical Tire Model – The model combines theoretical deduction based on the physical tire properties and experimental data analysis for parameter identification. This model typically requires less computational effort than the analytical tire model. The calibration process is easier than the pure empirical tire model. Therefore it is widely used to develop tire models for vehicle dynamic simulation application.

Finite Element Tire Model – The finite element tire model is capable to take the detailed tire structure into consideration and provide accurate predictions. Due to the complexity and the computational power limitation it is generally not used for vehicle dynamic simulation purpose.

A fundamental requirement of tire models is that they must possess proper bridging and enveloping properties over uneven roads. The resultant force should be obtainable through the circumferential deformation and tire property estimation. A considerable amount of research has been done in this area. Umsrithong presents a detailed review of tire modeling over uneven rigid terrain in his dissertation [24]. Bandel and Monguzzi proposed a semi-empirical model called “Black Box Model” to simulate the tire running over an obstacle [25]. The tire is modeled as a damped one degree of freedom oscillatory system

with five parameters. Compared to the analytical tire model, this semi-empirical model is much computationally efficient and highly duplicable for different tires. However the model neglects the tire bridging and enveloping properties over uneven terrain profiles.

Zeglelaar provides an overview of the tire model categories to simulate the enveloping properties in his dissertation [26]. Among all the categories, the flexible ring model provides a simple and intuitive insight into the interaction between the terrain and tire. The model is widely applied to analyze the tire-terrain interaction. Zegelaar and Pacejka used a flexible ring model to simulate the quasi-static response of a tire rolling over a short wavelength obstacle [27]. The model consists of a deformable circular beam representing the tread band, and springs distributed radially and tangentially representing the sidewall stiffness and tire pressure. The inextensibility for the tire ring model is compared the simulation result with an extensible tread band simulation result. The difference is not significant, but the extensible ring model is much more time consuming. In this way, the inextensible model is preferred for the flexible ring tire model. Loo modeled the tire by using a flexible circular ring under tension with a nest of linear springs and dampers arranged radially [28]. The ring representing the tread band is assumed to be massless and completely flexible for simplicity. The experimental result shows general agreement with the predicted tire response. Thus the flexible ring representing the can be further assumed to be massless.

The tire deflection and force generation mechanism can also be modeled with elastic springs. Badalamenti and Doyle developed a radial-interradial spring tire model to predict vertical and drag forces produced by a tire rolling over a rectangular obstacle [29]. In this model the tire deflection of a local segment is dependent on the adjacent ones. This interdependency of adjacent segments also can be described by modeling the shearing properties with the flexible ring model. Gillespie used a simple radial spring model to simulate the stiffness variation circumferentially [30]. The magnitude of the radial force

variation is found to be relatively independent of speed. The concept can be extended to the limit, with the speed goes to zero. Therefore a quasi-static assumption can be applied for tire modeling. Takayama et al. developed a five degree of freedom mass-spring tire model to predict the transient responses of a tire slowly rolling over a cleat [31]. The belt and tread region was modeled by a rigid ring and deflections from the cleat are absorbed by a linear and planar spring attached to the rigid ring. Modal Analysis is applied to obtain the rigid vibration mode and the torsional vibration mode. Simulation results show that radial rigid mode vibrations dominated the radial axial force. Therefore for in-plane tire model, the force generated by the tire deflection can be obtained through the radial deformation only.

Ferris proposed the static constraint mode tire model to capture the tire enveloping and bridging properties [32]. The tire is modeled with an inextensible ring with some bending stiffness and mass supported by an elastic foundation centered on the rim as shown in Figure 2.7. Circumferential deformation $\{\boldsymbol{u}\}$ is assumed to be adequately represented by a second order, linear model differential equation as given in equation 2. 1.

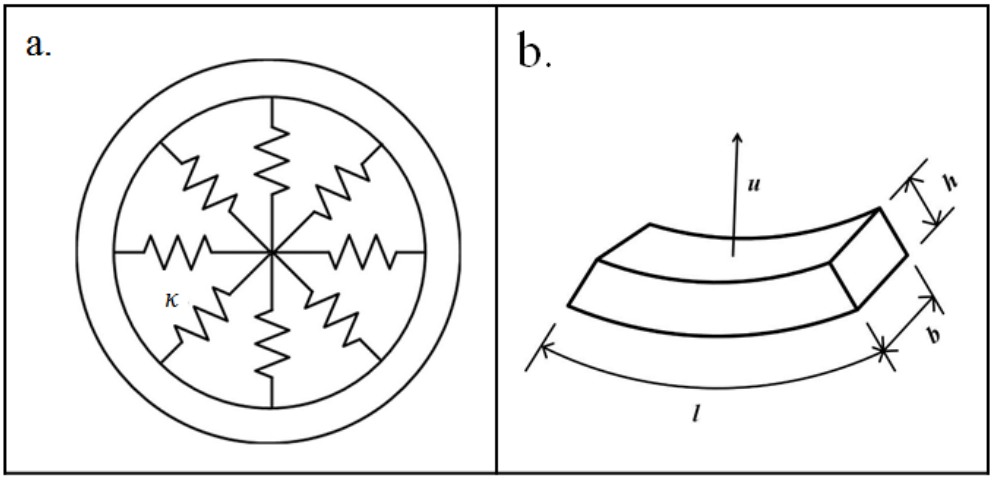

Figure 2.7. Schematic plot of constraint tire model and a piece of tire segment

$$[\boldsymbol{M}]\{\ddot{\boldsymbol{u}}\} + [\boldsymbol{K}]\{\boldsymbol{u}\} = \{\boldsymbol{f}\} \qquad 2.\ 1$$

The stiffness matrix $[\boldsymbol{K}]$ is a circulant Toeplitz matrix due to the symmetry of the problem. The physical degrees of freedom are reordered and divided into active and omitted, and the mass and stiffness matrices are portioned as equation 2. 2.

$$\{\boldsymbol{u}\} = \begin{Bmatrix}\{\boldsymbol{u^a}\}\\ \{\boldsymbol{u^o}\}\end{Bmatrix}$$

$$[\boldsymbol{M}] = \begin{bmatrix}[\boldsymbol{M^{aa}}] & [\boldsymbol{M^{ao}}]\\ [\boldsymbol{M^{oa}}] & [\boldsymbol{M^{oo}}]\end{bmatrix} \qquad 2.\ 2$$

$$[\boldsymbol{K}] = \begin{bmatrix}[\boldsymbol{K^{aa}}] & [\boldsymbol{K^{ao}}]\\ [\boldsymbol{K^{oa}}] & [\boldsymbol{K^{oo}}]\end{bmatrix}$$

Since quasi-static deflections are assumed, the second derivative of the radial deflection vector vanishes. Through Gyuan deduction [33], the tire radial deflection can be calculated as equation 2. 3 through the active constraints. The resultant spindle force can then be predicted with the stiffness matrix and the circumferential deformations.

$$\{\boldsymbol{u}\} = \begin{Bmatrix}\{\boldsymbol{u^a}\}\\ \{\boldsymbol{u^o}\}\end{Bmatrix} = \begin{bmatrix}[\boldsymbol{I}]\\ -[\boldsymbol{K^{oo}}]^{-1}[\boldsymbol{K^{oa}}]\end{bmatrix}\{\boldsymbol{u^a}\} \qquad 2.\ 3$$

The method uses an iterative process to identify the active constraints at the tire-road interface as shown by Figure 2.8 [32]. First the point along the road profile that has the greatest interference with the undeformed tire shape is determined and considered to be the first active constraint. The addition of this active constraint yields a corresponding deformed tire shape as shown by (b). Given the deformed tire shape, the consecutive points with the greatest interference are identified as the next active constraints and are used to obtain new deformed shape. This process is shown graphically in Figure 2.8 (c) through (f). The iterative process continues until there is no active constraint, i.e. no point along the road profile interfere with the current prediction of the deformed tire shape.

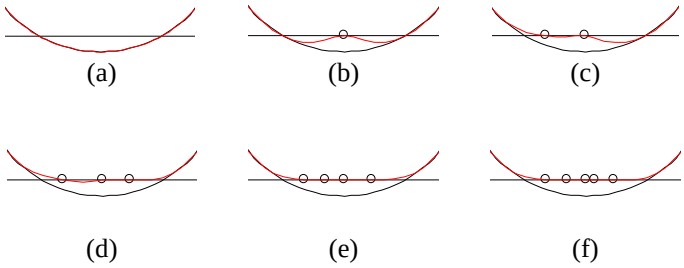

Figure 2.8. Iterative process to identify active constraints

2.4 Effective Road Profile

Even if the terrain profile input is regularly spaced, it is still not computationally efficient to directly perform vehicle dynamic simulation on them due to the complexity of the tire structure. An alternative efficient approach is to use a simplified tire model excited by an effective terrain profile instead of the original terrain. The objective is to produce responses that are nearly identical to the ones a complex tire model and unfiltered terrain would produce. A considerable amount of research has been done for effective road profile generation. The approach can be categorized into two types as follows.

2.4.1 Morphological Filter

As traveling on the uneven terrain, the tire samples the terrain surface on the top. Over a finite length, with tire geometry assumed fixed, a morphological filter can be developed for equivalent terrain profile generation. Due to the round shape of the tire, an acceptable shape to develop the filter is a circle. In Guo's paper, a rigid roller contact filter is proposed as shown in Figure 2.9 [34]. The rigid roller is assumed to always keep in contact with the terrain profile. The obtained vertical trajectory of the roller center is considered to be the effective road profile.

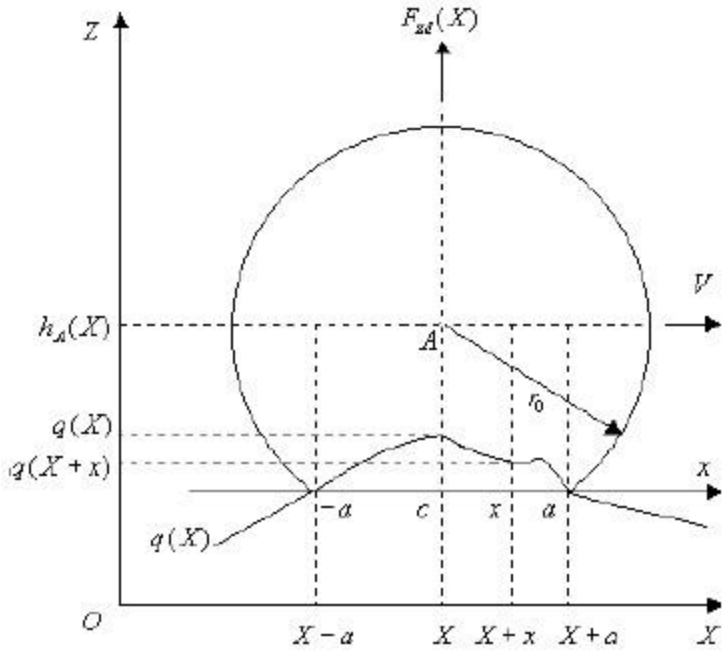

Figure 2.9. Rigid roller method to determine the effective road profile

Another mathematical morphological filter for effective terrain profile generation is image analysis technique based on set theory [35]. The opening operation effect on image processing can be shown as Figure 2.10 with the structure elements S to probe the image X. It can be seen that the sharp edge is removed after opening using a circular structure element. For more complicated images, the opening operation can be used to remove the ambiguities and local transients.

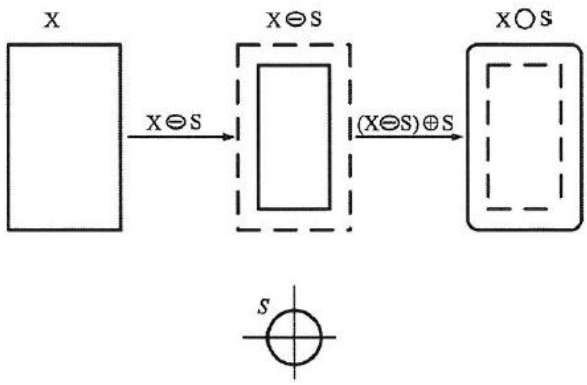

Figure 2.10. Opening Operation to Remove the Ambiguities

The mathematical morphological filter can be used as a morphological filter to generate the equivalent terrain from actual terrain [36]. First the terrain profile plot is transformed into binary image X shown as Figure 2.11. An elliptical structure element S, usually a circle to represent the wheel, is used for the opening operation with the road binary image. Finally the obtained binary road image after the opening operation is reversely transformed into elevation signals.

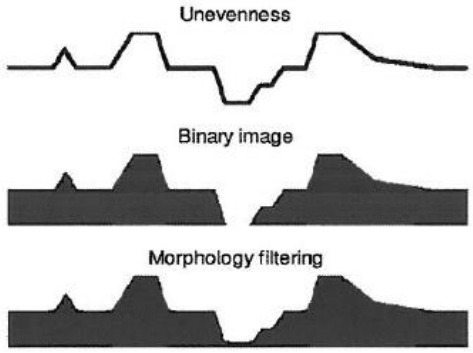

Figure 2.11. Morphologic filter applied on binary image of terrain profile

The application of morphological filtering to generate effective terrain profile is simple and intuitive. However deformability of the pneumatic tire running over a terrain profile is ignored. Therefore the tire bridging and enveloping properties are not reflected accurately by the filtered terrain profile. Given a rough original terrain, the difference between the obtained effective profile and the actual tire center trajectory would be considerable. Besides, both morphological filter reviewed doesn't involve any spindle load information; therefore the obtained effective terrain profile would be independent of the spindle load. However in reality the tire bridging and enveloping properties are determined by circumferential deformation over the terrain irregularity, and are strongly influenced by the spindle load. Thus the morphological filter method is not suitable to generate effective terrain profile as input to a simplified tire model in vehicle dynamic simulation.

2.4.2 Basic Function

The effective terrain profile generation is developed to provide an input to the simplified tire model in vehicle dynamic simulation. The objective is to greatly improve the computational efficiency with minimal accuracy loss of the obtained spindle force. To include the spindle force in the terrain pre-filtering process, the concept of a basic function is introduced [25, 26]. The basic function is considered as effective excitations of the tire caused by the obstacles under a certain spindle load. With a fixed shape obstacle, Bandel et al. discovered the tire response can be decomposed into two equal but shifted half sine waves as shown by Figure 2.12 [25]. The parameters of the basic functions are obtained by experimental data or simulation result with a tire model.

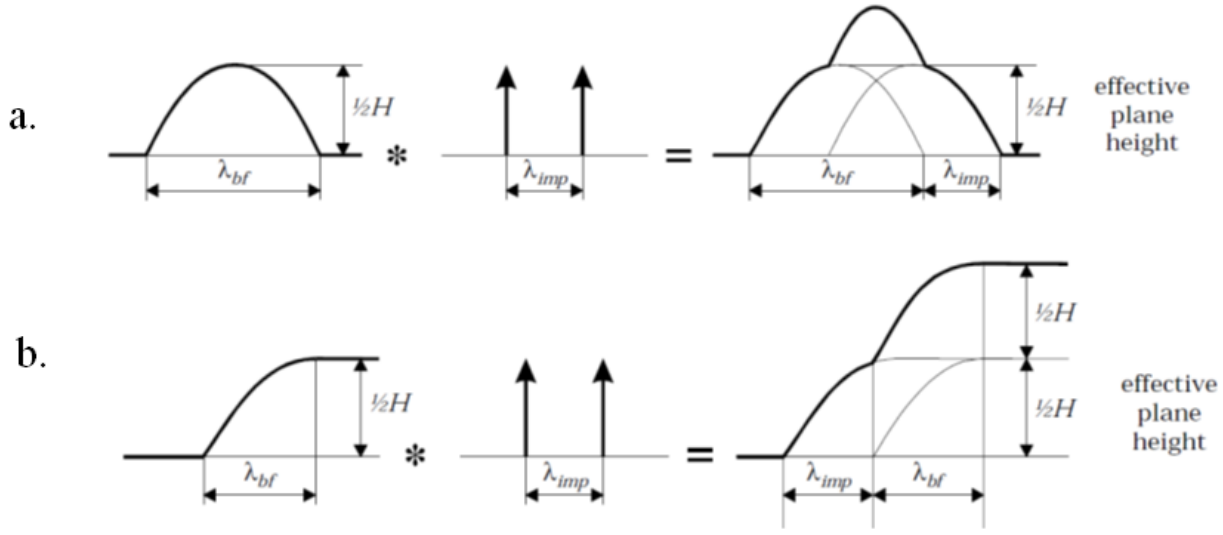

Figure 2.12. The composition of the effective road surface from basic functions for obstacles: a) Trapezoid cleat. b) Positive Step

The basic function is widely for effective terrain profile generation. Pacejka introduced the two-point follower technique to compute the effective terrain profile based on basic function curves, as shown in Figure 2.13 [37]. The basic curve is defined to be assessed at constant vertical load when rolling over a trapezoid obstacle with a very low speed. The horizontal projection of the segment defined by the two points is kept to be a constant. The midpoint height of the two points moving along the basic curve is considered to be the description of the equivalent road height.

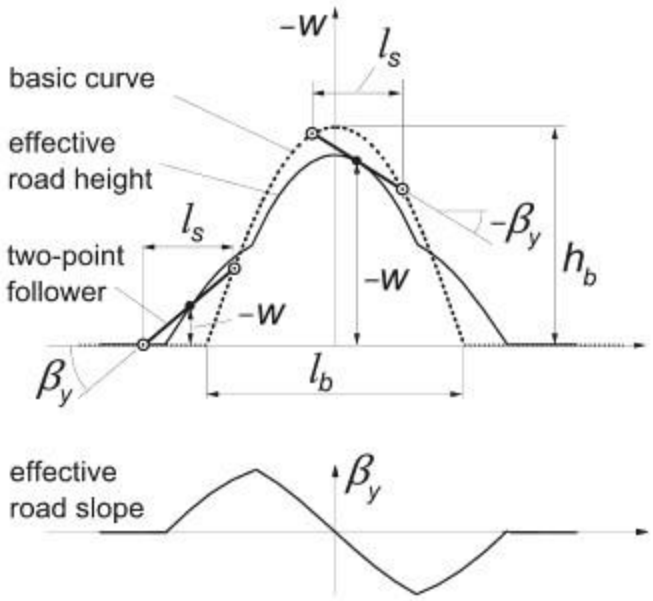

Figure 2.13. Two point follower method to determine the effective road profile

Schmeitz applied two elliptical cams following each other at a fixed distance to obtain the effective road height as shown in Figure 2.14 [38]. The change in height of the connecting line midpoint and its inclination represent the effective height and effective slope respectively.

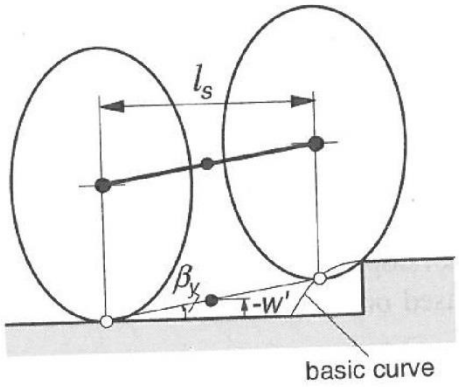

Figure 2.14. Two cam follower method to determine the effective road profile

It can be seen from Figure 2.13 that the first derivative of the generated effective terrain profile is discontinuous for a step obstacle, i.e. the obtained filtered curve is not smooth. Besides the previous reviewed method are developed based on the basic functions, which are highly dependent on the obstacle shape, the vertical load and the spindle height. Therefore the calibration process to obtain the corresponding basic function parameters needs to be performed if the obstacle or the operation condition changes. It is difficult to directly apply on various kinds of terrain profiles with different operation conditions.

2.5 Vehicle Dynamic Simulation Model

An accurate and computationally efficient vehicle dynamic simulation model is essential for chassis load prediction. Chul and Ro have shown that a simple seven-degree-of-freedom (7-DOF) vehicle model is able to accurately portray vehicle ride dynamics [39]. The vertical motions of the four suspensions are considered to be lumped unsprung masses; Similarly, the bounce, pitch, and roll of the vehicle body is considered a lumped sprung mass. The 7-DOF model for vehicle ride dynamics is shown in Figure 2. 15. The model is excited by the terrain profile input and only applies to low speed application in this paper. Therefore the aerodynamic loads can be neglected.

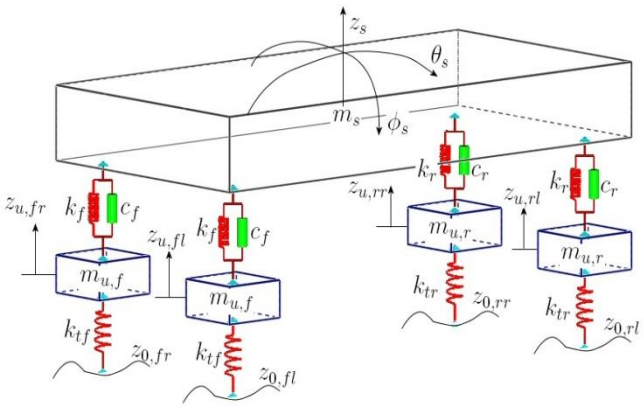

Figure 2. 15. 7-DOF Vehicle Model

Muller developed a system identification process to accurately estimate 7-DOF vehicle system parameters [40]. The vehicle is excited by a speed bump and an optimization method is applied to estimate the model parameters through the vehicle response comparison. A simple point follower tire model is used in the calibration process and can be substituted later by more complicated ones to address the tire bridging and enveloping properties and provide more accurate spindle load estimation. As the complexity of the tire model increases, the computational efficiency decreases and the simulation process becomes more time consuming.

3. Stochastic Gridding Method and Probabilistic Terrain

Non-deformable terrain imposes a unilateral geometric boundary constraint on rolling tires to which the chassis responds by generating loads, moments, motions, deformations, etc. The terrain profile undulation is a consistent excitation to the chassis, through the tire, throughout the iterative design process. High fidelity terrain measurement of non-deformable terrain can be provided with a new 3D scanning laser systems that performs both on-road and off-road measurements [12, 14]. However, the resultant terrain topology is represented by an irregularly spaced cloud of terrain points. Due to the large size of terrain data sets and computational power limitations, a gridding process that produces a uniformly spaced data configuration is essential for simulation efficiency [21, 22]. The gridded terrain is represented by a series of uniformly spaced nodes assigned according to the original cloud of points and the selected path. The height of the gridding node is estimated by the surrounding terrain points.

Due to the inaccuracies inherited from the measuring equipment, the measured cloud of points can be considered as a realization of the true terrain point location. As the gridding nodes are assigned according to the cloud of points, with the true cloud of points location unknown, the true gridding node location is considered unknown. Given the measured terrain points, the estimated gridding node location can be computed with a selected path and considered to be deterministic. Therefore the relative location between measured terrain points and the true gridding node is considered stochastic. To differentiate the contribution of terrain points towards nodal height estimation, each terrain point is assigned with a weighting function according to the relative distance to the gridding node. If the uncertainty vanishes, the location of the terrain points relative to the true gridding node is considered to be true, as was assumed in Chapter 2.

Since the relative distance is embedded with underlying uncertainties from the measurement equipment, the resultant nodal height should be stochastic as well. The obtained uniformly spaced terrain data configuration composes of sequential nodal heights represented as random variables and it is defined as a probabilistic terrain. The uncertainty of the random variable can be described by empirical Cumulative Distribution Function (C.D.F) [41]. Compared to the deterministic terrain profile obtained through the gridding method reviewed in Chapter 2, the nodal height of a probabilistic terrain is stochastic. In order to generate realizations, the marginal probability of the nodal height and the dependent relationship between the heights of two gridding nodes are required.

The nodal height random variable is defined to only take realizations on values of the measured heights of terrain points. Therefore the obtained empirical Cumulative Distribution Function (C.D.F) is discrete and it is considered as marginal probability of the nodal height. To define a dependent relationship between the heights of two gridding nodes, a conditional probability based on the weighting function is introduced. A number of realizations of the underlying stochastic terrain can be generated given the original cloud of terrain points and the selected path. The variation of the terrain profile realizations reflect the stochastic nature of the gridded terrain profile, which is inherited from the uncertainty of the measuring equipment.

The scope of this chapter is to obtain a uniformly spaced probabilistic terrain from the original measured cloud of points by a stochastic gridding method. The work is organized as follows. First, a stochastic weighting function assignment method is introduced to include the inherited horizontal measurement uncertainty. Then the obtained stochastic representation of the weighting function is modeled to evaluate the weighting function in terms of the estimated relative distance between the gridding node and the terrain point. Next, with the model of the weighting function, a stochastic gridding method is developed. The obtained uniformly spaced terrain profile is a probabilistic terrain, composing of nodes with heights

as random variables. Finally the realizations of the probabilistic terrain profile can be generated. The influences of weighting function parameters are discussed.

3.1. Stochastic Gridding Method

3.1.1 Weighting Function

The measured cloud of terrain points can be converted to uniformly spaced terrain data configuration using the gridding methods reviewed in Chapter 2, under the assumption that the horizontal locations of terrain points are deterministic. The relative locations of the points with respect to the gridding nodes are considered to be fixed. Among all the existing gridding methods, the inverse distance to power introduces the concept of differentiating the contribution made by terrain points according to their relative distance to the gridding node, *d*, In this work, when the distance between the node and the terrain point is considered to be known exactly, inverse-distance-to-a-power (IDP) are used to assign weight *w*, as expressed by equation 3. 1.

$$w(d) = d^{-n} \qquad 3.1$$

The weighting, *w*, assgined to terrain points that are closer to the horizontal location of a grid node can be orders of magnitude larger than other points that are also nearby. An example of $n = 0.02$ is shown in Figure 3.1. As the distance from the point to the node increases, the relative contribution it makes to the nodal height evaluation decreases and correspondingly the weighting factor decreases too. If there is a terrain point location that coincides with the gridding node, the corresponding measured height is considered to be infinitely important in the nodal height estimation process; therefore the weight of this terrain point is considered to be infinite too. As a result, the nodal height is exactly the height of that terrain point. As *d* increases from 0 to 0.1, the weighting factor drops from infinite large to less than 1.05. The rate of this decent is determined by the exponent, *n*, which can be adjusted depending on the

application. As *n* approaches infinity, only the points that are the nearest to the node are taken into consideration. The gridding method is identical to nearest neighbor estimation.

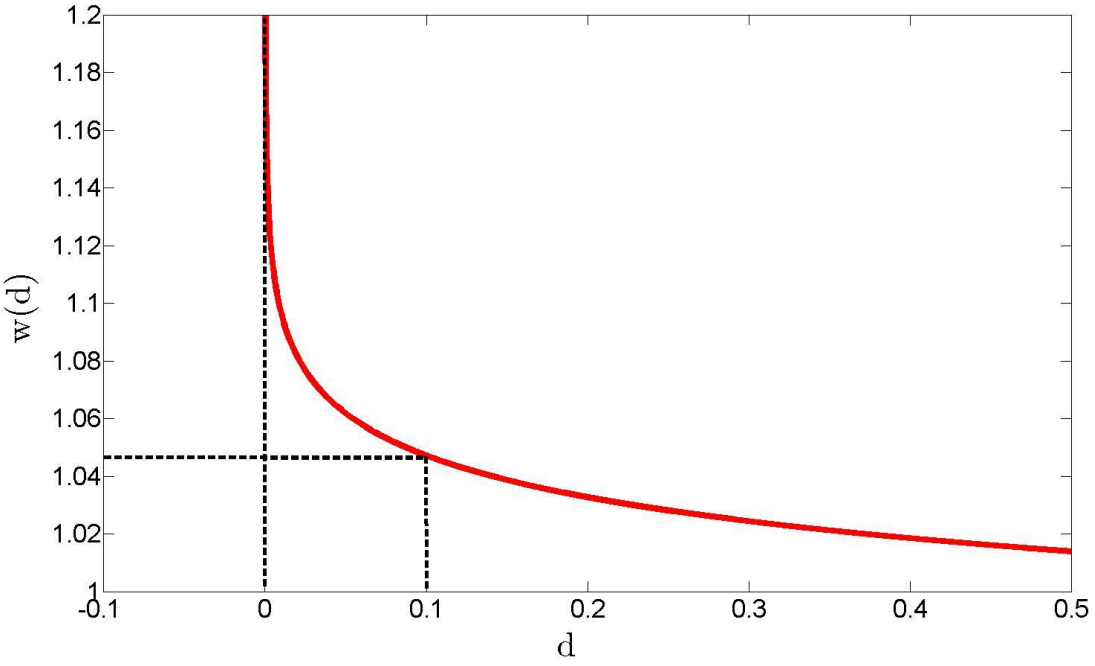

Figure 3.1. Weighing function *w(d)* with respect to the known distance *d*

3.1.2 Stochastic Weighting Function Derivation

With the uncertainties inherited from the terrain measurement equipment and methodology, the relative distance between the measured terrain point and the true gridding node is represented by a random variable *D*. The weighting function shown as 3. 1needs to be evaluated in terms of the random variable *D*.

The geometry of the terrain point with respect to the estimated and true gridding nodes is shown in Figure 3.2. O is the true location of a grid node under consideration, and O_e is the estimated (measured) position. P is the location of a terrain data point. The location of O_e is estimated based on the measured cloud of points and set to be the reference origin in the coordinate system. The relative distance between the true gridding node and the estimated one is represented by a random variable *R*. The relative locations of *O* and *P* are not measureable because the location of *O* is not known. The uncertainty is described in the polar coordinates system by the random variables *R* and Θ, while $\hat{d}$ and φ are measured parameters.

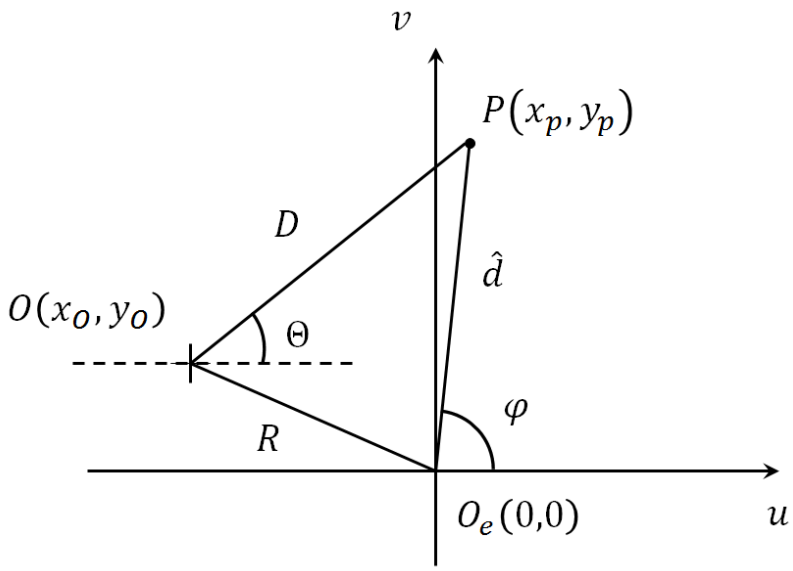

Figure 3.2. Geometric layout of relative positions between terrain points and gridding nodes

According to the definition, the Cumulative Probability Density Function (C.D.F) of W can be evaluated based on the C.D.F of D as equation 3. 2.

$$F_W(x) = P(w(D) < x) = P(D^{-n} < x) = P\left(D > x^{-\frac{1}{n}}\right) = 1 - F_D\left(x^{-\frac{1}{n}}\right) \qquad 3.\ 2$$

Due to the physical meaning of distance, *x* must always be positive. The C.D.F of *D* can be transformed into the C.D.F of D^2 as equation 3. 3

$$F_D(x) = P(D < x) = P(D^2 < x^2) = F_{D^2}(x^2) \quad 3.\ 3$$

Therefore if the C.D.F of D^2 is known, the distribution of the weighting factor *w* can be expressed as equation 3. 4.

$$F_W(x) = 1 - F_{D^2}\left(x^{-\frac{2}{n}}\right) \quad 3.\ 4$$

From the geometry shown in Figure 3.2, D^2 can be decomposed as equation 3. 5.

$$D^2 = \hat{d}^2 + R^2 - 2\hat{d}Rcos(\Theta - \varphi) \quad 3.\ 5$$

Therefore, the C.D.F of D^2 can be computed as equation 3. 6.

$$F_{D^2}(x) = F_{\hat{d}^2+R^2-2\hat{d}Rcos(\Theta-\varphi)}(x) = P\left(\hat{d}^2 + R^2 - 2\hat{d}Rcos(\Theta - \varphi) < x\right) \quad 3.\ 6$$

The procedure of stochastic weighting computation is shown in a flow chart as Figure 3.3. The red represents stochastic random variables and the blue represents variables with deterministic values. As shown in the flow chart, the uncertainty of the true gridding node is described by two random variables: Θ and *R*, which can be used to compute the relative distance as shown by equation 3. 5. Through the relative distance, the C.D.F. of the weighting function $w(D)$ can be computed as shown by equation 3. 2. The terrain measurement uncertainty is then included in the nodal height evaluation process.

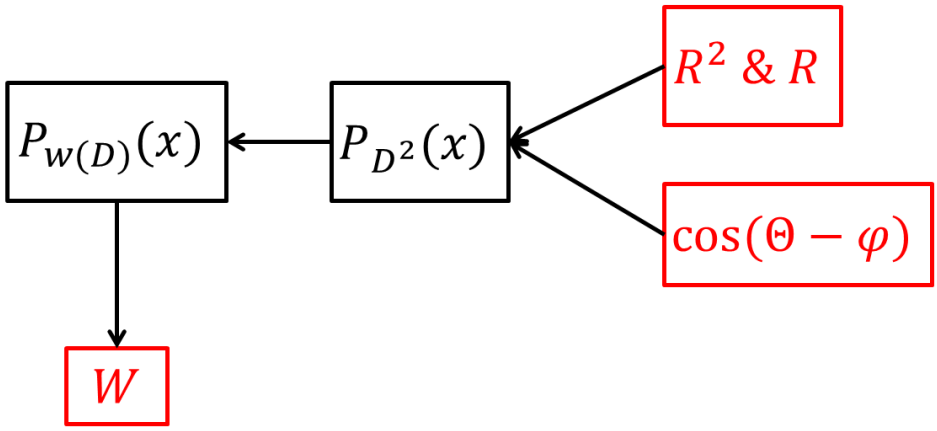

Figure 3.3. Flow chart of stochastic gridding method to compute the nodal height

3.1.2.1 Development of C.D.F. for R and R^2

The distance between the true gridding node and estimated node location is represented by random variable R. R can be decomposed into Cartesian components as shown in equation 3. 7.

$$U = R\cos(\varphi) \qquad 3.\ 7$$

$$V = R\ \sin(\varphi)$$

It is assumed that the GPS error in the horizontal locations arises from multiple independent sources and no single source is dominant over the others [42]. Therefore according to Central Limit Theorem, the horizontal errors U and V can be modeled as normal distributions centered around the origin with the same standard deviation σ [43], shown in equation 3. 8.

$$U, V \sim \mathcal{N}(0, \sigma^2) \qquad 3.\ 8$$

The distribution of R^2 is then a chi-squared distribution and the Probability Density Function (P.D.F) of R^2 can be computed with equation 3. 9.

$$f_{R^2}(x) = e^{-\frac{x}{2\sigma^2}} \frac{1}{2\sigma^2} \quad 3.9$$

Now, let X and Y be continuous random variables and $Y = g(X)$. Suppose g is one-to-one or monotonic, and both g and its inverse function g^{-1}, are continuously differentiable. Then according to the random variable transformation theorem [43], the transformation from the P.D.F of X to Y is given by equation 3. 10.

$$f_Y(y) = f_X[g^{-1}(y)] \left| \frac{dg^{-1}(y)}{dy} \right| \quad 3.10$$

By transforming the random variable from R^2 to R, the P.D.F of R can be obtained as shown in equation 3. 11.

$$f_R(r) = f_Z[g^{-1}(r)] \left| \frac{dg^{-1}(r)}{dr} \right| = \frac{e^{-\frac{r^2}{2\sigma^2}}}{2} \cdot \frac{2r}{\sigma^2} = \frac{re^{-\frac{r^2}{2\sigma^2}}}{\sigma^2} \quad 3.11$$

3.1.2.2 Development of C.D.F. for $cos(\Theta - \varphi)$

The measurement error is considered to be locally isotropic. Therefore the orientation angle Θ can be assumed regularly distributed around the gridding node and the P.D.F of Θ can be written as equation 3. 12.

$$f_\Theta(x) = \begin{cases} \frac{1}{2\pi} & x \in [0, 2\pi] \\ 0 & otherwise \end{cases} \quad 3.12$$

The orientation angle φ can be calculated from the relative position of O_e and P and it is deterministic. As θ varies from 0 to 2π, $cos(\theta - \varphi)$ and $cos\theta$ experience one identical cycle, with only a phase

difference. Therefore the P.D.F of $cos(\Theta - \varphi)$ is the same as p.d.f. of $cos\Theta$ and it is independent of φ. The geometric interpretation is that the system coordinates are centered at location O_e, local isotropicity is assumed for the relative location of point *O*. Therefore the random variable Θ denoting the angular position of the true gridding node can be assumed a uniform distribution. The angle Θ can be expressed as equation 3. 13 based on the geometry shown in Figure 3.2. The angle φ is an overall deterministic orientation angle of the whole geometry set. Specifically, as the coordinate system rotates about O_e, the distribution of distance *D* will not be affected.

$$\Theta = \arctan\left(\frac{y_P - V}{x_P - U}\right) = \arctan\left(\frac{\hat{d}sin\varphi - V}{\hat{d}cos\varphi - U}\right) \qquad 3.\ 13$$

The C.D.F of $\cos(\Theta - \varphi)$, or equivalently $cos\Theta$, is calculated by defining a new random variable $Y = \cos(\Theta - \varphi)$ using the random variable transformation theorem as 3. 14.

$$f_Y(x) = \begin{cases} \dfrac{1}{\pi\sqrt{1 - x^2}} & x \in [-1,1] \\ 0 & otherwise \end{cases} \qquad 3.\ 14$$

Since the location of the data point located at *P* is independent from the true grid node at *O*, then the distance *R* and the angle Θ (and therefore *Y*) must be independent, so that the C.D.F. for D^2 is given by equation 3. 15.

$$F_{D^2}(x) = P\left(\hat{d}^2 + R^2 - 2\hat{d}RY < x\right) = \iint\limits_{\hat{d}^2 + R^2 - 2\hat{d}RY < x} f_R(r) f_Y(y) dr dy \qquad 3.\ 15$$

Therefore the C.D.F of the weighting function *w(D)* can be obtained from equation 3. 4 and equation 3. 15.

$$F_W(x) = 1 - \iint_{\hat{d}^2+R^2-2\hat{d}RY<x^{-\frac{2}{n}}} f_R(r) f_Y(y) dr dy \qquad 3.\ 16$$

3.1.3 Numerical Validation

To examine the validity of the derivation, simulated data are generated according to the assumptions that the error is normally distributed in both of the horizontal directions and that the data are locally isotropic. The numerically integrated C.D.F of D^2 is calculated from equation 3. 15, which is compared with Monte Carlo simulation results in Figure 3.4 for the specific case when $\hat{d}$ and σ both equal 0.1. The small difference oscillation in the curves is due to the finite number of iteration used in the Monte Carlo simulation. It can be seen that the simulation result agrees with the computed analytical result. This exercise was performed to validate the analytical derivations in equation 3. 1 through equation 3. 15.

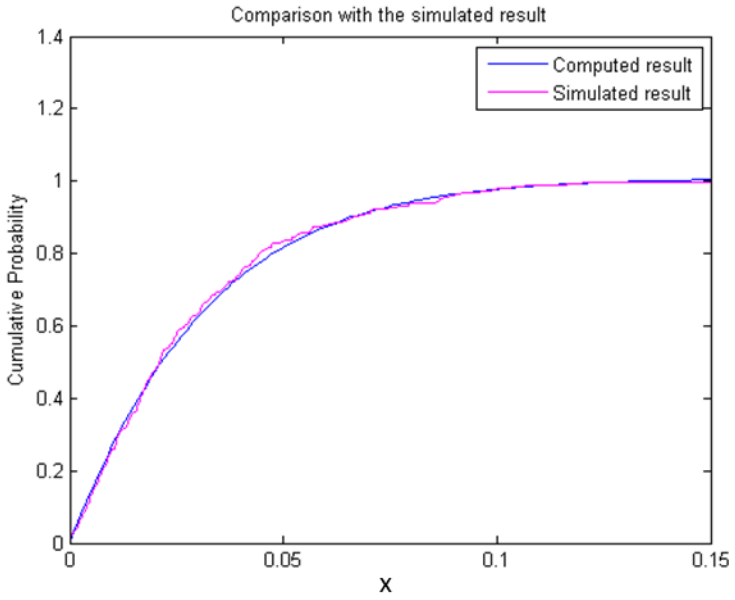

Figure 3.4. Comparison of $F_{D^2}(x)$ obtained analyticaly and numerically

3.1.4 Weighting Function Modeling

Although equation 3. 15 and equation 3. 16 cannot be solved in closed form, two limiting conditions are considered in approximating the median distance from the true grid node to the data point, $\widetilde{D}$. First, it is clear from the geometry defined in Figure 3.2 that when the horizontal location of the grid point is known exactly ($\sigma = 0$), then the median distance $\widetilde{D}$ is equal to the actual distance *D* which is in turn equal to the estimated (measured) distance $\hat{d}$. This limiting case is written as equation 3. 17.

$$\widetilde{D}\big|_{\sigma=0} = \hat{d} \qquad 3.\ 17$$

Second, if the distance from the data point to the estimated grid point is zero ($\hat{d} = 0$), then the true distance *D* varies with the error in the horizontal location of the grid. Specifically, the distribution of *D* is equal to the distribution of *R*, so that $f_D(x) = f_R(x)$. The median distance, $\widetilde{D}$, would then be determined by integrating equation 3. 11 and solving for $\widetilde{D}$ as shown in equation 3. 18.

$$\int_0^{\widetilde{D}} f_R(r)dr = \int_0^{\widetilde{D}} \frac{re^{-\frac{r^2}{2\sigma^2}}}{\sigma^2} dr = 1/2 \qquad 3.\ 18$$

So, for the limiting condition when the estimated distance from the data point to the grid point is zero ($\hat{d} = 0$), the median distance from the true grid point to the data point being evaluated $\widetilde{D}$ is given by equation 3. 19, where the parameter $\alpha = \sqrt{2\ ln(2)}$is now defined and σ is the standard error in the horizontal position of the grid nodes.

$$\widetilde{D}\big|_{\hat{d}=0} = \sqrt{2\ ln(2)}\ \sigma = \ \alpha\sigma \approx 1.1774\,\sigma \qquad 3.\ 19$$

From equation 3. 3 and equation 3. 15, the C.D.F of the random variable can be obtained as

$$F_D(x) = F_{D^2}(\sqrt{x}) = \iint_{\hat{d}^2+R^2-2\hat{d}RY<\sqrt{x}} f_R(r) f_Y(y) dr dy \qquad 3.\ 20$$

With equation 3. 20 computed numerically, the median distance to the true grid node is evaluated with respect to changes in $\hat{d}$ and σ as shown in Figure 3.5. Consider the two limiting conditions in approximating the median distance from the true grid node to the data point, $\widetilde{D}$. It is clear that when σ = 0, the median distance from the true grid point to the data point, $\widetilde{D}$, varies linearly with $\hat{d}$, as described in equation 3. 17. Similarly, when $\hat{d} = 0$, $\widetilde{D}$ varies linearly with σ, where the linear relationship has a slope of α, as defined by equation 3. 19.

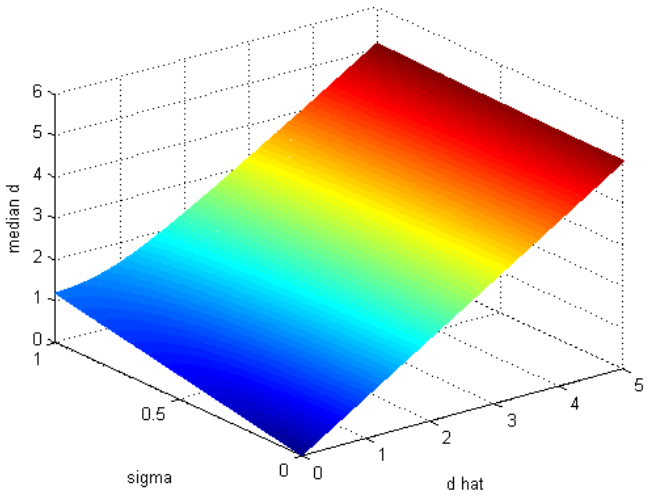

Figure 3.5. Median distance $\widetilde{D}$ vs. horizontal error σ and the estimated distance $\hat{d}$

More general results are demonstrated in the contour plot of $\tilde{D}$ shown as Figure 3.6. The nearly circular contour lines and the nearly even spacing between different contour lines suggest that some geometric average of the standard deviation, σ, and the estimated distance, $\hat{d}$, is appropriate to estimate the median distance $\tilde{D}$. That is, if the contour edges were circular and evenly spaced, then the square of the median distance would be the sum of the squared estimated distance and the squared standard deviation. A more general form of such an approximation is required since the contour lines are not circular.

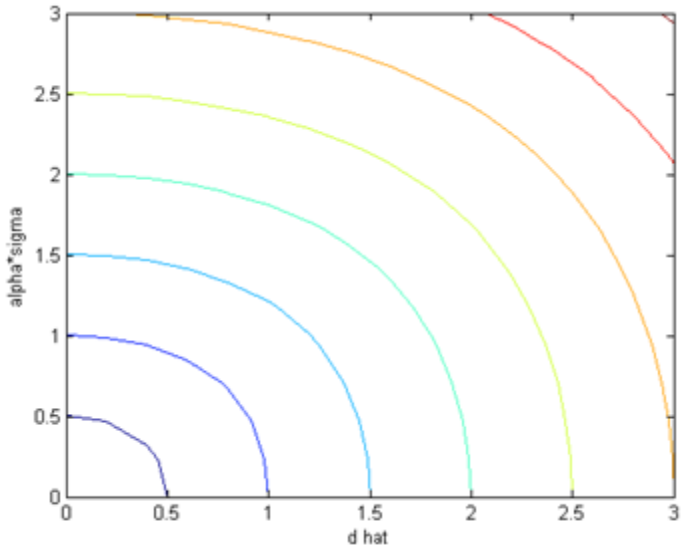

Figure 3.6. Contuour plot of $\tilde{d}$ VS $\alpha\sigma$ and $\hat{d}$

These numerical simulation results suggest an assumed form for the approximation of $\tilde{D}$, as proposed in equation 3. 21. Note that this form satisfies both of the special cases ($\sigma = 0$ and $\hat{d} = 0$) when $\alpha = \sqrt{2\ln(2)}$. The parameter β is tuned to minimize the error in the estimate.

$$\tilde{D} \approx \left[(\alpha\sigma)^{\beta} + \left(\hat{d}\right)^{\beta}\right]^{\frac{1}{\beta}} \qquad 3.\ 21$$

Note that this equation can be normalized with respect to the standard deviation in the horizontal error, σ. The normalized equation is given as equation 3. 22.

$$\frac{\widetilde{D}}{\sigma} \approx \left[\alpha^{\beta} + \left(\frac{\hat{d}}{\sigma}\right)^{\beta}\right]^{\frac{1}{\beta}} \qquad 3.\ 22$$

Equation 3. 22 provides the estimation of the median standardized true distance between the grid node and the terrain points, based on the standardized measured distance. The relationship between $\frac{\widetilde{D}}{\sigma}$ and $\frac{\hat{d}}{\sigma}$ is plotted in Figure 3.7, where the individual dots represent the median distance from the true grid node to the terrain point, normalized by the standard deviation, while the solid line is the estimated median distance from the true grid point to the data point, normalized by the standard deviation. The dotted line is a reference to show that as $\hat{d}$ grows much larger than σ, it asymptotically approaches the median distance, $\widetilde{D}$ (corresponding to the first limiting condition, $\sigma = 0$). The y-axis intercept occurs at $\widetilde{D} = \alpha\sigma$ (corresponding to the second limiting condition, $\hat{d} = 0$). The parameter β is tuned to minimize the maximum percent error in the estimate of $\widetilde{D}$. It is clear from visual inspection that the individual dots and the curved line are nearly indistinguishable; the error in this estimate is less than 1% over the domain $\sigma \in$ (0,2] and $\widetilde{D} \in [0, 6]$ when β = 2.3.

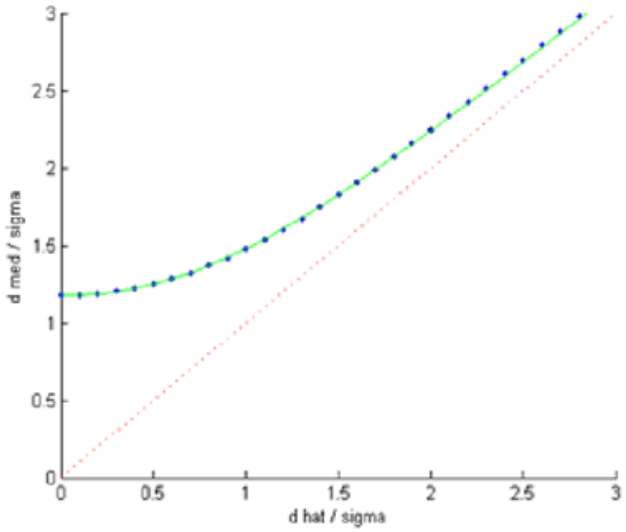

Figure 3.7. Normalized median distance $\frac{\tilde{D}}{\sigma}$ VS. Normalized estimated distance $\frac{\hat{d}}{\sigma}$

3.1.5 Weighting Function Definition used for Stochastic Gridding Method

Based on equation 3. 21, a weighting function can be developed to quantitatively differentiate the contribution of each terrain point in nodal height evaluation process as equation 3. 23. With the true relative horizontal distance between a measured terrain point and a grid node, *D* unknown, an estimated relative horizontal distance, $\hat{d}$, is used as a surrogate for weighting function evaluation. The value of parameters α and β can be obtained from previous numerical analysis section. The measurement error in the approximation is normally distributed in both the Easting (global x) and Northing (global y) directions and the mean is assumed to be zero and the standard deviation is σ. The exponent n can be adjusted to determine the decaying rate of the weighting function depending on the specific application. The choice of *n* is outside the scope of this work wherein the value *n=2.3* will be used for simplification. The appropriateness of this choice of exponent will be discussed later in this chapter.

$$w(\hat{d};n) \equiv \left[(\alpha\sigma)^{\beta} + (\hat{d})^{\beta}\right]^{-\frac{n}{\beta}} \qquad 3.\ 23$$

$$\alpha = 1.1774 \quad \beta = 2.3 \quad \sigma = 25mm$$

The curve of weighting function with respect to the estimated distance $\hat{d}$ can be shown as the blue line in Figure 3.8, with exponent n = 2.3 and σ =25 mm. Note that when the estimated distance $\hat{d}$ is small, the weighting function is nearly flat, so that points lying within this error of the horizontal position are considered nearly equally. As the estimated distance approaches one standard deviation (25mm), the weight assigned to that point begins to decrease rapidly. If the measurement uncertainty vanishes, that is, $\sigma = 0$, the terrain point location is considered known exactly. The weighting function is denoted as w_0 and can be evaluated as equation 3. 24. It can be considered the same as equation 3. 1 (inverse-distance-to-a power), with the true distance between the terrain point and the gridding node can be estimated exactly. The corresponding curve can be shown as the red line in Figure 3.8. If the distance is null, the weighting function approaches infinity, so the corresponding terrain point is considered infinitely more important than all the others. The evaluated height of the gridding node would take the exact same value of the terrain point height. As the distance gets larger, the weighting functions begin to decrease. If the estimated distance keeps increasing, the weighting functions estimated by the two functions $w(\hat{d})$ and w_0 $(\hat{d})$ approaches to each other asymptotically and the values are respectively low. That is, if the terrain point is relatively far away from the grid node, the corresponding weighting function would be low, whether the location is considered exact or unknown.

$$w_0(\hat{d}; n) = w(\hat{d}; n) \equiv \hat{d}^{-n} \qquad 3.\ 24$$

$$\alpha = 1.1774 \quad \beta = 2.3 \quad \sigma = 25mm$$

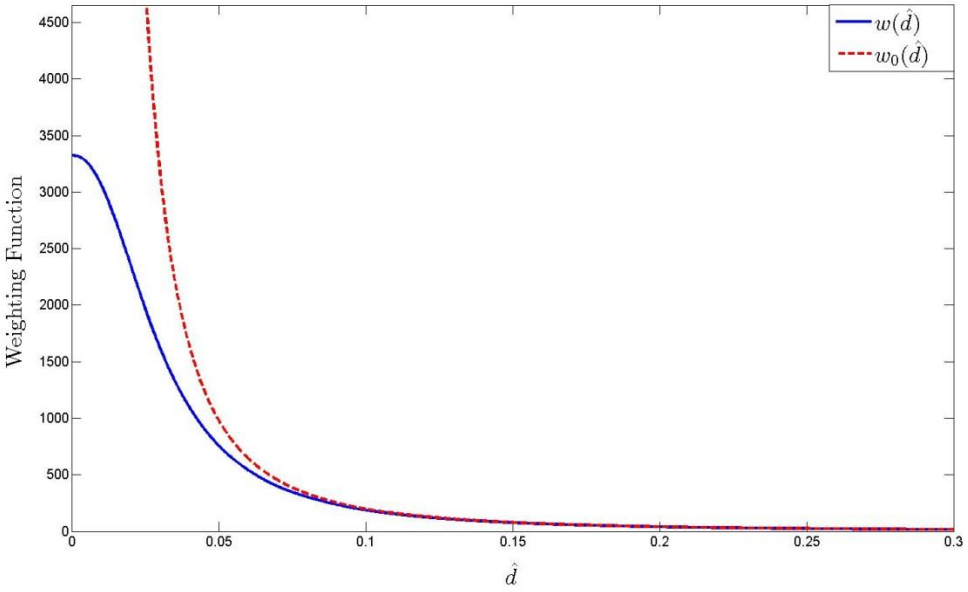

Figure 3.8. Comparison between $w(\hat{d})$ and $w_0(\hat{d})$

3.2 Probabilistic Terrain

In the previous section of this chapter, a weighting function assigning method is developed in which the uncertainty in the relative horizontal location of the measured terrain points and the grid nodes is accounted for. Based on the weighting function, a stochastic gridding method is developed to convert the measured cloud of terrain points into uniformly spaced format of probabilistic terrain comprising a series of gridding nodes. As the relative distance between the terrain point and the gridding node is uncertain, the nodal height should be stochastic to reflect the measurement uncertainty. The nodal height is estimated based on the surrounding measured terrain points' heights and the corresponding weighting functions. Noted the concept of probabilistic terrain is different from stochastic terrain. The stochastic terrain refers to the modeling technique applied on the gridded terrain profile. With the node height value provided by a deterministic gridding method, the whole terrain profile is considered to be a realization of

an underlying stochastic process [44]. The probabilistic terrain is the output of a stochastic gridding method, with obtained nodal heights represented by random variables instead of deterministic values.

3.2.1 Defining the Marginal Probability of Node Heights

The terrain data obtained with the Vehicle Terrain Measurement System (reviewed in Chapter 2) are discrete height samples of the original continuous terrain surface measured at various horizontal locations. These heights can be sorted so that the sorted measured discrete terrain heights compose vector $\{h_i\}$, where the index *i* indicates the i^{th} terrain point. To address the horizontal measurement uncertainty, the concept of Probabilistic Terrain is introduced. Probabilistic Terrain comprises a series of terrain gridding nodes, with heights considered to be random variables instead of deterministic values. The random variable at the j^{th} grid node is defined as Z_j and the set of random variable heights for all grid nodes is $\{Z_j\}$. Realizations of these random variables are defined such that they only take on realizations at the values belong to the vector $\{h_i\}$, i.e. the measured terrain heights. The set of indices for all terrain points is defined as *I*, the set of all grid nodes is *J* and set of all terrain heights is defined as *H*. The empirical marginal Probability Density Function (PDF) for a gridding node height to take a measured height value is defined as equation 3. 25.

$$P(\{Z_k = h_l\}) = \begin{cases} \dfrac{w(\hat{d}_{lk})}{\sum_l w(\hat{d}_{ik})} & h_l \in H, \forall l \\ 0 & otherwise \end{cases} \qquad \forall k \in J \tag{3. 25}$$

$$I = \{indices\ for\ measured\ terrain\ data\ points\}$$

$$J = \{indices\ for\ grid\ nodes\}$$

Where d_{ik} is the estimated relative horizontal distance between data point *i* and grid node *k*. The resultant empirical marginal Cumulative Distribution Function (CDF) of the k^{th} node height can be shown as a stair plot by Figure 3.9. At any measured height value $h_l \in H$, the discrete increment of C.D.F is

determined by the corresponding weighting as defined by equation 3. 25; there is no increment at other values. The resultant CDF is the *marginal* probability of Z_k, without regard to the realizations of heights at other grid nodes.

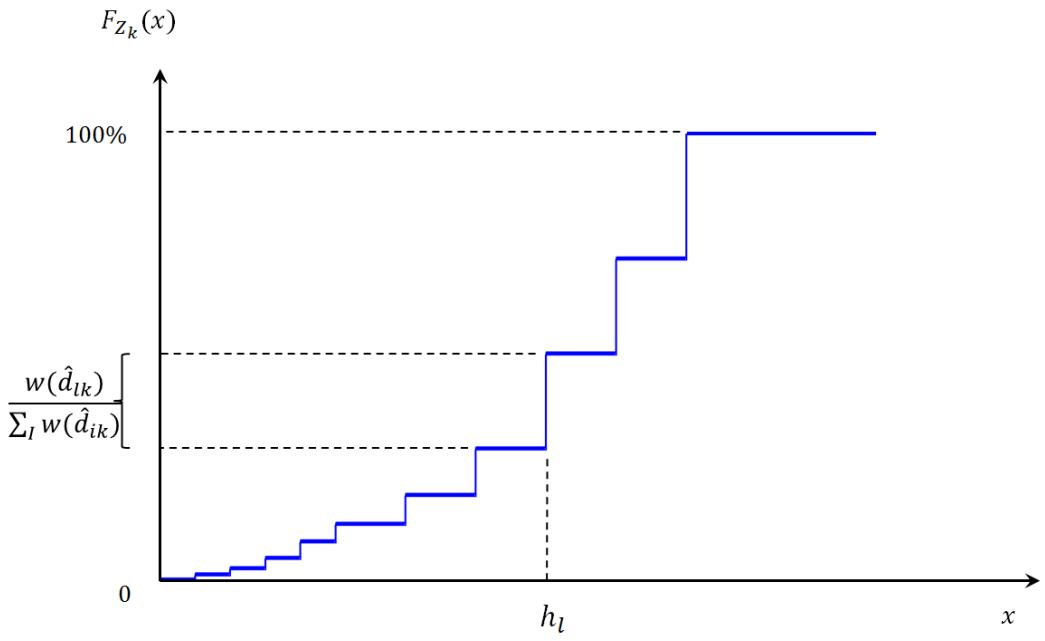

Figure 3.9. Cumulative Distribution Function of Z_k

3.2.2 Defining the Joint Probability of Node Heights

Once the marginal probability of the node heights is defined, the dependency relationship between nodes is required to generate realizations of a probabilistic terrain profile. For ease of explanation, this concept is developed without loss of generality for the case of a terrain profile (i.e., a sequence of heights along a single longitudinal path). The Joint probability is developed in terms of the conditional probability (i.e., given the previous node height realization, the uncertainty of the consecutive node height is provided). Since the relative location between the gridding nodes is assigned deterministically by the user, the corresponding contribution of the gridding node with known height can be evaluated by equation 3. 24.

The conditional probability for a grid node height to take on a particular height value $h_l \in H$, given the surrounding gridding nodes with known heights can be defined as equation 3. 26.

$$P(Z_k = h_l | H_{J'}) \triangleq \frac{w(\hat{d}_{lk})}{\sum_{i \in I} w(\hat{d}_{ik}) + \sum_{i \in J'} w_0(d_{ik})} \quad \forall k \in J \cap \overline{J'} \tag{3. 26}$$

$$J' = \{indices\ for\ known\ grid\ heights\}$$

$$H_{J'} = \{h_i \in H; i \in J'\}, \quad h_l \in H\ , \forall l$$

Consider the case when the k^{th} grid node is very close to a known grid height at index m. As the relative distance between the two gridding nodes approaches to zero ($d_{mk} \to 0$), the corresponding weight approaches infinity (see Figure 3.8). Therefore in this extreme case, conditional probability developed in equation 3. 26 can be rewritten as equation 3. 27.

$$\lim_{d_{mk} \to 0} w_0(d_{mk}) = \infty \quad \forall k \in J \cap \overline{J'}, m \in J' \tag{3. 27}$$

$$\lim_{w_0(d_{mk}) \to \infty} P(z_k = h_l | H_{J'}) = \lim_{w_0(d_{mk}) \to \infty} \frac{\frac{w(\hat{d}_{lk})}{w_0(d_{mk})}}{\frac{\sum_{i=1}^{N} w(\hat{d}_{ik})}{w_0(d_{mk})} + 1 + \frac{\sum_{i \in J'_{\overline{m}}} w_0(d_{ik})}{w_0(d_{mk})}} = 0$$

where

$$J'_{\overline{m}} = \{i | i \in J'\ and\ i \neq m\}$$

For completeness, the conditional probability that the k^{th} grid node assumes the same value as the known m^{th} grid node height is given in equation 3. 28.

$$P(z_k = z_m | H_{J'}) = \frac{w_0(d_{mk})}{\sum_I w(\hat{d}_{ik}) + \sum_{J'} w_0(d_{ik})} \tag{3. 28}$$

$$\forall k \in J \cap \overline{J'}, m \in J'$$

Since the k^{th} node coincides with the known m^{th} grid, the relative distance is zero and the weighting function approaches infinity. Therefore the conditional P.D.F. can be rewritten as equation 3. 29. It indicates trivially that if the gridding node height is known, the corresponding P.D.F is 100%.

$$P(z_k = z_m | H_{J'}) = \lim_{w_0(d_{mk})\to\infty} \frac{1}{\frac{\sum_{i\in I} w(\hat{d}_{ik})}{w_0(d_{mk})} + 1 + \frac{\sum_{i\in J'_{\overline{m}}} w_0(d_{ik})}{w_0(d_{mk})}} = 100\% \qquad 3.\ 29$$

$$\forall k \in J \cap \overline{J'}, m \in J'$$

If all the known grid nodes are much far away from the k^{th} grid node, then the total weight of the known gridding node approaches to zero. If there is at least one data point that is much closer to the k^{th} grid node than all the known grid nodes, then the impact of the known nodes becomes irrelevant and the conditional probability reverts to the marginal probability as shown by equation 3. 30.

$$\lim_{\sum_{J'} w_0(d_{ik})\to 0} P(z_k = h_l | H_{J'}) = \lim_{\sum_{J'} w_0(d_{ik})\to 0} \frac{w(\hat{d}_{lk})}{\sum_{i\in I} w(\hat{d}_{ik}) + \sum_{i\in J'} w_0(d_{ik})} \qquad 3.\ 30$$

$$= \frac{w(\hat{d}_{lk})}{\sum_{i\in I} w(\hat{d}_{ik})} = P(\{z_k = h_l\})$$

3.2.3 Realization Generation

Given the node height marginal probability and the dependency relationship, the realization of a probabilistic terrain can be generated by a stochastic gridding method. The measured terrain data of a section of MnRoad is used as the original measured terrain surface that needs to be gridded. The terrain

image can be shown as Figure 3.10. The terrain surface is smooth and there is a slight ascending trend from one end to the other.

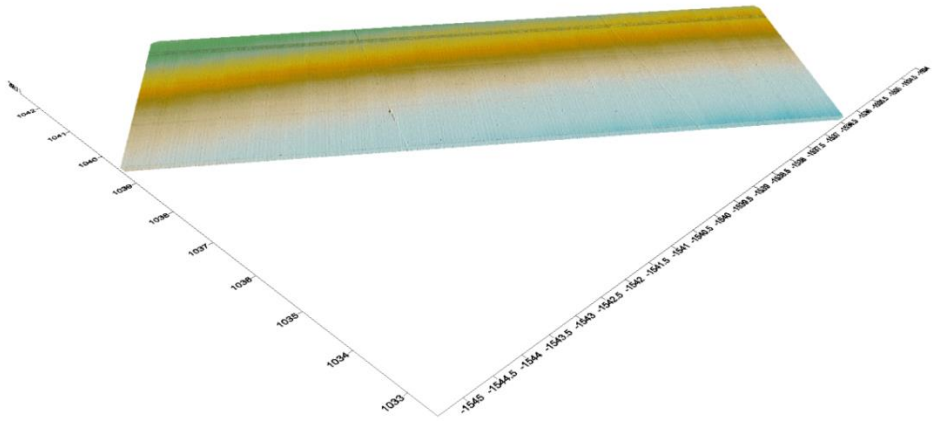

Figure 3.10. 3D terrain surface image of a section of MnRoad

The grid nodes are uniformly distributed along the center path of the of road surface as shown by Figure 3.11. The obtained gridded terrain profile represents the undulation of the center path.

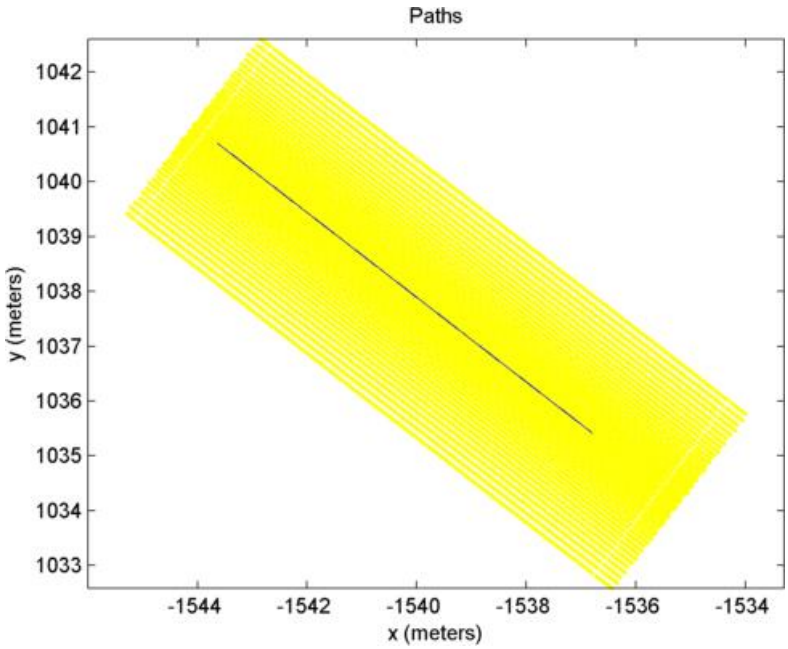

Figure 3.11. Center Path of a section of MnRoad

With the exponent n = 2.3 used in Equation 3. 23 and equation 3. 24, different realizations of the center path as a probabilistic terrain profile can be shown as Figure 3.12. The undulation is considerable because the n value is relatively small; therefore more terrain points around the gridding node are assigned with relatively large weights. At every horizontal location, the variability range of the terrain point height is larger. As a result the realization of the terrain profile is rougher with a small n value.

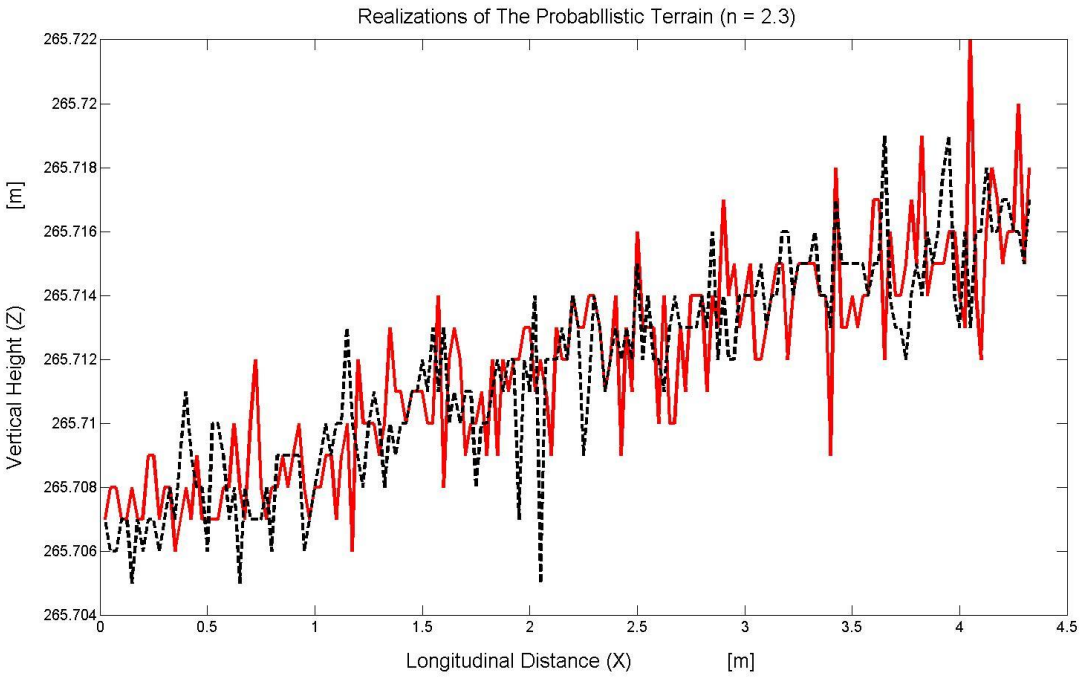

Figure 3.12. Realizations of the center profiles (n = 2.3)

As *n* increases, the importance (relative weight) of the known gridding node and the nearby terrain points increases. The terrain points farther away become less important. For the smooth measured terrain surface shown as Figure 3.10, the undulation of the probabilistic terrain profile realizations becomes smoother, as shown by Figure 3.13.

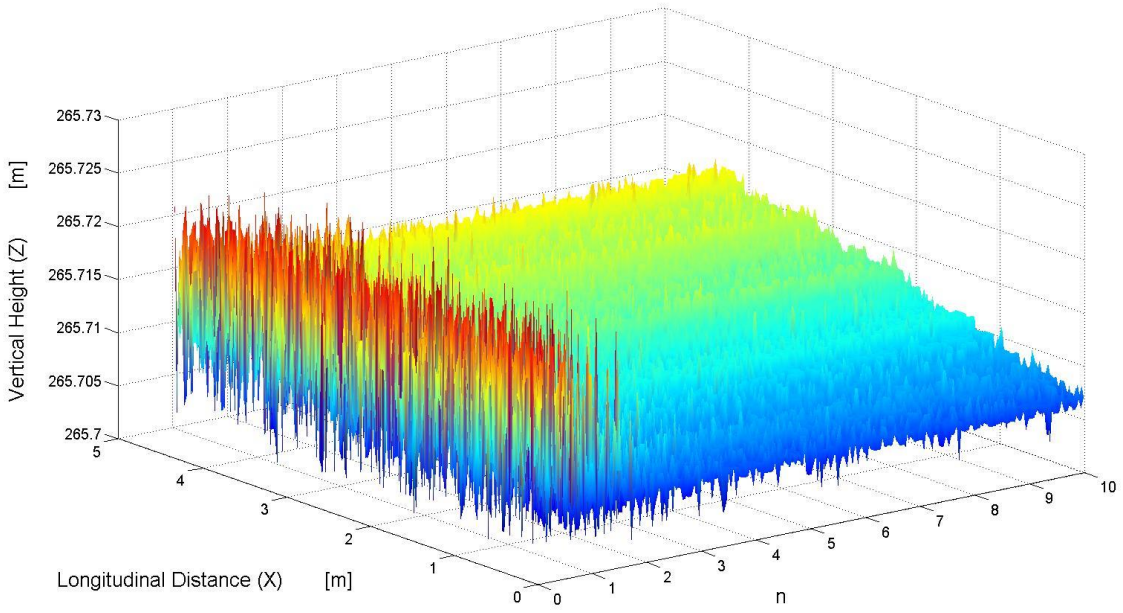

Figure 3.13. Realizations with different n

The undulation of the realization is also influenced by the measurement standard deviation σ as shown by Figure 3.14. As σ increases, the measurement uncertainty is larger. Consequently the locations of measured terrain points are considered more uncertain and assigned with smaller weights. The gridding node with known height takes a more important contribution in nodal height evaluation. Therefore the uncertainty variation range of the terrain height at each horizontal location decreases. The resultant realization is smoother. If the standard deviation keeps increasing to a very large value compared to adjacent gridding nodes spacing, the terrain point location is considered known with negligible certainty. The corresponding assigned weight is very low too. Therefore the nodal height evaluation is highly similar to the previous ones with known height. The resultant realization is a flat. A comparison of realizations with different standard deviations σ is shown by Figure 3.15. As the standard deviation increases, the realization becomes smoother, and the ascending slope is less obvious.

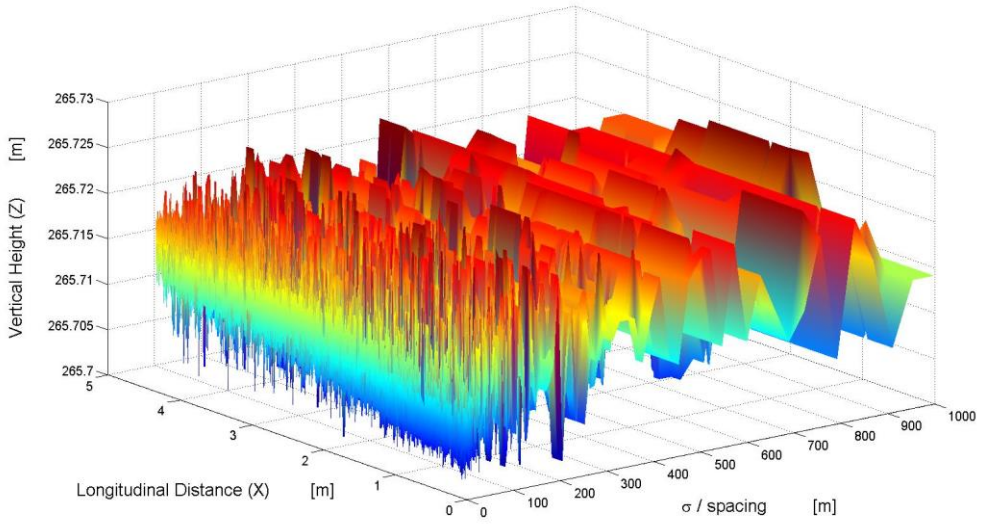

Figure 3.14. Realizations with different σ

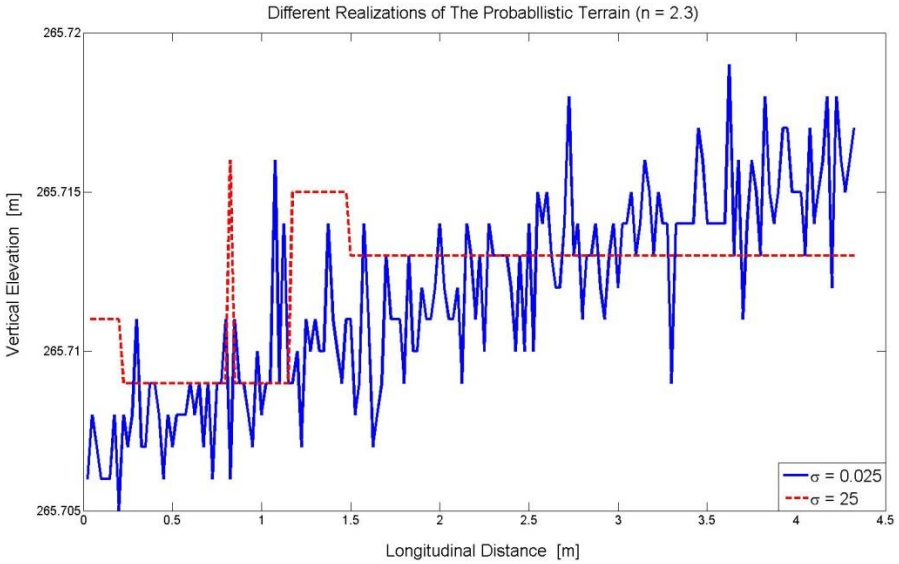

Figure 3.15. Comparison of two realizations with different σ

3.3 Discussion

The stochastic gridding method developed in this work convert the irregular spaced data into uniformly spaced configuration. The measured terrain surface comprises discrete samples of a continuous surface. An empirical Cumulative Distribution Function is developed from measured heights and the assigned weighting functions of the surrounding terrain points. It is used to define the marginal probability of an individual node height as well as the dependency relationship between the adjacent nodes. The obtained terrain profile is a probabilistic terrain composing of a series of uniformly spaced nodes. The height of each node is represented by a discrete random variable.

The weighting function assignment applied to develop the stochastic gridding method involves a user defined parameter *n*. As the value of *n* varies, the weighting functions of surrounding terrain points with respect the gridding nodes changes. The importance of the adjacent node heights varies too. If *n* approaches to infinite, the relative importance of the adjacent node heights is much larger than terrain points heights, according to Figure 3.8. Therefore the evaluated node height would be dominated by the known ones as shown by equation 3. 26. The contribution of the surrounding terrain points would be trivial. Therefore the nodal height evaluation process is dominated by the one with known heights. As *n* increases, the undulation of realization decreases as shown by Figure 3.13. With a very large n value the realization of a profile is a flat line, as the proceeding node height is determined by the previous one as show in Figure 3. 16. Future work focuses on the choice of different *n* value according to different application requirements.

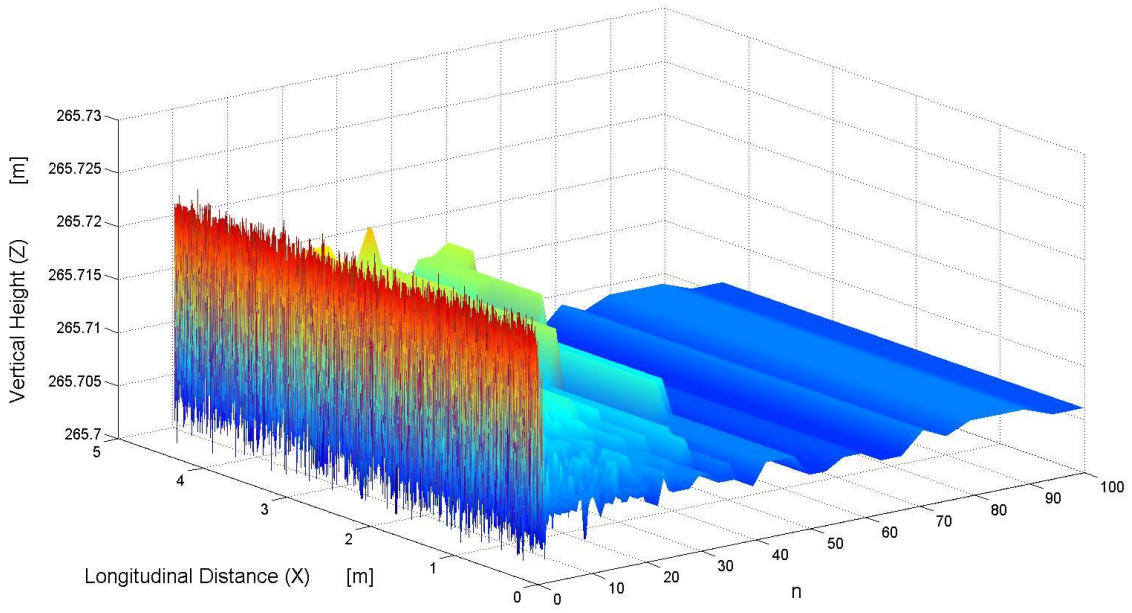

Figure 3. 16. Realizations with different *n* in logarithm scale

3.4 Conclusion

The main contribution of this work is the development of a stochastic gridding method to obtain a uniformly spaced probabilistic terrain from the measured cloud of points. The probabilistic terrain profile comprises a series of regularly spaced nodes with heights as random variables. A stochastic weighting function is assigned to include the measurement uncertainty with respect to the relative distance between the terrain data point and the grid node. The obtained stochastic representation is modeled to evaluate the weighting function in terms of the estimated relative distance. Based on the weighting function model, a stochastic gridding method is developed to include the horizontal measurement uncertainty in the nodal height evaluation. Realizations of the obtained probabilistic terrain profile are generated given an example of original measured terrain data. This work provide a stochastic gridding method to convert the irregular spaced cloud of terrain points into uniformly spaced probabilistic terrain, with gridding node

heights as random variable to represent the uncertainty in horizontal locations inherited from the terrain measurement procedure.

4. Static constraint mode tire model

One long-standing hurdle to accurate tire-terrain interaction analysis is the development of high fidelity tire models. As the non-deformable terrain imposes a unilateral geometric constraint to the tire, the desired tire model should capture the circumferential deformation and predict the spindle load due to the terrain excitation. The tire model should also bridge cracks in the pavement and envelope small bumps, and the resultant force should be obtainable through the circumferential deformation. As reviewed in Chapter 2, a considerable amount of research has been done in this area. Among all kinds of tire models, the in-plane the flexible ring model provides a simple and intuitive insight into the interaction between the terrain and tire.

In this work, a constraint mode tire model is developed to predict the tire circumferential displacements and the corresponding spindle force in tire-terrain interaction. The tire is modeled by a discretized flexible ring. Each individual tire segments is connected with the tire center by a spring. Hamilton's principle is used to model the spatially discretized tire segment as a flexible beam with radial stiffness. The required model parameters are reduced to two non-dimensional shape parameters and an overall stiffness factor. A parameter identification process is proposed to obtain the model parameters of a specific tire, as well as an admissible domain of these shape parameters due to the deformation limitations of a physical tire. The ability to accurately predict spindle forces is evaluated by comparing the simulation and experimental response for a cleat test. The constraint mode tire model provides a simple, accurate tire model for circumferential displacement estimates and vertical spindle force predictions. With the obtained load prediction, the stress and strain on the suspension component can be computed and the fatigue mode analysis can be conducted in the design stage when the adjustment is easier and cheaper.

The scope of this chapter is to develop a quasi-static in-plane tire model for deflection and force prediction in tire-terrain interaction. The tire is modeled as a flexible ring with springs connected to the center. Hamilton's principle is used to model the spatially discretized tire segment as a flexible beam with radial stiffness. The required model parameters are reduced to two non-dimensional shape parameters and an overall stiffness factor. An admissible region of the shape parameters is developed based on the deformation limitations of a physical tire. A system identification procedure is provided to calibrate the model parameters for specific tires. The bridging and enveloping properties of the tire model over irregular terrain excitation are demonstrated. The ability of the model to accurately predict the spindle force is evaluated by comparing simulation and experimental responses for a static cleat test. This work provides a simple, accurate tire model for circumferential displacement description and vertical spindle force prediction.

4.1 Model Development

In this section, a planar quasi-static tire model is developed that can be completely described by one stiffness parameter and two shape parameters. The system is assumed to be quasi-static. Therefore the equation of motion shown by equation 2. 1 can be simplified as equation 4. 1.

$$[\boldsymbol{K}]\{\boldsymbol{u}\} = \{\boldsymbol{f}\} \qquad 4.\ 1$$

For one tire segments, Hamilton's principle is applied as equation 4. 2.

$$\int_{t_1}^{t_2} (\delta U_b - \delta U_e - \delta U_s + \delta U_w) dt = 0 \qquad \forall t_1, t_2 \qquad 4.\ 2$$

The kinetic energy term vanishes under the quasi-static assumption. Each term and the corresponding virtual changes are computed as equations 4. 3 - 4. 6.

$$U_b = \frac{EIl}{2}\left(\frac{\partial^2 u}{\partial x^2}\right)^2 \qquad \delta U_b = EIl\frac{\partial^4 u}{\partial x^4}\delta u \qquad 4.\ 3$$

$$U_e = \frac{1}{2}\kappa l u^2 \qquad \delta U_e = \kappa l u \delta u \qquad 4.\ 4$$

$$U_s = \frac{Gblh}{2}\left(\frac{\partial u}{\partial x}\right)^2 \qquad \delta U_s = Glbh\frac{\partial^2 u}{\partial x^2}\delta u \qquad 4.\ 5$$

$$U_w = flu \qquad \delta U_w = fl\delta u \qquad 4.\ 6$$

The equation of motion for each segment is then simplified to equation 4. 7 by substituting equation 4. 3 - 4. 6 into the equation of motion shown by equation 4. 2.

$$EIl\frac{\partial^4 u}{\partial x^4} + \kappa l u + Glbh\frac{\partial^2 u}{\partial x^2} = fl \qquad 4.\ 7$$

For simplicity, the following parameters are defined in Table 4. 1. A, B, and C are stiffness parameters that are a function of physical tire properties and the number of segments, *N*. γ_1, γ_2 and γ_3 are considered the lumped parameters that are invariant with respect to a specific tire. It should be clear that each of the three stiffness parameters must be positive. F_n is the magnitude of the radial force on the n^{th} segment.

Table 4. 1. Tire stiffness parameters as a function of physical properties

$A = \frac{EI}{l^3} = \frac{EIN^3}{(2\pi R)^3} = \gamma_1 N^3$	Bending stiffness parameter

$B = \frac{Gbh}{l} = \frac{GbhN}{2\pi R} = \gamma_2 N$	Shear stiffness parameter
$C = \kappa l = \frac{2\kappa\pi R}{N} = \frac{\gamma_3}{N}$	Elastic stiffness parameter
$F_n = \frac{2f\pi R}{N}$	Force on each tire segment

The fourth spatial derivative of *u* for the n^{th} tire segment can be approximated by the radial displacements at adjacent points using a finite difference method; the approximation of u_0'''' with 2 adjacent points on each side as given in equation 4. 8.

$$u_n'''' \simeq \frac{u_{n-2} - 4u_{n-1} + 6u_n - 4u_{n+1} + u_{n+2}}{l^4} \qquad 4.\ 8$$

By substituting equation 4. 8 into 4. 7, the equation of motion for the radial degree of freedom for the nth tire segment can be expressed as equation 4. 9.

$$Au_{n-2} + (B - 4A)u_{n-1} + (6A - 2B + C)u_n + (B - 4A)u_{n+1} + Au_{n+2} = F_n \qquad 4.\ 9$$

The stiffness matrix $[\boldsymbol{K}]$ is a circulant Toeplitz matrix, as shown in equations 4. 10, due to the circular shape of the physical tire. It can be decomposed into two parts: k_0 as the overall stiffness factor and the matrix $[\boldsymbol{\alpha}]$ to determine the deformed tire shape [45]. Note that matrix $[\boldsymbol{\alpha}]$ is only a function of two shape parameters (α_1 and α_2) and has a circulant form denoted by $circ$ where the vector $\{a_i\} = [\ a_0 \quad a_1 \quad a_2 \quad \dots \quad a_{n-1}]$ is the first row of $[\boldsymbol{\alpha}]$ and considered to be the characterization vector of circulant matrix $[\boldsymbol{\alpha}]$, with $a_0 = 1, a_1 = a_{n-1} = \alpha_1, a_2 = a_{n-2} = \alpha_2, a_3 = a_4 = \cdots = a_{n-3} = 0$.

$$[\boldsymbol{K}] = k_0 \begin{bmatrix} 1 & \alpha_1 & \alpha_2 & 0 & \cdots & \alpha_2 & \alpha_1 \\ \alpha_1 & 1 & \alpha_1 & \alpha_2 & \cdots & 0 & \alpha_2 \\ \alpha_2 & \alpha_1 & 1 & \alpha_1 & \vdots & 0 & 0 \\ 0 & \alpha_2 & \alpha_1 & 1 & \cdots & 0 & 0 \\ \vdots & \vdots & \vdots & \vdots & \vdots & \vdots & \vdots \\ \alpha_1 & \alpha_2 & 0 & 0 & \cdots & \alpha_1 & 1 \end{bmatrix} = k_0[\boldsymbol{\alpha}] = k_0 circ(\{a_i\}) \qquad 4.\ 10$$

$$\{a_i\} = [\, a_0 \quad a_1 \quad a_2 \quad \ldots \quad a_{n-1}]$$

The three parameters composing the stiffness matrix $[\boldsymbol{K}]$ can be written in terms of modeling parameters as equations 4. 11 [45].

$$k_0 = 6A - 2B + C \qquad 4.\ 11$$

$$\alpha_1 = \frac{B - 4A}{6A - 2B + C} = \frac{B - 4A}{k_0},$$

$$\alpha_2 = \frac{A}{6A - 2B + C} = \frac{A}{k_0}$$

4.2 System Identification

From the equation of motion 4. 1 it can be seen that the relationship between tire deformation and the generated force depends on the stiffness matrix $[\boldsymbol{K}]$, which can be decomposed into overall stiffness factor k_0 and the shape matrix $[\boldsymbol{\alpha}]$ comprising two parameters α_1 and α_2. Given the uneven terrain excitations, the choice of α_1 and α_2 values determines the deformed tire shape. With the discretized ring model, the radial deformation associated with each individual segment composes of a vector. As the tire is modeled under quasi-static assumption, the radial deformation vector should be dominated by low frequency content, as shown by the right figure in Figure 4. 1. It is evident that under quasi-static condition, the left high frequency dominated deformed shape is not possible for a physical tire. Therefore

the values of α_1 and α_2 need to be properly selected to reflect the actual tire deformation under quasi-static condition.

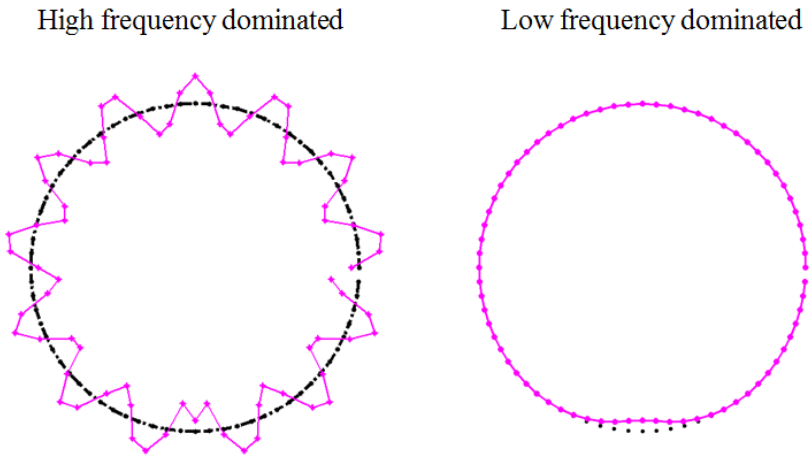

Figure 4. 1. Comparison of the deformed tire shape with different choice of shape parameters values

From Table 4. 1, it can be seen that if the lumped parameters A,B and C change the same percentage, the shape parameters α_1 and α_2 maintain, while the overall stiffness factor k_0 changes. The stiffness factor k_0 value determines the reaction force of the deformed tire with respect to the excitations. Given a specific terrain section interfering with tire, if k_0 value increases, the reaction forces generated by the tire deformation increase too, as well as the resultant spindle force. Provided a flat terrain profile underneath the tire with certain interference, the relationship between the spindle forces and k_0 is linear, as shown in Figure 4. 2.

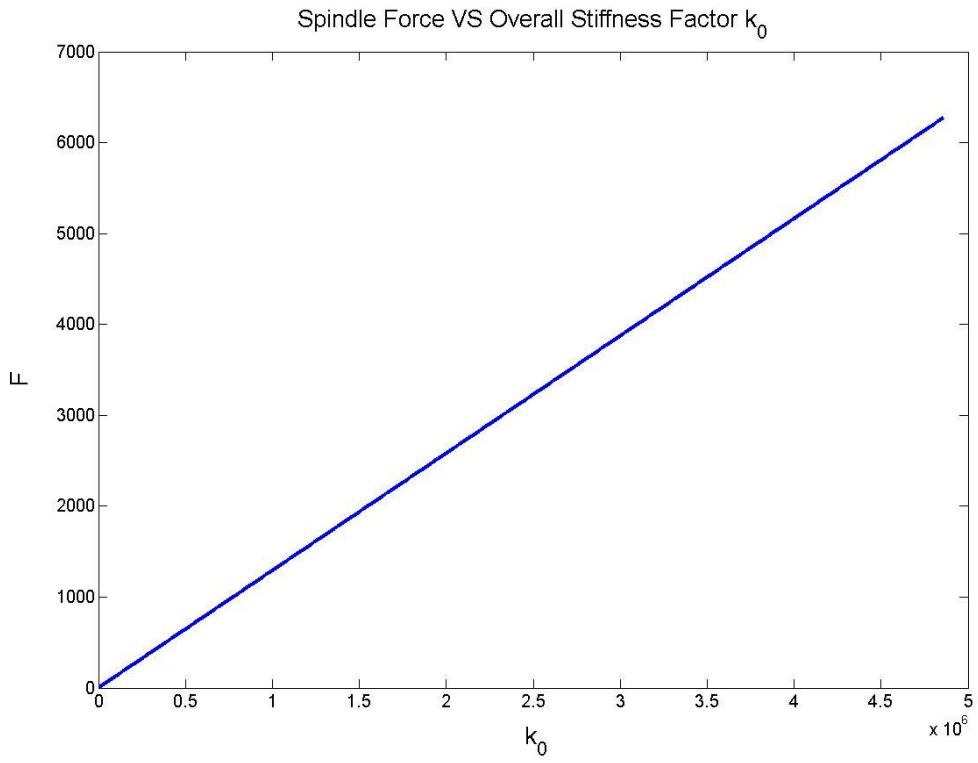

Figure 4. 2. Spindle Force VS. Overall Stiffness Factor

To provide accurate force and displacement prediction, a parameter identification process is then developed to provide a standard practice to calibrate the model for different tires.

4.2.1 Shape parameters

To identify the shape parameters α_1 and α_2, a single point excitation is applied upon the tire model quasi-statically, resulting in one active degree of freedom. The index will be assigned such that this active point is the first degree of freedom as shown by Figure 4. 3. The resultant tire shape is restrained by certain physical restrictions which manifest themselves as parameter constraints on the shape parameters α_1 and α_2. These physical constraints include the positive bending, shear and radial stiffness and the frequency

stability of the deformed tire shape. An admissible region of the shape parameters can be derived from the constraints.

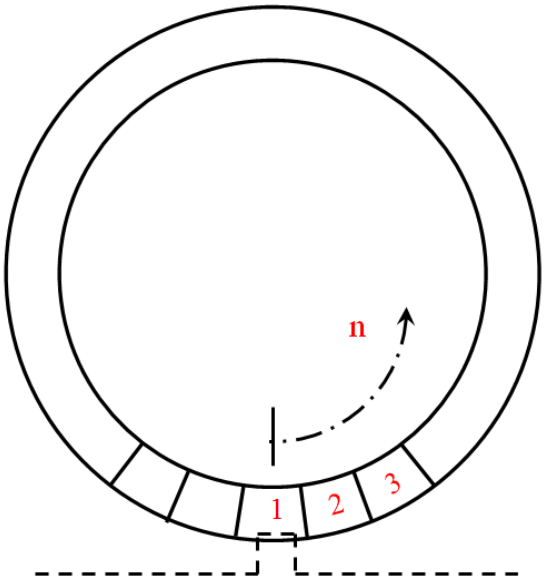

Figure 4. 3. Indexing of the tire segment

From the equation of motion shown as 4. 1, and the stiffness matrix partition shown as equation 4. 10 , the deformed tire shape can be computed as equation 4. 12.

$$\{\boldsymbol{u}\} = \begin{Bmatrix} u^a \\ \boldsymbol{u^o} \end{Bmatrix} = [\boldsymbol{K}]^{-1} \begin{Bmatrix} f^a \\ \boldsymbol{0} \end{Bmatrix} = [\boldsymbol{\alpha}]^{-1} \begin{Bmatrix} \frac{f^a}{k_0} \\ \boldsymbol{0} \end{Bmatrix} \qquad 4.\ 12$$

To obtain the description of the deformed tire shape $\{\boldsymbol{u}\}$, the inverse of the shape matrix $[\boldsymbol{\alpha}]^{-1}$ is required. On the other hand, to identify the shape parameters α_1 and α_2, the deformed tire shape is also necessary. For simplification, only one segment is assumed to be active. Since the indexing for the tire segments is arbitrary, the active segment can be considered as the first. Therefore, u^a and $\frac{f^a}{k_0}$ are scalar

values. The deformed shape of the tire $\{\boldsymbol{u}\} = \begin{Bmatrix} u^a \\ \boldsymbol{u^o} \end{Bmatrix}$ can be described by an vector composed of the first column of the matrix $[\boldsymbol{\alpha}]^{-1}$ times the constant factor $\frac{f^a}{k_0}$.

Recall from the lower equation in 4. 114. 10 that the vector $\{a_i\} = [\, a_0 \quad a_1 \quad a_2 \quad \dots \quad a_{n-1}]$ is the first row of $[\boldsymbol{\alpha}]$ and is the characterization vector of $[\boldsymbol{\alpha}]$, with $a_0 = 1, a_1 = a_{n-1} = \alpha_1, a_2 = a_{i-2} = \alpha_2, a_3 = a_4 = \cdots = a_{i-3} = 0$. The corresponding eigenvalue vector of $[\boldsymbol{\alpha}]$, $\{\lambda_k\}$, can be calculated by applying the Discrete Fourier Transform to the vector $\{a_i\}$ as equation 4. 13 [46].

$$\{\lambda_k\} = \mathcal{F}(\{a_i\}) \qquad 4.\ 13$$

$$\lambda_k = \sum_{i=0}^{n-1} a_i W_k^i \qquad k = 0,1,2,\dots,n-1$$

$$W_k = e^{-\frac{2\pi k}{n} j}$$

The corresponding k^{th} eigenvector $v^{(k)}$ can be expressed as equation 4. 14.

$$\boldsymbol{v}^{(k)} = \frac{1}{\sqrt{n}}(W_k^0 \quad W_k^1 \quad W_k^3 \quad \cdots \quad W_k^{n-1})' \quad k = 0,1,2,\dots,n-1 \qquad 4.\ 14$$

The eigenvector matrix $[\boldsymbol{V_k}]$ is defined as a collection of eigenvectors at each column, shown as equation 4. 15.

$$[\boldsymbol{V_k}] = [\boldsymbol{v^{(0)}} \quad \boldsymbol{v^{(1)}} \quad \boldsymbol{v^{(2)}} \quad \dots \quad \boldsymbol{v^{(n-1)}}] \qquad 4.\ 15$$

The circulant matrix $[\boldsymbol{\alpha}]$ can be diagonalized by $[\boldsymbol{V_k}]$ as equation 4. 16, where $[\boldsymbol{V_k}]^H$ is the Hermitian matrix of $[\boldsymbol{V_k}]$.

$$[\boldsymbol{\alpha}] = [\boldsymbol{V_k}]^H \, diag(\lambda_0 \quad \cdots \quad \lambda_{N-1})[\boldsymbol{V_k}] \qquad 4.\ 16$$

The inverse of $[\boldsymbol{\alpha}]$ can be derived as equation 4. 17. The inverse matrix of $[\boldsymbol{\alpha}]$ is also a circulant matrix because it has the same diagonalized form as the original matrix $[\boldsymbol{\alpha}]$, shown as equation 4. 16. The eigenvalue vector of $[\boldsymbol{\alpha}]^{-1}$ is simply $\left\{\frac{1}{\lambda_k}\right\}$ and shares the same eigenvectors as $[\boldsymbol{\alpha}]$, as shown in equation 4. 17.

$$[\boldsymbol{\alpha}]^{-1} = [\boldsymbol{V_k}]^H diag(\frac{1}{\lambda_0} \quad \cdots \quad \frac{1}{\lambda_{N-1}})[\boldsymbol{V_k}] \qquad 4.\ 17$$

Due to the symmetric and sparse property of the characterization vector $\{a_i\}$ associated with the shape matrix $[\boldsymbol{\alpha}]$, the eigenvalue of $[\boldsymbol{\alpha}]$ can be simplified as equation 4. 18. The simplification derivation detail is shown in Appendix Section 1.

$$\lambda_k = 4\alpha_2 cos^2\left(\frac{2\pi k}{n}\right) + 2\alpha_1 cos\left(\frac{2\pi k}{n}\right) + 1 - 2\alpha_2 \qquad 4.\ 18$$

$$k = 0,1,2 \ldots N-1$$

The characteristic vector of the inverse matrix, i.e. the first row of $[\boldsymbol{\alpha}]^{-1}$, is defined as $\{\beta_i\}$. It can be obtained by performing an Inverse Discrete Fourier Transform on the eigenvalue vector of $[\boldsymbol{\alpha}]^{-1}$, i.e. $\left\{\frac{1}{\lambda_i}\right\}$. The inverse matrix $[\boldsymbol{\alpha}]^{-1}$ also has a circulant form as shown by equation 4. 19.

$$[\boldsymbol{\alpha}]^{-1} = \boldsymbol{B} = Circ(\{\beta_i\}) \qquad 4.\ 19$$

$$\{\beta_i\} = [\beta_0, \beta_1, \beta_2, \ldots, \beta_{n-2}, \beta_{n-1}] = \mathcal{F}^{-1}(\left\{\frac{1}{\lambda_i}\right\})$$

$$\beta_k = \frac{1}{n}\sum_{i=0}^{n-1} \frac{1}{\lambda_i} W_k^{-i} \qquad k = 0,1,2, \ldots, n-1$$

As shown in Appendix Section 1, $\{\lambda_k\}$ is symmetric except the first term $\lambda_0 = 1$, i.e. $\lambda_k = \lambda_{N-k}, k = 1,2,\dots,N-1$. Due to the symmetry of $\{\lambda_k\}$, $\{\beta_i\}$ is symmetric too, i.e. $\beta_k = \beta_{n-k}, k = 1,2,\dots,n-1$. The detail is provided in Appendix Section 1. From equation 4. 12 and the symmetric property of $\{\beta_i\}$, the resultant deformed tire shape with one active segment can be computed as equation equation 4. 19.

$$\{\boldsymbol{u}\} = [\boldsymbol{\alpha}]^{-1}\begin{Bmatrix}\frac{f^a}{k_0}\\0\\\vdots\\0\end{Bmatrix} = \begin{bmatrix}\beta_0 & \beta_1 & \beta_2 & \beta_3 & \cdots & \beta_{n-2} & \beta_{n-1}\\ \beta_{n-1} & \beta_0 & \beta_1 & \beta_2 & \cdots & \beta_{n-3} & \beta_{n-2}\\ \beta_{n-2} & \beta_{n-1} & \beta_0 & \beta_1 & \vdots & \beta_{n-4} & \beta_{n-3}\\ \beta_{n-3} & \beta_{n-2} & \beta_{n-1} & \beta_0 & \cdots & \beta_{n-5} & \beta_{n-4}\\ \vdots & \vdots & \vdots & \vdots & \vdots & \vdots & \vdots\\ \beta_1 & \beta_2 & \beta_3 & \beta_4 & \cdots & \beta_{n-1} & \beta_0\end{bmatrix}\begin{Bmatrix}\frac{f^a}{k_0}\\0\\\vdots\\0\end{Bmatrix} \quad 4.\ 20$$

$$= \frac{f^a}{k_0}\begin{Bmatrix}\beta_0\\\beta_1\\\beta_2\\\beta_3\\\vdots\\\beta_{n-1}\end{Bmatrix}$$

Therefore the deformed tire shape vector $\{\boldsymbol{u}\}$ is proportional to the vector $\{\beta_i\}$ with a factor $\frac{f^a}{k_0}$. $\{\beta_i\}$ is obtained by applying Inverse Discrete Fourier Transformation on $\left\{\frac{1}{\lambda_i}\right\}$, which is determined by the shape coefficients α_1 and α_2 as shown by 4. 13.

Based on the derivation in the system identification analysis, a standard procedure is proposed to determine the shape parameters α_1, α_2 for a particular tire. A cleat with the width of $\frac{2\pi R}{N}$ is required, where R is the tire radius and N is the number of segments. N should be large enough to validate the small angle assumption used in the model development. The steps are as follows:

1) Perform the cleat test and record the tire shape deformation as a vector with the length N as $\{u_i\}$
2) Perform inverse Fast Fourier Transform to the deformed shape vector as $\mathcal{F}^{-1}(\{u_i\}) = \frac{f_a}{k_0}\left\{\frac{1}{\lambda_i}\right\}$
3) Obtain the vector $\frac{1}{\mathcal{F}^{-1}(\{u_i\})} = \frac{k_0}{f_a}\{\lambda_i\}$
4) Fit a parabolic curve $y = p_1x^2 + p_2x + p_3$ to $\frac{1}{\mathcal{F}^{-1}(\{u_i\})}$ and obtain the parameters p_1, p_2 and p_3
5) The shape parameters can be obtained by $\alpha_1 = \frac{p_2}{2p_3+p_1}$, $\alpha_2 = \frac{p_1}{4p_3+2p_1}$

This shape parameter identification technique is demonstrated in an example in the 4.3 Model Validation section. However, as demonstrated in Figure 4. 1, it is critical to identify values for these shape parameters that are physically realizable. Therefore a study of the admissible range of α_1 and α_2 is conducted for the model accuracy. The challenge is that α_1 and α_2 are each lumped parameters comprising several of the tire physical properties and these two parameters must determine the deformed tire shape with respect to the terrain excitations. Several constraints are applied in the following sections.

Physical Constraints:

The definition of the positive sense for the deflections and corresponding forces are defined such that overall tire stiffness, k_0 must be positive. Similarly, since the tire stiffness parameters, *A*, *B*, and *C* as shown in Table 4. 1must be positive, the following relationships for the tire shape parameters, α_1 and α_2, must be positive. Therefore the physical constraints applied on α_1 and α_2 can be obtained as the inequalities shown in 4. 21 and it can be plotted as Figure 4. 4, where the white area denotes the admissible region.

$$\alpha_2 = \frac{A}{k_0} > 0 \qquad 4.\ 21$$

$$\alpha_1 + 4\alpha_2 = \frac{B}{k_0} > 0$$

$$2\alpha_1 + 2\alpha_2 + 1 = \frac{C}{k_0} > 0$$

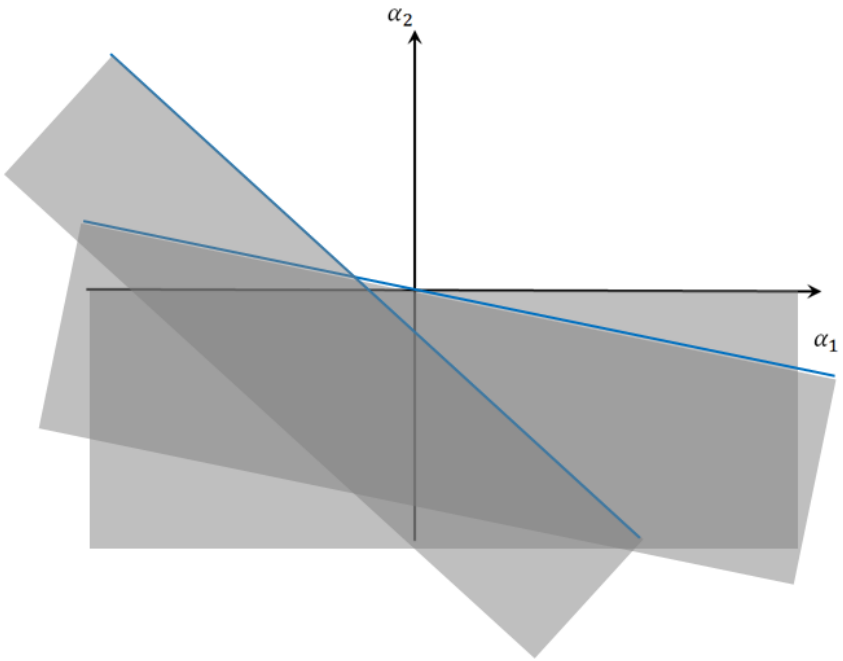

Figure 4. 4. Admissible region with physical constraints applied

Frequency Constraints

As equation 4. 17 shows, the inverse of the shape matrix $[\boldsymbol{\alpha}]^{-1}$ has a circulant form and the corresponding characterization vector $\{\beta_i\}$ can be computed by Inverse Discrete Fourier Transform of the vector $\left\{\frac{1}{\lambda_k}\right\}$, where $\{\lambda_k\}$ is the eigenvalue vector of the original shape matrix $[\boldsymbol{\alpha}]$. In the case that only one segment is active and the segment numbering starts with the active segment (as shown in Figure 4. 3),

the radial displacement vector is represented by the characterization vector as $\{\boldsymbol{u}\} = \frac{f^a}{k_0}\{\beta_i\}$ as shown by equation 4. 20. $\left\{\frac{1}{\lambda_k}\right\}$ can be considered the weight of each frequency in the composition of the vector $\{\beta_i\}$. If there exists one element $\frac{1}{\lambda_m} \in \left\{\frac{1}{\lambda_k}\right\}$ that approaches infinity, the characterization vector $\{\beta_i\}$ would be dominated by the corresponding frequency term $cos\left(\frac{2\pi km}{N}\right)$. Under this circumstance the radial deformation vector would be periodic.

Examples of this periodic shape behavior are shown in Figure 4. 5. The total number of tire segments is N = 72. The first example shown in (a) is when *m=0* and the radial deformation vector is constant. In this case the circumference of the tire is contracting which invalidates the circumferential length constraint of the inextensibility assumption. In the second case, *m=1*, the tire takes on the deflection of a rigid-body as shown in (b). Examples of higher order shapes are shown as (c) through (e), demonstrating higher order vibrational modes of the tire corresponding to higher order frequency excitations. If any single periodic shape behavior term dominates over the others, the tire deflection fails to reflect a real tire response under the quasi-static condition. Therefore none of the periodic shape should be dominant.

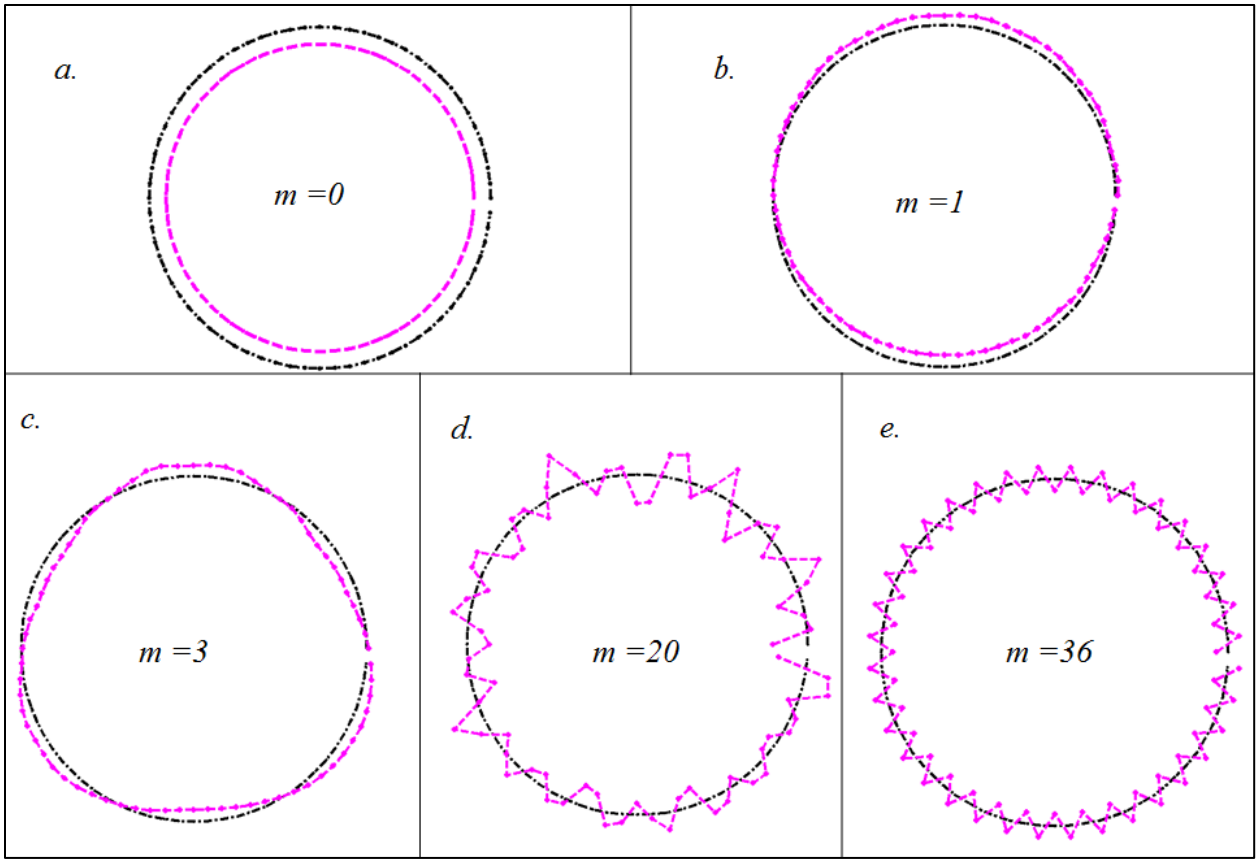

Figure 4. 5. Periodic shape behavior of the constraint mode terms

According to the previous analysis of the periodic behaviors, since the constraint mode model is assumed to be quasi-static, two Frequency Constraints are required as follows.

1. None of the purely periodic shapes are permissible. Therefore, none of the elements of the vector $\left\{\frac{1}{\lambda_k}\right\}$ should approach infinity, so that the constraint on the eigenvalue due to the frequency stability must be enforced as given in equation 4. 22 and in practice these eigenvalues should not approach zero.

$$\lambda_k \neq 0, \quad \forall k \in \{0,1,2 \ldots n-1\} \qquad 4.\ 22$$

2. Due to the quasi-static assumption, the radial deformation vector should be low-frequency dominated. Therefore the frequency weight vector $\left\{\frac{1}{\lambda_i}\right\}$ should be relatively large in the low frequency range, i.e. $k = 0$, and should be relatively small in the high frequency range, i.e. $k = \frac{n}{2}$.

Next the conditions on the shape parameters, α_1 and α_2, that satisfy these two Frequency Constraints are developed. From equation 4. 18, λ_k can be rewritten as a function of a new lumped variable ξ as equation 4. 23. The detail is provided in Appendix Section 1.

$$\lambda_k(\xi) = 4\alpha_2\xi^2 + 2\alpha_1\xi + 1 - 2\alpha_2 \qquad \xi \in [-1,1]$$
$$\xi = cos\left(\frac{2\pi k}{N}\right) \quad k = 0,1,2 \ldots n-1 \tag{4. 23}$$

Therefore the constraint shown as inequality 4. 22 can be rewritten in terms of ξ as 4. 24.

$$\lambda_k(\xi) \neq 0, \forall \xi \in (-1,1) \tag{4. 24}$$

Note that the variable ξ can only take on discrete values (it is not a continuous function) that are determined by the number of segments, *N*. The function $\lambda_k(\xi)$ can be written as a continuous function of ξ, but only approaches a continuous function as *N* approaches infinity. In the strict sense then, it may be possible to choose *N* such that inequality 4. 24 is satisfied for any given set of α_1 and α_2. However, in practice the eigenvalues $\lambda_k(\xi)$ should not *approach* zero for any choice of *N*. In order to avoid the case in which the eigenvalue approaches zero (whether or not is equals zero exactly), the discrete function $\lambda_k(\xi)$ is considered in this work to be a continuous function and no points along this continuum must be

allowed to be equal to zero. In this way the discrete values that the true discrete function can assume will not produce an eigenvalue that approaches zero, i.e. no terms in $\left\{\frac{1}{\lambda_i}\right\}$ approaches to infinity.

The continuous representation of the function $\lambda_k(\xi)$ is a parabola. From the physical constraints shown in the inequality 4. 21, α_2 is positive. According to the derivation shown in Appendix Section 1, the parabolic curve $\lambda_k(\xi)$ faces upwards. Depending on the sign of the discriminant of the equation $\lambda_k(\xi) = 0$, the parabolic curve may or may not have intersections with horizontal ξ axis. The three possibilities of the discriminant sign are addressed separately as follows.

1. Discriminant $\Delta = 4\alpha_1^2 - 16\alpha_2(1 - 2\alpha_2) < 0$

In this case, according to the derivation in Appendix Section 1, the parabolic equation doesn't intersect the horizontal ξ axis, and $\lambda_k(\xi)$ is always positive. The parabola curve of $\lambda_k(\xi)$ can be shown as Figure 4. 6. Therefore the first Frequency Constraint , that the eigenvalues do not approach zero, always holds in this case. The resulting constraint on the shape parameters is derived knowing the sign of the discriminant Δ, leading to the inequality constraint represented by 4. 25.

$$\frac{\alpha_1^2}{\frac{1}{2}} + \frac{(\alpha_2 - \frac{1}{4})^2}{\frac{1}{16}} < 1 \qquad 4.\ 25$$

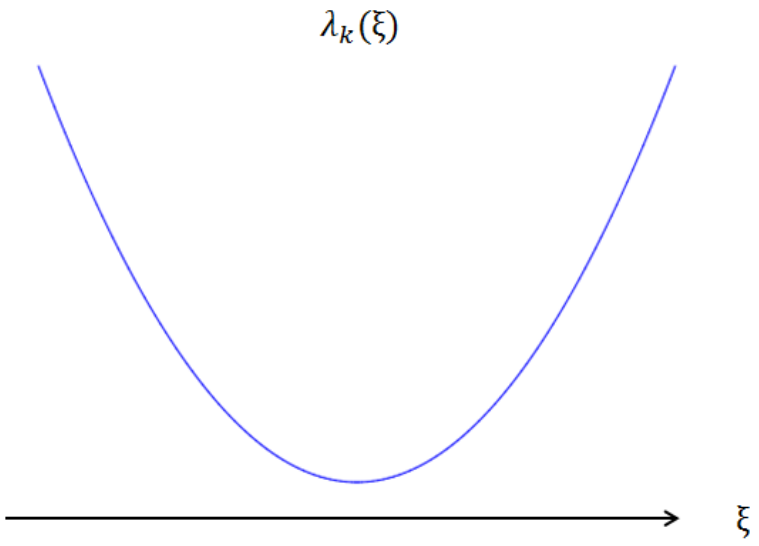

Figure 4. 6. Parabola curve of $\lambda_k(\xi)$ with discriminant $\Delta < 0$

The second Frequency Constraint (i.e. the radial deformation vector should be low-frequency dominated and the frequency weighting vector $\left\{\frac{1}{\lambda_k}\right\}$ should be relatively large in the low frequency range, i.e. $k = 0$, or $\xi = -1$; and should be relatively small in the high frequency range, i.e. $k = \frac{N}{2}$, or $\xi = 1$) can be expressed by an inequality shown as 4. 26.

$$\lambda_k(1) < \lambda_k(-1) \qquad 4.\ 26$$

In this case, $\lambda_k(\xi) > 0, \forall \xi \in \mathbb{R}$, therefore the low frequency domination requirement constraints can be further simplified as 4. 27.

$$\alpha_1 < 0 \qquad 4.\ 27$$

2. Discriminant $\Delta = 4\alpha_1^2 - 16\alpha_2(1-2\alpha_2) > 0$

The first Frequency Constraint (i.e., the eigenvalues do not approach zero) is enforced by considering points at which the parabolic curve intersects the ξ axis. These points of intersection occur at the horizontal coordinates shown by equation 4. 28.

$$\xi_1 = -\frac{\alpha_1 + \sqrt{4\alpha_1^2 - 16\alpha_2(1-2\alpha_2)}}{4\alpha_2} \qquad 4.\ 28$$

$$\xi_2 = -\frac{\alpha_1 - \sqrt{4\alpha_1^2 - 16\alpha_2(1-2\alpha_2)}}{4\alpha_2}$$

Where $\xi_2 > \xi_1$ always holds since $\sqrt{4\alpha_1^2 - 16\alpha_2(1-2\alpha_2)} > 0$ and $\alpha_2 > 0$. Since the first Frequency Constraint must be enforced, the parabolic curve $\lambda_k(\xi)$ must not cross the horizontal axis in the range $\xi \in (-1,1)$. So within the range, there are three possible cases for the parabolic function $\lambda_k(\xi)$ and each of them is discussed separately.

2. - Case 1:

In this case, the range $\xi \in (-1,1)$ falls on the left side of the symmetric axis, the curve monotonically decreases as ξ increases and $\lambda_k(\xi)$ is positive, as shown by Figure 4. 7. Therefore the inequality shown as 4. 29 would always hold.

$$\lambda_k(-1) > \lambda_k(1) > 0 \qquad 4.\ 29$$

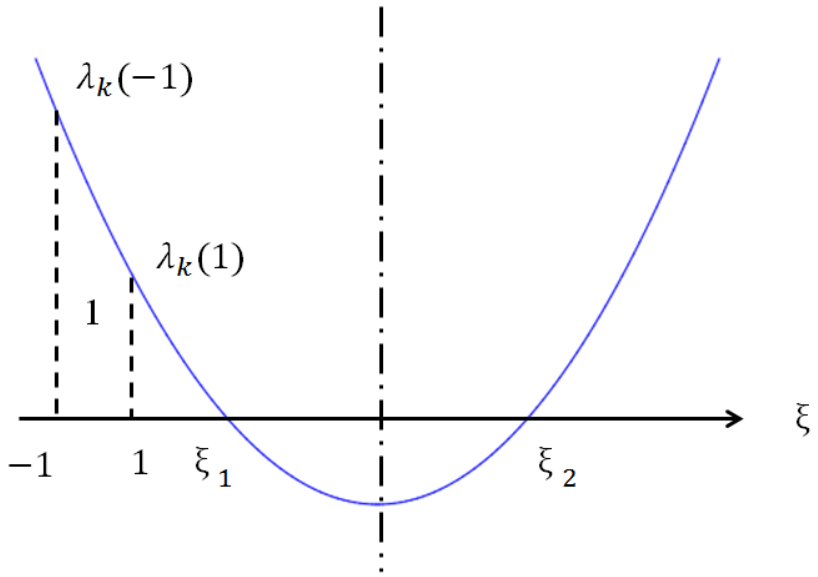

Figure 4. 7. Plot of the parabolic curve representing $\lambda_k(\xi)$, discriminant $\Delta > 0$ - Case 1

It can be further simplified as the inequality expressed as 4. 30. The derivation detail is provided in Appendix Section 1.

$$2\alpha_1 + 2\alpha_2 + 1 > 0 \qquad 4.\ 30$$

$$\alpha_1 + 4\alpha_2 < 0$$

$$\alpha_2 > 0$$

$$4\alpha_1^2 - 16\alpha_2(1 - 2\alpha_2) > 0$$

However the second inequality above contradicts the physical constraints expressed by 4. 21. Therefore case 1 is not valid.

2. - Case 2:

In this case, the range $\xi \in (-1,1)$ falls on both sides of the symmetric axis, the curve first monotonically decreases and then increases as ξ increases and $\lambda_k(\xi)$ is negative, as shown by Figure 4. 8. Therefore the inequality shown as 4. 31 would always hold.

$$\lambda_k(-1) < 0 \qquad 4.\ 31$$
$$\lambda_k(1) < 0$$

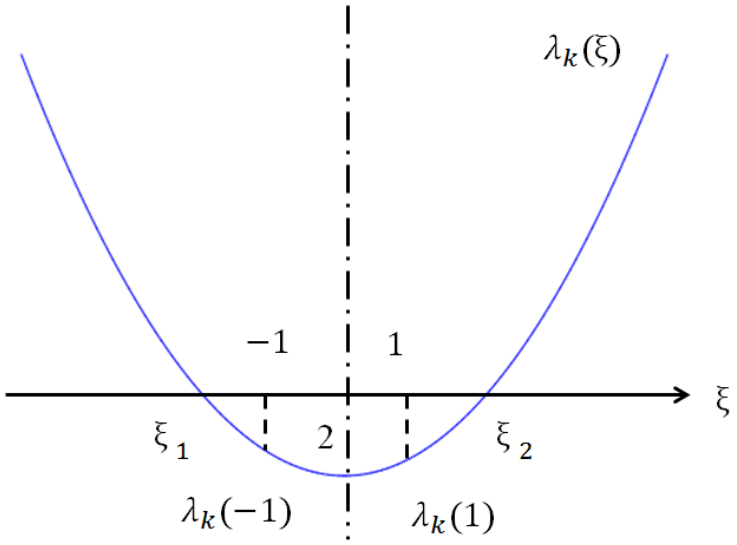

Figure 4. 8. Plot of the parabolic curve representing $\lambda_k(\xi)$, discriminant $\Delta > 0$ - Case 2

It can be simplified to the inequality shown as 4. 32.

$$2\alpha_1 + 2\alpha_2 + 1 < 0 \qquad 4.\ 32$$
$$2\alpha_2 - 2\alpha_1 + 1 < 0$$

The first inequality in 4. 32 contradicts the physical constraint expressed in 4. 21. Therefore case 2 is not valid either.

2. - Case 3:

In this case, the range $\xi \in (-1,1)$ falls on the right sides of the symmetric axis, the curve monotonically increases as ξ increases and $\lambda_k(\xi)$ is positive, as shown by Figure 4. 9. Therefore the inequality shown as 4. 33 would always hold.

$$\lambda_k(1) > \lambda_k(-1) > 0 \qquad 4.\ 33$$

$$\xi_1 < \xi_2 < -1$$

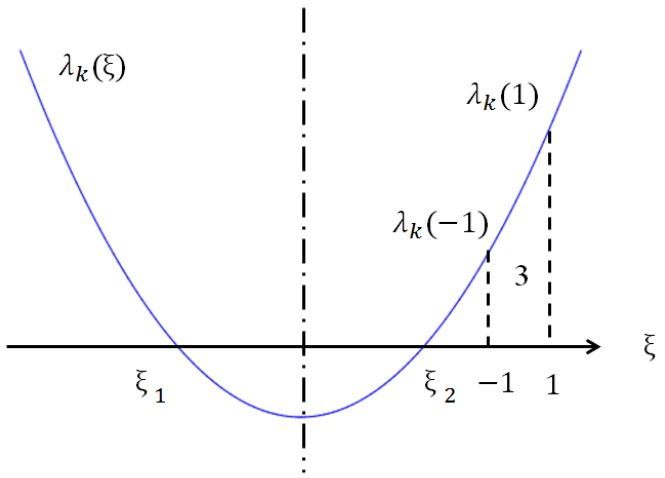

Figure 4. 9. Plot of the parabolic curve representing $\lambda_k(\xi)$, discriminant $\Delta > 0$ - Case 3

The first inequality contradicts the second Frequency Constraint (i.e., low-frequency domination), therefore region 3 is not valid.

In summary, in the second case in which the determinant $\Delta = 4\alpha_1^2 - 16\alpha_2(1-2\alpha_2) > 0$, there is no admissible region for α_1 and α_2.

3. Discriminant $\Delta = 4\alpha_1^2 - 16\alpha_2(1-2\alpha_2) = 0$

If the discriminant equal to zero, the parabola $\lambda_k(\xi)$ is tangential with respect to the horizontal axis. To eliminate the possibility that $\lambda_k(\xi)$ equals zero, the $\xi \in (-1,1)$ should be either on the left side of the symmetry axis as shown in Figure 4. 10 (a), or on the right as shown in Figure 4. 10 (b). The discussion would be identical to case 1 and case 3 with discriminant > 0 . The obtained constraints contradict with either physical constraints or the second Frequency Constraints. Therefore the possibility is not valid.

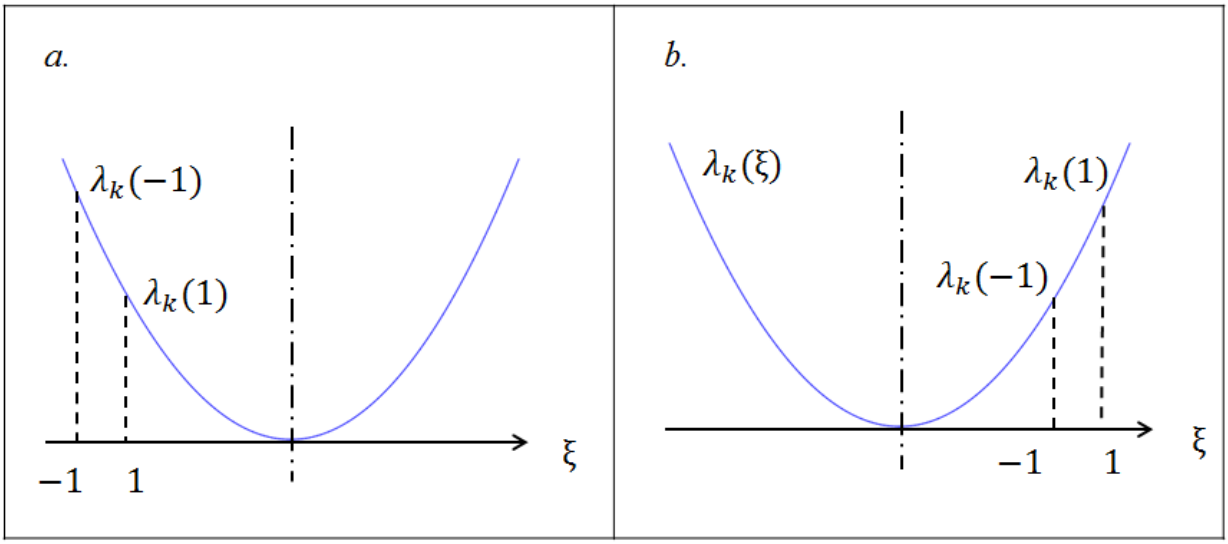

Figure 4. 10. Plot of the parabolic curve representing $\lambda_k(\xi)$, discriminant $\Delta = 0$

Summary of Constraints

All the constraints on shape coefficients α_1 and α_2 obtained under the Physical Constraints and the two Frequency Constraints are summarized as 4. 34.

$$\begin{cases} 4\alpha_1^2 - 16\alpha_2(1-2\alpha_2) < 0 \\ \alpha_1 < 0 \\ \alpha_1 + 4\alpha_2 > 0 \\ 2\alpha_2 + 2\alpha_1 + 1 > 0 \end{cases} \quad 4.\ 34$$

The resultant admissible region for α_1 and α_2 with the constraints shown as 4. 34 enforced can be plotted as Figure 4. 11, with the white area denoting the admissible region.

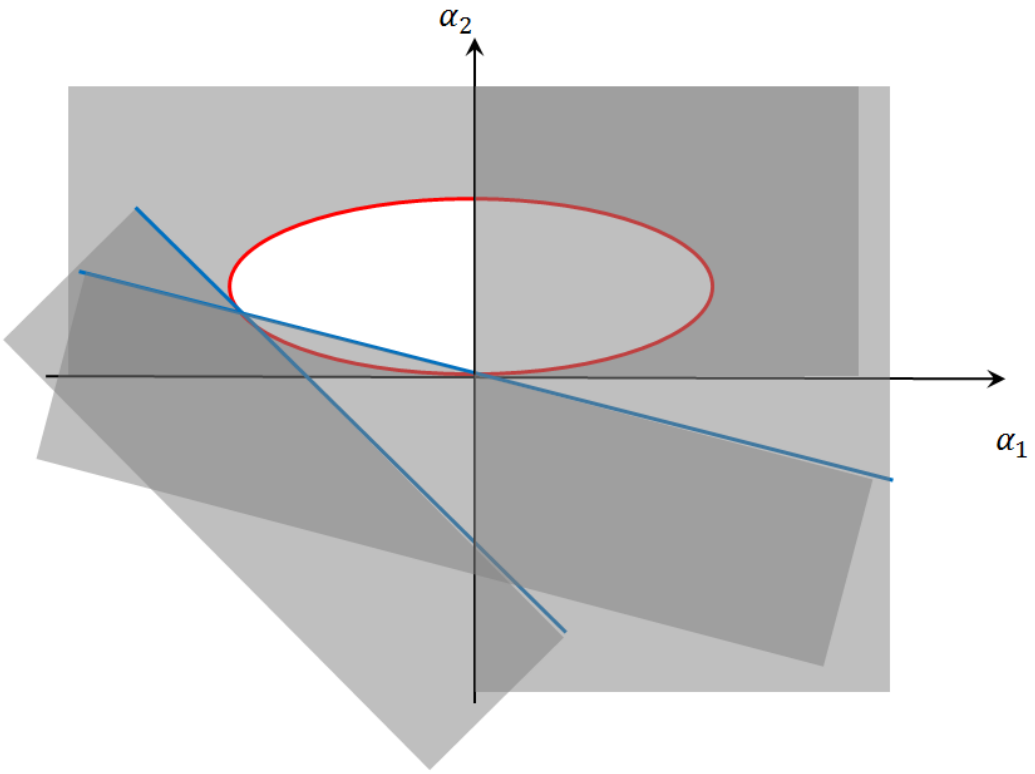

Figure 4. 11. The admissible region for α_1 and α_2

Note that the fourth constraint is not active, so that the set of active constraints that completely define the admissible region of the shape parameters can be represented as 4. 35.

$$4\alpha_1^2 - 16\alpha_2(1 - 2\alpha_2) < 0 \qquad 4.\ 35$$

$$\alpha_1 < 0$$

$$\alpha_1 + 4\alpha_2 > 0$$

Figure 4. 12 shows the spindle force intensity with respect to the parameter values α_1 and α_2, with the constraints shown by 4. 35, i.e. the admissible region shown by Figure 4. 11. The overall stiffness factor is set to be constant. It can be shown that the force intensity is relatively low on the edge of the admissible region. As the parameter value pairs get closer to the upper right corner, i.e. α_1 approaches to zero and α_2 approaches to the maximum in the region, the force intensity increases. As α_2 increases, the lumped parameter A related to the bending property increases according to equation 4. 11; as α_1 approaches to zero, the lumped parameter B related to the shearing property increases. Therefore the force generated by the tire radial displacement increases, as well as the resultant spindle force. If α_1 and α_2 reaches the upper right corner, the force intensity is too high to plot in Figure 4. 12. Therefore the region very close to the vertical axis is trimmed out in the figure.

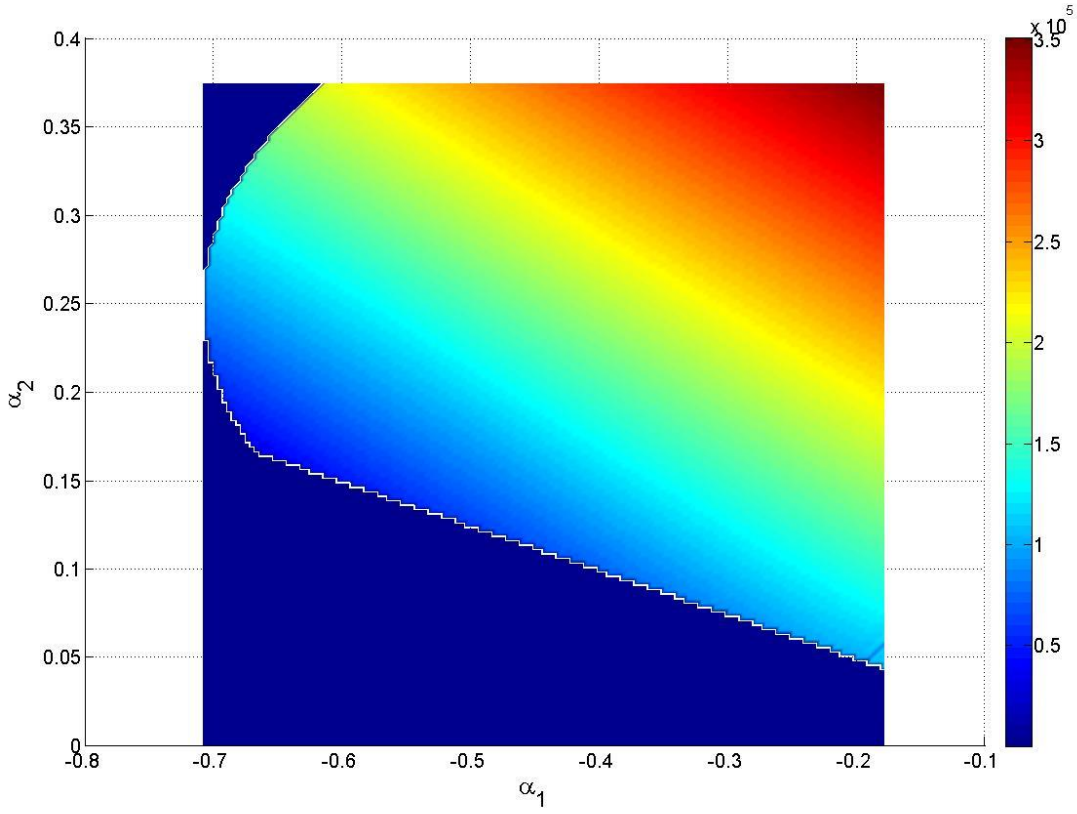

Figure 4. 12. Spindle force intensity with respect to the shape parameters

4.2.2 Overall stiffness factor

Given shape parameters α_1 and α_2 identified by the previous procedures, the stiffness parameters $k_0$required for the stiffness matrix can be computed by an iterative optimization process with respect to the force-deflection curve obtained from a flat plate test. The experimental data used throughout this work is provided by Professor Schalk Els of the University of Pretoria, South Africa. The tire used is Continental Conti-Trac AT 238/85 R16. During the Parameter Identification Process, a flat plate is pushed towards the center of the tire gradually (i.e., under quasi-static conditions) and the resultant spindle force *F* is measured with respect to the tire-plate interference *e*. An optimization process with respect to the difference between the simulated and the experimental forces is employed to identify the

stiffness parameters k_0 for the specific tire. With the stiffness parameter k_0 and the shape parameters α_1 and α_2 identified, given the flat plate as terrain excitation, the spindle force with respect to deflection can be calculated by the equation of motion. The comparison between the simulated result and the experimental data shows very good agreement as indicated in Figure 4. 13. The difference between the simulated and experimental force is less than 4%.

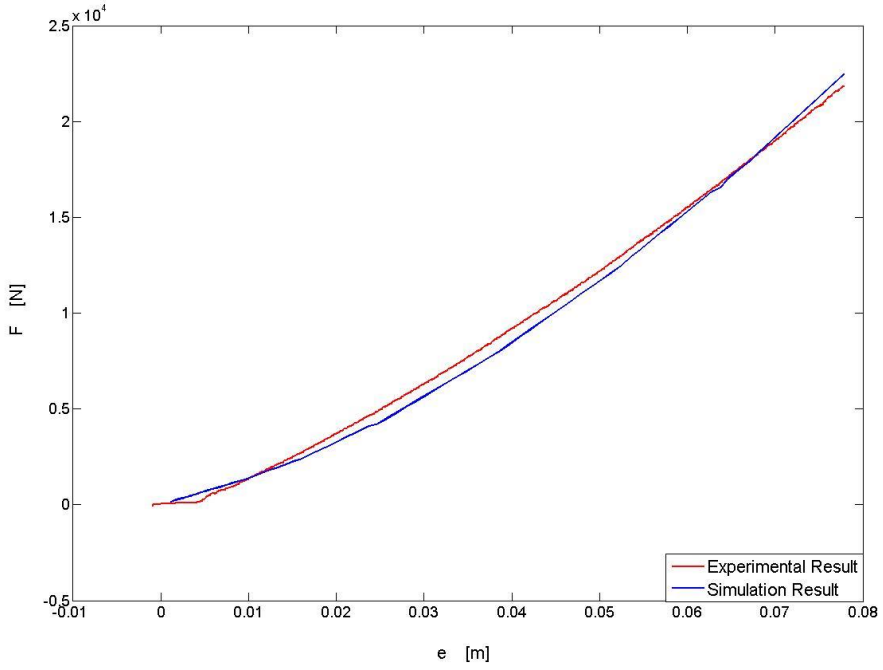

Figure 4. 13. Comparison between the flat-plate experimental and simulated force, *F*, with respect to the interference, *e*

4.2.3 Tire Property Parameter and Parameter Adaption Process

According to the previous system identification process with the cleat test to determine the shape parameters, it can be seen that the model parameter is dependent on the number of tire segments *N*, as the cleat length should be $\frac{2\pi R}{N}$ and the resultant tire radial deformation vector length is N. *N* must be large enough to meet the small angle assumption required in the model derivation. If a different number of

segments is desired for accuracy adjustment, the model parameters needs to be recalibrated. In order to develop an easy parameter adaption process between different numbers of segments, the relationship of model parameters with respect to *N* is further analyzed. Based on the lumped parameters definition as shown by Table 4. 1, *A, B* and *C* can be considered as functions of *N*, with γ_1, γ_2 and γ_3 as property parameters as 4. 36. It is evident that γ_1, γ_2 and $\gamma_3$are positive and invariant with respect to a specific tire, therefore *A, B* and *C* are positive too.

$$A = \gamma_1 N^3 \qquad \gamma_1 = \frac{EI}{(2\pi R)^3} \tag{4. 36}$$

$$B = \gamma_2 N \qquad \gamma_2 = \frac{Gbh}{2\pi R}$$

$$C = \frac{\gamma_3}{N} \qquad \gamma_3 = 2\kappa\pi R$$

According to the constraints on the model parameters α_1, α_2 given in 4. 35, the corresponding constraints for property parameters γ_1, γ_2 and γ_3 and segment number *N* can be shown as 4. 37. The overall stiffness k_0 should be positive due to simple physical characteristics of tires.

$$\gamma_2^2 - 4\gamma_1\gamma_3 < 0 \tag{4. 37}$$

$$k_0 > 0$$

$$\gamma_2 N - 4\gamma_1 N^3 < 0$$

The formulation of $k_0 > 0$ due to physical constraint can be rearranged as 4. 38.

$$k_0 = 6B - 4A + 2C = \frac{1}{N}\left[4\gamma_1\left(N^2 - \frac{\gamma_2}{4\gamma_1}\right)^2 + \frac{4\gamma_1\gamma_3 - \gamma_2^2}{4\gamma_1} + 2\gamma_1 N^4\right] > 0 \tag{4. 38}$$

Therefore $k_0 > 0$ always holds and it is consistent with the tire physical requirement.

The third constraint is shown in 4. 37 can be rewritten as 4. 39. It can be considered as the minimum requirement for the number of segments for the constraint mode tire model.

$$N > \sqrt{\frac{\gamma_2}{\gamma_1}} = 2\pi R\sqrt{\frac{Gbh}{EI}} \qquad 4.\ 39$$

According to equations 4. 11 and equation 4. 36, given k_0, α_1 and α_2 obtained from the previous parameter identification process with a specific *N*, the three property parameters can be obtained by a transfer matrix T_N as equation 4. 40. The property parameters are invariant for a specific tire regardless of the number of segments N.

$$\begin{bmatrix}\gamma_1\\ \gamma_2\\ \gamma_3\end{bmatrix} = T_N \begin{bmatrix}k_0\\ k_0\alpha_1\\ k_0\alpha_2\end{bmatrix} \qquad 4.\ 40$$

$$T_N = \begin{bmatrix}0 & 0 & \frac{1}{N^3}\\ 0 & \frac{1}{N} & \frac{4}{N}\\ N & 4N & 10N\end{bmatrix}$$

With the property parameters calculated, the constraint mode tire model parameters k_0, α_1 and α_2 can be computed as 4. 41, given any N' that meets the constraint as 4. 39. The larger number of segments leads to finer tire separation, and provides more accurate deflection and force prediction; however it is also more computationally expensive. Therefore given a set of model parameters k_0, α_1 and α_2 calibrated with *N* segments, through the transfer matrix T_N and the property parameters, the model parameters can be easily adapted with different segment numbers for different application requirements.

$$k_0 \begin{bmatrix} 1 \\ \alpha_1 \\ \alpha_2 \end{bmatrix} = T_{N'}^{-1} \begin{bmatrix} \gamma_1 \\ \gamma_2 \\ \gamma_3 \end{bmatrix} \qquad 4.41$$

$$T_{N'}^{-1} = \begin{bmatrix} 6N'^3 & -2N' & \frac{1}{N'} \\ -4N'^3 & N' & 0 \\ N'^3 & 0 & 0 \end{bmatrix}$$

4.3 Model Validation

To examine the circumferential deformation property, especially the bridging and enveloping property, the tire model is run over small cracks and bumps. The resultant shapes are shown in Figure 4. 14. The black and the red lines represent the original and deformed tire shape respectively, while the blue lines represent the discretized terrain profile. The tire bridging and enveloping properties are evident.

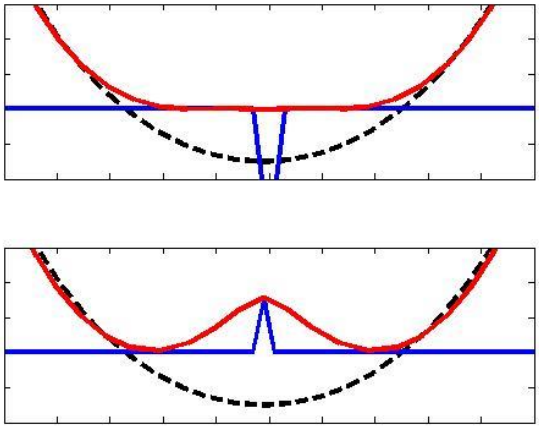

Figure 4. 14. Bridging and enveloping properties of constraint mode tire model

A cleat test is conducted to validate the force prediction of the constraint mode tire model. A flat plate with a square tube as cleat at the center is pushed gradually towards of the tire and the resultant spindle force *F* is measured with respect to the tire-plate interference *e*. The side length of the square tube is 19 mm.

The comparison between the simulation and measured data shows reasonable agreement in the linear region, i.e. the small interference region (up to 0.05m), as shown in Figure 4. 15. The difference between the experimental and simulated force data are less than 7%. It can be seen that the force versus deflection curve has a discontinuity in slope at 5cm. The reason is that in the first segment with smaller slope, the tire is suspended by the cleat event and the contact area related to force generation is constrained to the cleat surface only, as shown in the upper picture in Figure 4. 15. Therefore the force change rate with respect to deflection is relatively small. In the second segment with a larger slope, the tire tread touches the ground outside of the cleat and the contact area increases, as shown in the lower picture. Therefore the rate at which the generated force changes with respect to the deflection increases. If the side length of the square tube increases to 25 mm, the difference between the experimental and simulated force data increases to 13%.

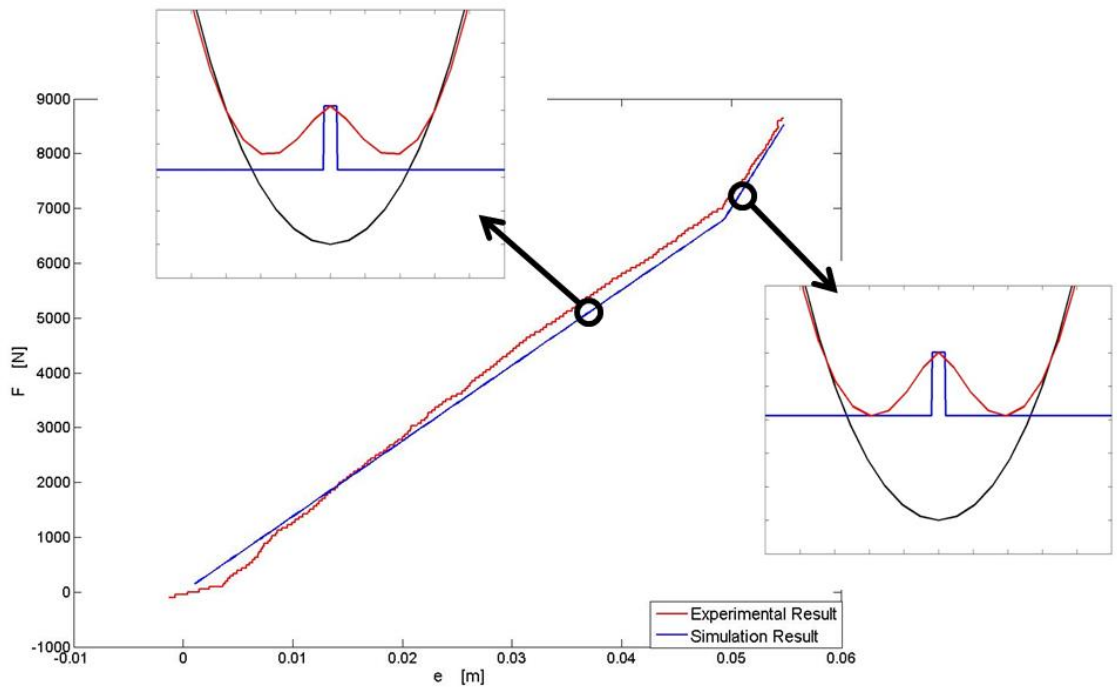

Figure 4. 15. Comparison between the cleat experimental and simulated force, F, with respect to the interference, e

4.4 Discussion

The constraint mode tire model developed in this work can serve as a terrain morphological pre-filter. The wheel trajectory can be computed given a section of actual terrain profile over which the wheel travels and a constant spindle load. The vertical trajectory wheel center is smoothed compared with the original terrain profile due to the tire bridging and enveloping properties. It can serves as an equivalent input to a simpler tire model to provide fast yet reliable spindle force prediction for vehicle dynamic simulation and reliability evaluation. Besides, the tire constraint model will be further improved so that it can be applied on not only deterministic terrain profiles, but also to stochastic terrain profiles. Future work focuses on further simplification of the system identification to determine the model parameters by only using the experimental data from a flat plate test.

4.5 Conclusions

The main contributions of this work are the enhancement to the constraint mode tire model to capture the tire circumferential displacements and predict the spindle force according to the tire shape. The model expression is derived by discretizing tire into segments and applying Hamilton's principle. The required model parameters can be reduced to two non-dimensional shape parameters and an overall stiffness factor. A parameter identification process to calibrate the tire model towards a specific tire is provided. The tire circumferential deformability is examined through the bridging and enveloping properties. The prediction accuracy of spindle force is evaluated by comparing the simulation and experimental response for a cleat test. This work provides a simple, accurate planar tire model for terrain-tire interaction analysis and vertical spindle force prediction.

5. Terrain Pre-filtering Technique

The vertical force generated from terrain-tire interaction has long been of interest for vehicle dynamic simulations and chassis development. As a vehicle traverses a particular terrain section, all of its content is an excitation to the suspension system through the pneumatic tire. The bridging and enveloping properties of the tire then filter the road excitations to the chassis. Due to the high complexity of the tire structure and the immense size of a high fidelity terrain profile, it is not efficient to calculate the terrain-tire interaction at every location. A more computationally efficient method would be to develop a pre-filtering method for the terrain. The method will produce an equivalent terrain profile specifically developed for use with efficient tire models (e.g. point follower tire model) in vehicle simulations. The desired produced responses would be nearly identical to the ones using a complex tire model and unfiltered terrain.

In this work, a terrain pre-filtering technique based on the constraint mode tire model is developed to improve simulation efficiency while still providing reliable load predictions. Under quasi-static condition, the wheel is assumed to convey one quarter of the vehicle static load. At each location along the tire's path, the wheel center height is adjusted until the static spindle load reaches this pre-designated load. The vertical location of the spindle (that yields the correct static quarter-car spindle load) obtained statically can be used as an equivalent terrain elevation. This series of equivalent terrain elevations form an equivalent terrain profile and can be used as the excitation to a simplified tire model (e.g. point follower tire model) during dynamic simulations. The spindle force can be predicted by using the pre-filtered terrain profile, coupled with a simple point follower tire model. This proposed method is compared to two references: one reference for accuracy and one reference for computational efficiency. The same vehicle model is coupled with the constraint mode tire model to generate reference forces and is used for an accuracy comparison. The same vehicle model with point-follower tire models is as a reference for computational efficiency. In the example simulations, the proposed terrain pre-filtering

technique demonstrates that the computational efficiency can be improved by three orders of magnitude without a statistically significant loss of accuracy in load prediction. The new pre-filtering technique can be applied to probabilistic terrain by incorporating realizations of terrain profiles provided by the stochastic gridding method developed in Chapter 3. When probabilistic terrain is combined with the stochastic gridding method, the uncertainty of the terrain measuring equipment is reflected by the variation of different resultant force signals.

5.1 Terrain Pre-filtering Technique Development

A pre-filtering technique based on the constraint-mode tire model requires a properly calibrated model. This calibration may be the result of either tuning the model for a specific tire, or a more general approach in which some standard values are used. For example, the latter case is preferred when developing a roughness metric that would be applicable to a large class of vehicles and tires. Once a proper constraint-mode tire model is defined it can be applied to the pre-filtering problem.

The pre-filtering method developed in this work is shown schematically in Figure 5. 1. The left side of the figure shows the development of the effective terrain profile using a static spindle load; one quarter of the total vehicle static weight is used in this work. At each horizontal location, under quasi-static assumption, the tire center height is adjusted to match this static spindle load. The statically obtained tire center trajectory is the pre-filtered terrain profile, as shown on the right side of Figure 5. 1. Next a simple tire model (e.g., a point-follower) and a dynamic vehicle model are used to simulate the vehicle excitation and resultant vehicle load.

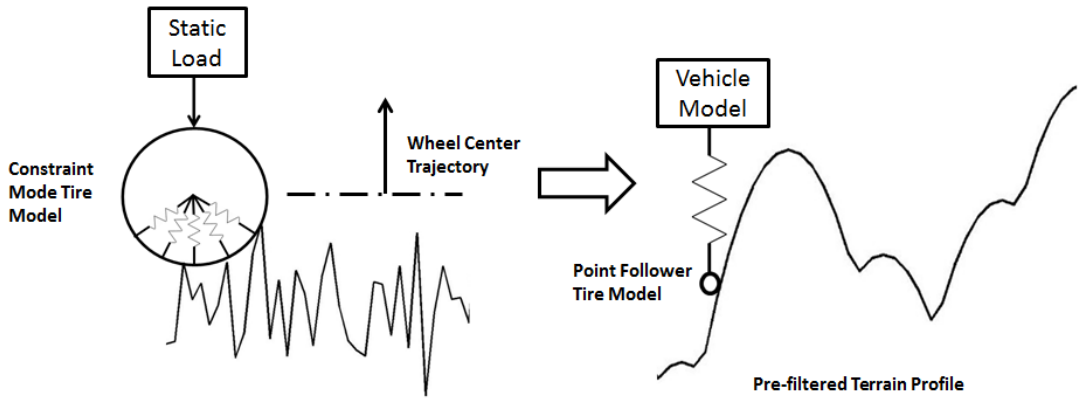

Figure 5. 1. Terrain Pre-filtering Technique

A vehicle dynamic simulation process is built in Simulink to emulate the response to terrain excitations. The system is shown schematically in Figure 5. 2. It is solely excited by the measured terrain profiles. The specific tire model and vehicle model modules can be adjusted or substituted according to application requirements. The results of the simulation over a given terrain include the sprung mass motion and suspension forces. A 7-DOF vehicle model is used in this work; the equations of motion are shown in Appendix Section 2.

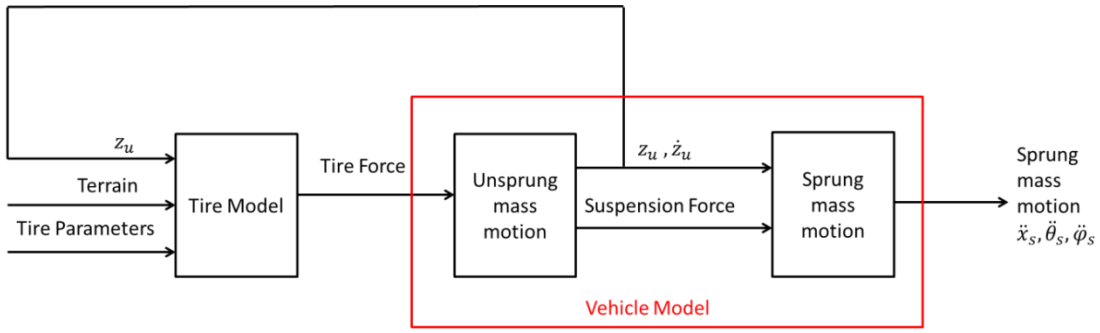

Figure 5. 2. Vehicle Dynamic Simulation Flowchart

As the terrain interacts with the vehicle through the tire, a tire model with high computational efficiency that produces accurate force prediction is desired. The point-follower tire model is a simple tire model in

which a spring interacts with the terrain profile point-by-point and the spindle force is computed through Hooke's Law. This commonly used point-follower model is computationally efficient, but it fails to capture even the most basic tire properties (e.g., the tire bridging and enveloping). The simulation results tend to yield spindle loads with a broader variation than a physical tire.

5.2 Model Verification

The goal of this work is to develop an accurate, computationally efficient estimate of the spindle loads. In order to achieve this goal, an equivalent terrain profile is developed to be used as the excitation to the point-follower tire model. The vehicle model used for the case studies in this work is a 7-DOF model as Figure 2. 15, with the equation of motions shown in the Appendix Section 2. In future work a more complex vehicle model could be used, but here the goal is to compare the relative improvements in computational speed, so a simple vehicle model is used in all the simulation cases.

The computational accuracy of the proposed modeling technique will be compared to a reference model traveling over the original terrain. The differences between the reference model and the proposed method are in the tire model used (constraint-mode or point-follower) and whether the terrain is the original terrain or it is pre-filtered. In this reference model, the tire is the constraint-mode tire model and the unfiltered terrain is used. In this way, the current state of practice (unfiltered terrain, complex tire model) is the reference and provides the measure of the upper limit for accuracy. This modeling technique is referred to as, "Reference-Best".

The proposed modeling technique uses pre-filtered terrain with a simple point-follower tire model. The pre-filtering is completed *a priori* using a static load of one-quarter the vehicle static weight and the constraint-mode tire model. This pre-filtering takes place off-line and takes place only once, before any vehicle simulations are run. This modeling technique is referred to as, "Proposed Method".

A third modeling technique is presented to serve as a reference for the computational speed with which a simple tire model can generate results. Specifically, unfiltered terrain excites a point-follower tire model. This modeling technique is referred to as, "Reference-Fastest". Table 5. 1 summarizes the three combinations of tire model and terrain excitation used in this work.

Table 5. 1. Tire Model and Terrain Excitation Combinations Used in Vehicle Dynamic Simulation

Modeling Technique	**Tire Model**	**Terrain Excitation**
Reference – Best	Constraint-Mode	Unfiltered Terrain
Proposed Method	Point-Follower	Pre-filtered Terrain
Reference - Fastest	Point-Follower	Unfiltered Terrain

Two deterministic terrain profiles are used to demonstrate the impact on computational speed and accuracy of using the proposed modeling method: one rough and one smooth terrain. The vertical forces at the spindle are simulated using the modeling techniques defined by the three terrain/tire combinations shown in Table 5. 1. The force generated by the Reference–Best method is used as a reference to evaluate the accuracy of the other two methods. Different realizations obtained from a stochastic gridding method are used as the input to the pre-filtering technique to validate the technique on probabilistic terrain. The difference in computational effort and a comparison of accuracy are then calculated.

5.3 Case Study: Smooth Terrain

Smooth terrain with occasional narrow deep cracks is used for the first case study. The 7-DOF vehicle model is simulated over the unfiltered terrain using a constraint-mode tire model and a point-follower tire model to form the Reference-Best and Reference-Fastest modeling results, respectively. Next, the

proposed modeling technique is employed. The terrain is filtered (using a quarter-car static weight and a constraint-mode tire) as shown in Figure 5.3. The original unfiltered terrain is shown as a solid blue line and exhibits numerous narrow deep cracks. The filtered terrain is shown as a solid red line and it is clear that these cracks are filtered out. The smoothing of the filtered terrain profile is due to the ability of the constraint-mode tire model to exhibit the tire bridging and enveloping properties when traversing such localized events. Next the pre-filtered terrain is used to excite the point-follower tire model with the 7-DOF vehicle model.

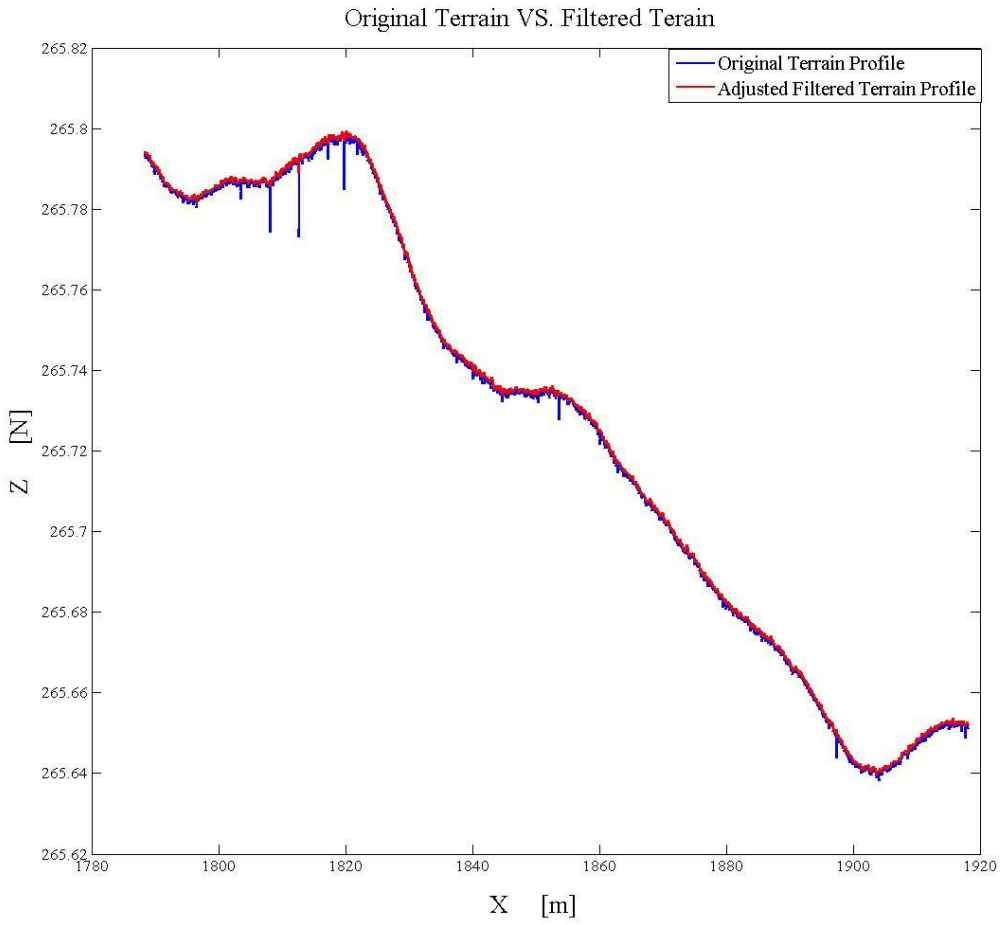

Figure 5.3. The comparison of a smooth original terrain profile (blue) with the adjusted pre-filtered terrain (red)

The predicted forces from the three modeling techniques excited by this smooth terrain surface are shown in Figure 5. 4. The spikes in vertical force result from the Reference-Fastest model (Point-Follower – Unfiltered Terrain) and are shown as a green line. These force spikes are mainly caused by the narrow cracks of the original terrain profile and the lack of a bridging property of the point-follower tire model. The black horizontal lines denote the range of the Reference-Best force signal. The Reference-Fastest model results in 30 excursions outside the range, while the Proposed Method (Point Follower with Pre-filtered Terrain) only has 1 excursion outside the range. It is clear that the loads predicted by the Reference-Fastest model (green line) have significantly greater variation than those of the Reference-Best method (red line) or the Proposed Method (blue line).

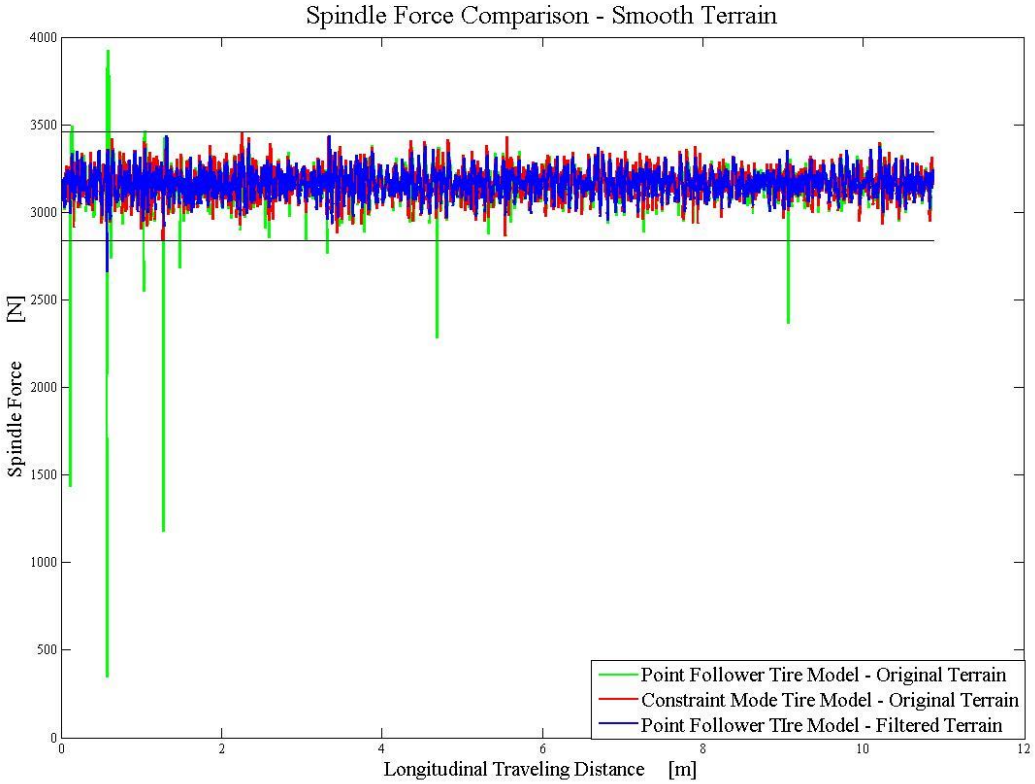

Figure 5. 4. The front spindle force comparison of simulation results from the three combinations

The variation of the spindle force has significant impact on fatigue prediction. To quantitatively compare this impact, the rainflow counting method is used to extract load cycles from the force signals. For each individual load cycle, indexed by i, amplitude of the load (F_{ai}) and the mean of the load is calculated. N_i is defined as the number of cycles required to cause failure given repeated loading of the i^{th} load cycle. According to fatigue theory, the number of cycle to cause failure (N_i) decreases exponentially with the load amplitude (F_{ai}) [47]. Therefore the load amplitude F_{ai} with relatively large value contributes much more to the fatigue effect, while the one with small value has less impact. As a practical matter, most materials have a threshold below which loads do not affect the fatigue. This work is using the pseudo-fatigue concept to describe contributions to damage in a general sense, no as it applies to a particular material. Therefore, in the work if the force amplitude is less than ten percent of the static load on the spindle, its impact on fatigue is considered negligible. Figure 5.5 shows the rainflow matrix of the load obtained by Reference – Best shown in Table 5. 1. The constraint mode tire model and unfiltered terrain is used to generate a reference force signal. It can be seen that the maximum load amplitudes are about 300N, with relative low numbers of cycles. The load amplitudes with highest numbers of cycles have low values, and the corresponding mean load values are close to the static load on the spindle.

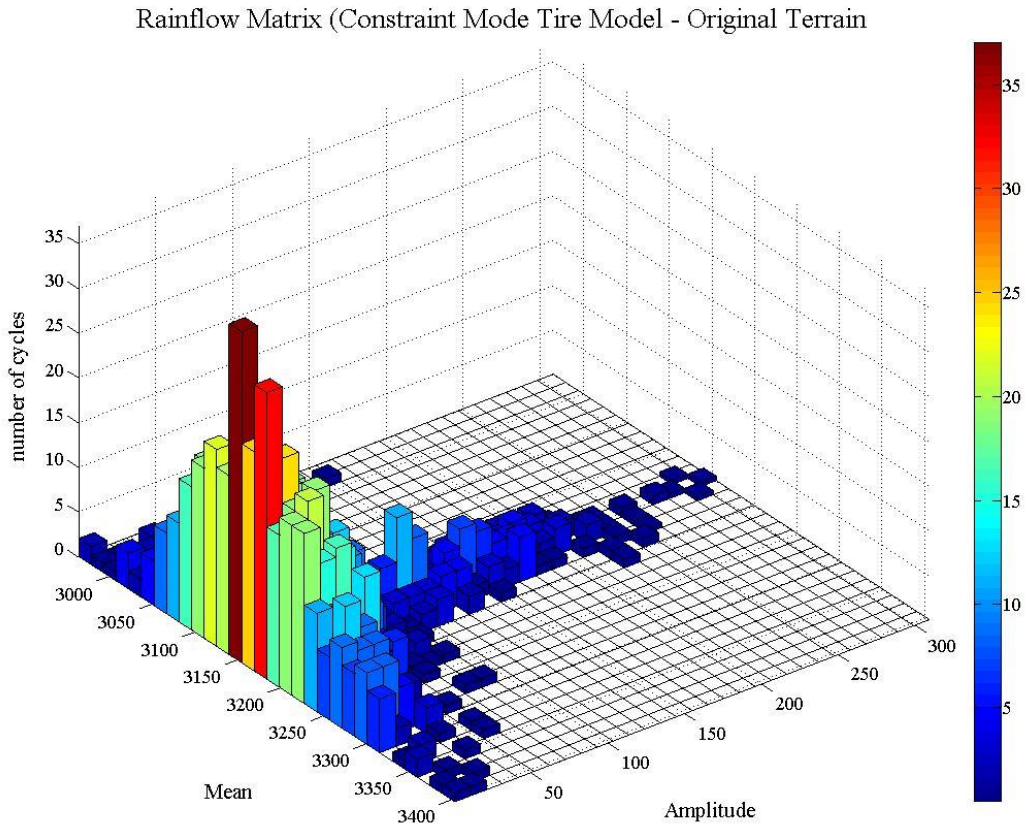

Figure 5.5. Rainflow Matrix: Reference – Best on Smooth Terrain

The rainflow matrix of the load obtained by Reference - Fastest method as described in Table 5. 1 is shown as Figure 5.7. Compared to the rainflow matrix of the reference load shown in Figure 5.5, the maximum load amplitudes increase about 10 times due to the spikes shown in Figure 5. 4. These large amplitudes are due to the deep cracks on the unfiltered terrain profile shown in Figure 5.3. The simple point-follower tire model fails to bridge these cracks.

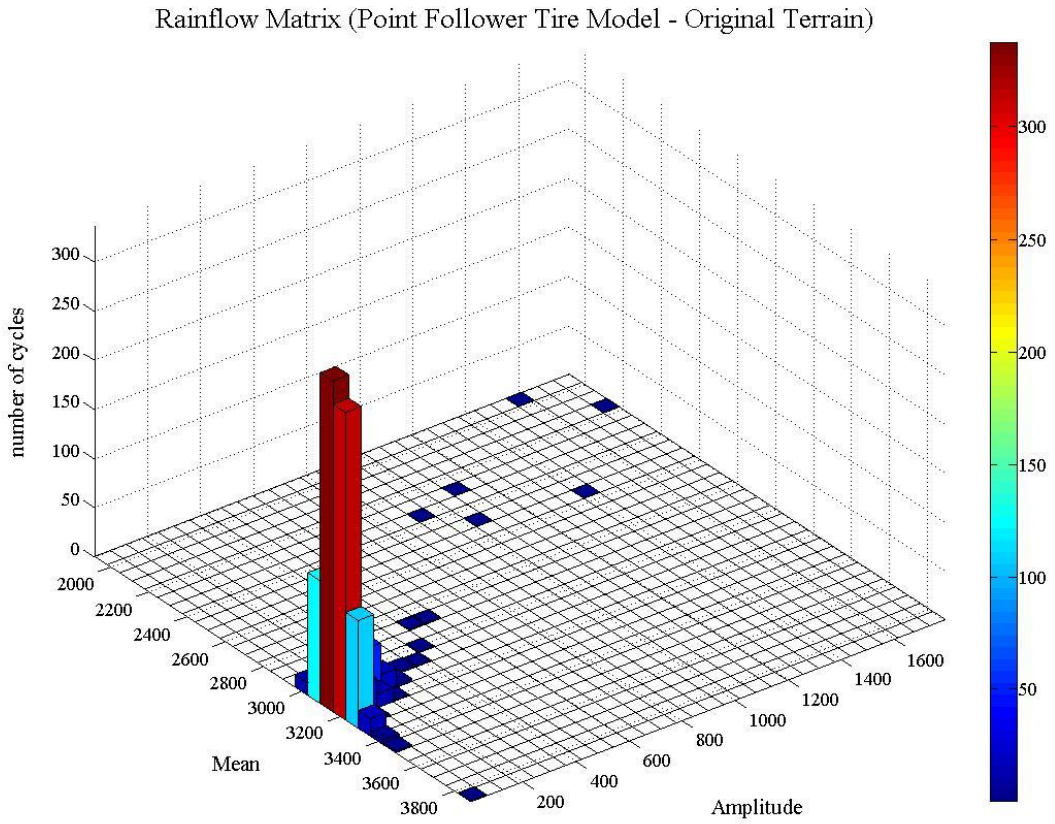

Figure 5.6. Rainflow Matrix: Reference - Fastest Method on Smooth Terrain

The rainflow matrix of the force obtained by the Proposed Method (as described in Table 5. 1) is shown as Figure 5.7. Compared with the one obtained by Reference - Fastest Method as Figure 5.6, the loads with extreme amplitudes are eliminated due to the bridging and enveloping properties of the constraint mode tire model. The results are similar to those predicted by the Reference-Best model shown in Figure 5.5.

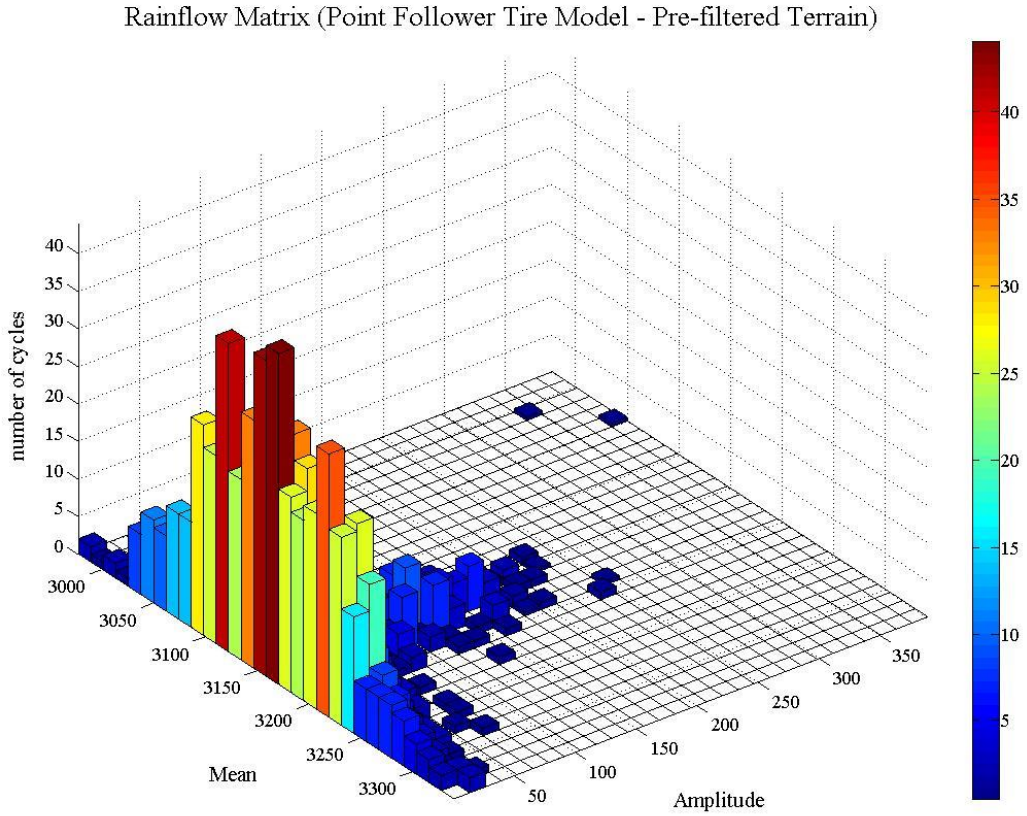

Figure 5.7. Rainflow Matrix: Proposed Method on Smooth Terrain

To quantitatively compare the impacts of the three obtained loads to the spindle, a Pseudo Fatigue life is introduced as a measure [47]. With the force amplitudes of the i[th] load cycle F_{ai} obtained from the rainflow counting method, the corresponding number of cycle to cause failure (N_i) can be obtained from a Wohler curve modeled with S_{ut} and S_y, the ultimate tensile stress and yielding stress respectively, as shown by equations 5. 1. In this work, it is assumed that the yield stress is 60% of the ultimate tensile stress (for example the yield stress and ultimate tensile could be 520 Mpa and 860 Mpa).

$$N_i = \left(\frac{\sigma_{ai}}{a}\right)^{\frac{1}{b}} \qquad 5.\ 1$$

$$r = \frac{S_y}{S_{ut}} \approx 60\% \quad b = \frac{log\frac{0.9S_{ut}}{0.5S_y}}{log\frac{10^3}{10^6}} = -0.159 \quad -\frac{1}{b} \approx 6.3$$

According to Miner's rule, the fatigue damage caused by i[th] load cycle can be quantified as $\frac{1}{N_i}$. Therefore the accumulated damage of multiple extracted cycles can be calculated by the summation of $\frac{1}{N_i}$ of different load cycles. The ratio of the accumulated damage is introduced to give a quantitative measure of the difference in accumulated fatigue damage as shown equation 5. 2. The reference for this accuracy comparison is the Reference-Best model. In this way, if the ratio is close to 100%, then the amount of damage predicted using the Proposed Method or the Reference-Fastest method is close to that predicted by the Reference-Best method.

$$\frac{Damage_j}{Damage_{Reference-Best}} = \frac{\left(\sum \frac{1}{N_i}\right)_j}{\left(\sum \frac{1}{N_i}\right)_{Ref-Best}} = \frac{(\sum \sigma_{ai})_j^{-\frac{1}{b}}}{(\sum \sigma_{ai})_{Ref-Best}^{-\frac{1}{b}}} = \frac{(\sum F_{ai})_j^{-\frac{1}{b}}}{(\sum F_{ai})_{Ref-Best}^{-\frac{1}{b}}} \qquad 5.\ 2$$

$$j = Fastest \;\; Proposed$$

The ratio for Proposed Method (Point Follower with Pre-filtered Terrain) and for the Reference-Fastest (Point Follower with Unfiltered Terrain) are compared to the Reference-Best results and shown in Table 5. 2. It can be seen that the ratio obtained from Reference-Fastest is much larger than 100% due to the existence of the large spikes in the force signal, i.e. the tire-terrain combination fails to provide a reliable spindle force signal for fatigue. While the ratio obtained Proposed Method is very close to 100%. To provide a more intuitive comparison, the accumulated damage fatigue ratio is converted to an equivalent force amplitude ratio. The equivalent force amplitude ratio can be considered an equivalent accuracy in the ability of the method to measure the same force as the Reference-Best model. Consider the case of the Reference-Fastest method which has equivalent force amplitude of 140% of the Reference-Best

results. This could be thought of as consistently measuring the force with 40% error with respect to the Reference-Best (e.g., measuring the force with a sensor that has a 40% gain error). In contrast, the Proposed Method has an equivalent force ratio of 99%, which would be the same result if the Proposed Method had simply recorded 99% of the Reference-Best forces at all times. In this case study it is clear that the accuracy of the Proposed Method is nearly identical to the Reference-Best method and the Reference-Fastest Method is simply unacceptable.

Table 5. 2. Accumulated Fatigue Damage Ratio for Smooth Terrain

	Reference-Fastest	Proposed Method
Accumulated Fatigue Damage Ratio VS. Reference-Best	6900%	95%
Equivalent Force Amplitude Ratio VS. Reference-Best	196%	99%

5.4 Case Study: Rough Terrain

A rough terrain profile is used as a second case study. Figure 5.8 shows the comparison of the terrain section before (blue line) and after (red line) filtering. In contrast to the case with the smooth terrain, the difference between the original and filtered terrain is considerable.

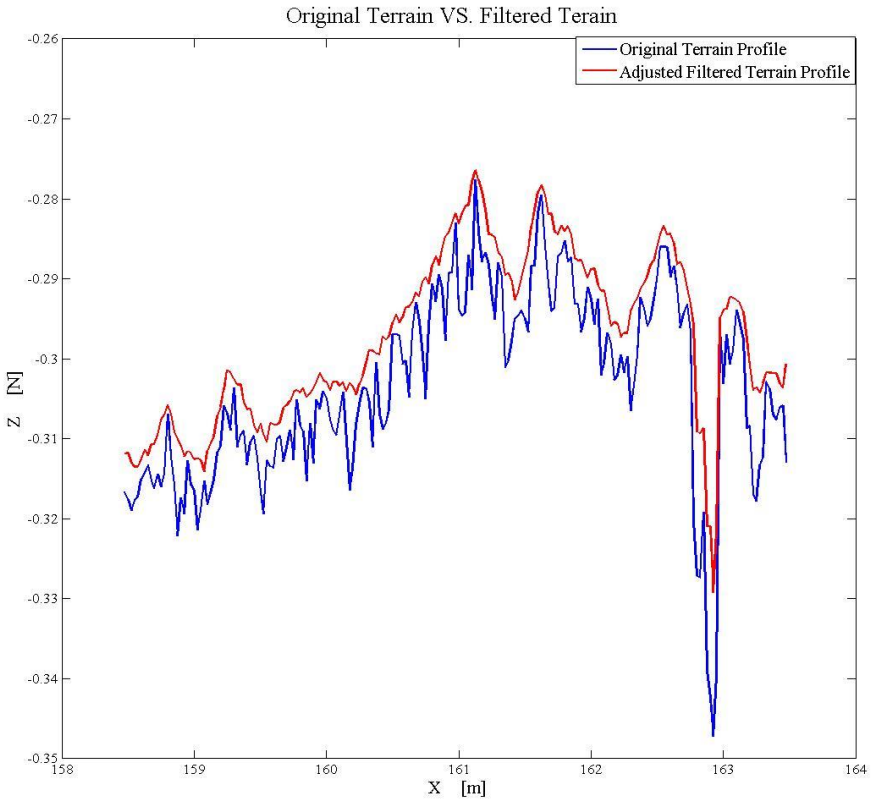

Figure 5.8. The comparison of a rough original terrain profile (blue) with the pre-filtered terrain (red)

The forces simulated using the three modeling techniques with this rough terrain input is shown in Figure 5. 9. The green line represents the Reference-Fastest method which has far greater peak forces than the results from the Reference-Best method (red line) or the Proposed Method (blue line). Although the range of the Reference-Best loads is not plotted as black horizontal lines, the force excursions outside the range of the Reference-Best loads are computed: the Reference-Fastest results in 7 excursions outside the range, while the Proposed Method model has no excursion outside the range.

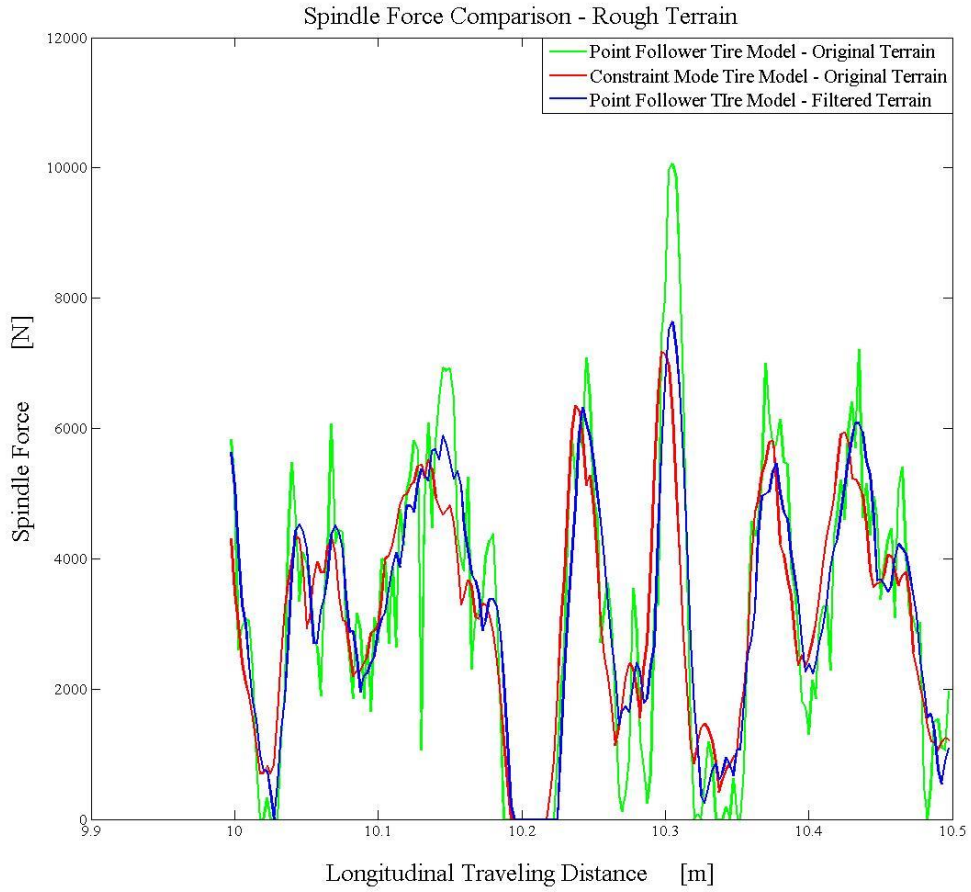

Figure 5. 9. The front spindle force simulation results from the three combinations

The rainflow matrix load obtained by simulating Reference–Best (described in Table 5. 1) is shown as Figure 5. 10. The results are similar to those found in the previous case study with smooth terrain, the load cycles with highest numbers are around the static load on the spindle. The high load amplitudes possess relative low numbers of cycles; however compared to the previous smooth terrain case, the amplitude is much larger. Therefore the corresponding impacts on the fatigue of the spindle are considerably larger.

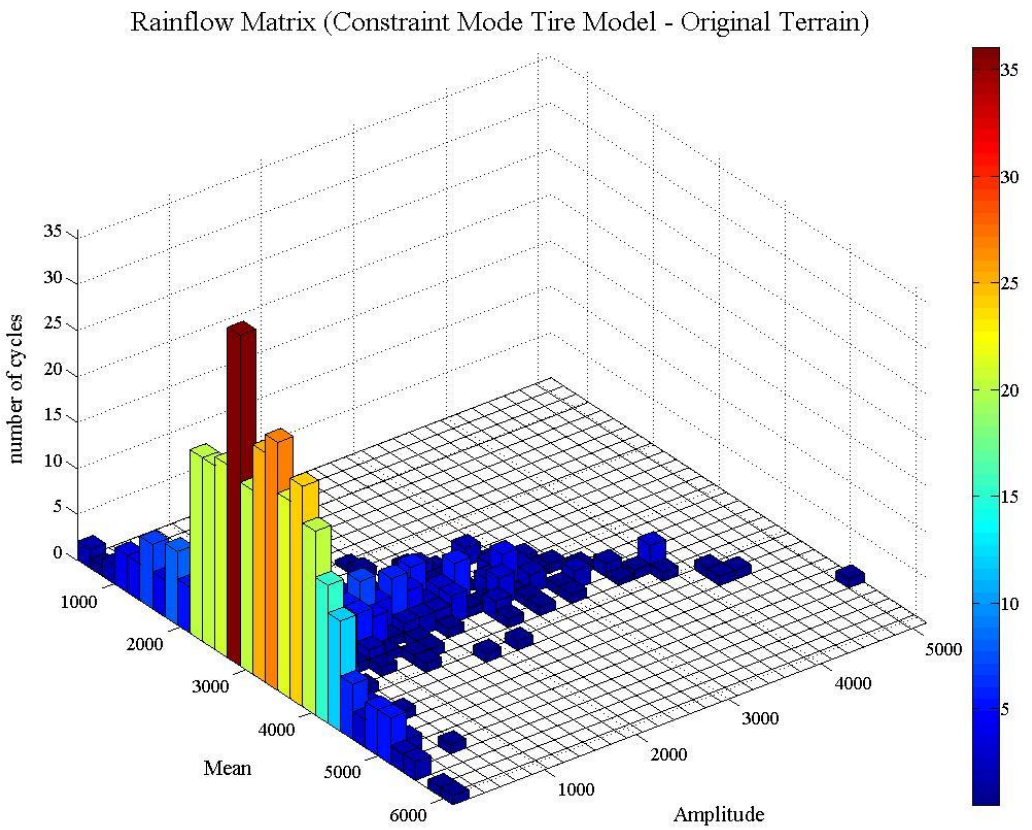

Figure 5. 10. Rainflow Matrix: Reference – Best on Rough Terrain

Figure 5. 11 shows the rainflow matrix of the load obtained by Reference-Fastest method (described in Table 5. 1). Compared to the rainflow matrix of the reference load shown in Figure 5. 10, the numbers of cycles with relative high load amplitudes (> 1000 N) increases significantly.

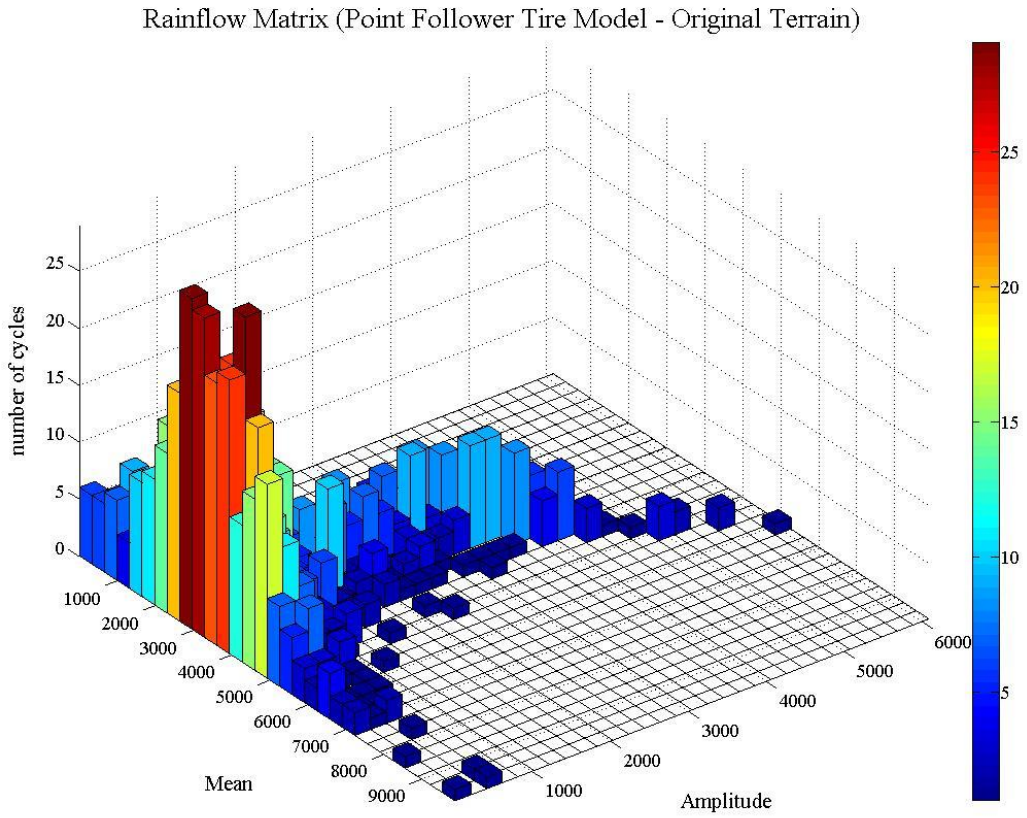

Figure 5. 11. Rainflow Matrix: Reference - Fastest Method on Rough Terrain

The rainflow matrix of the force obtained by Proposed Method (described in Table 5. 1) is shown as Figure 5. 12. Compared with the results obtained by the Reference-Fastest Method shown as Figure 5. 11, the numbers of cycles with high amplitudes are reduced noticeably due to the smoothening effect of the pre-filtering technique resulting from tire bridging and enveloping properties. Again, the results from the Proposed Method are much more closely aligned with those derived from the Reference-Best method.

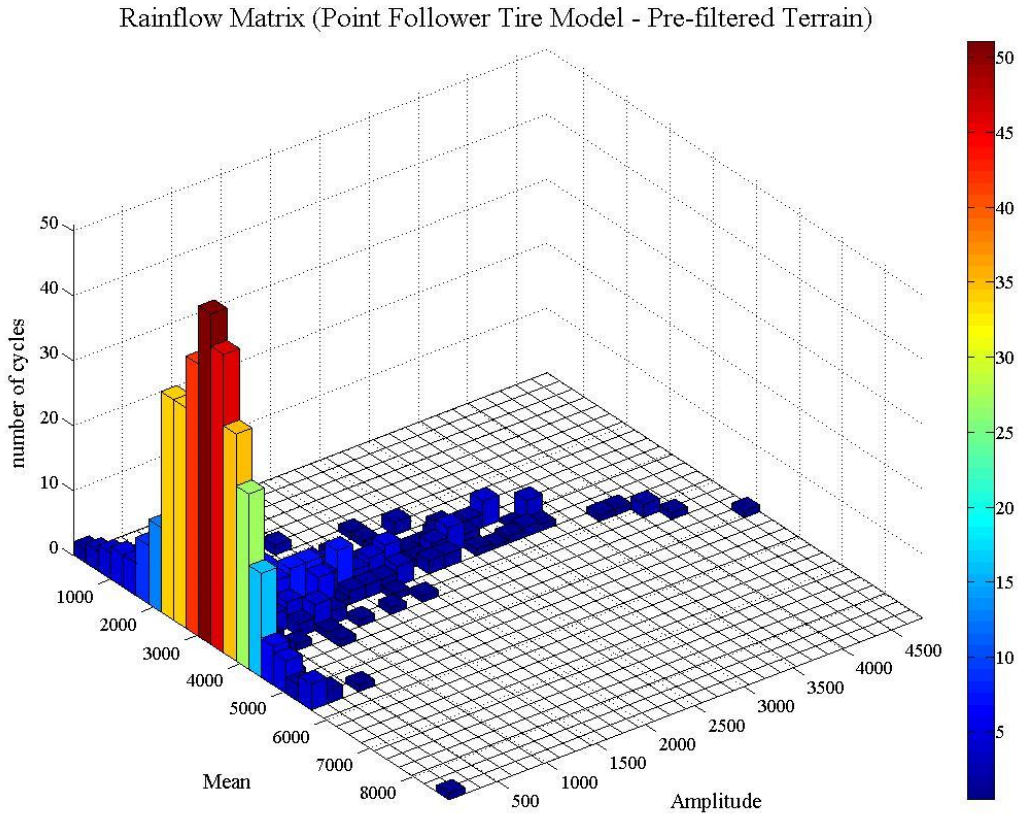

Figure 5. 12. Rainflow Matrix: Proposed Method on Rough Terrain

The power spectral density plot of the loads obtained by the three combinations is shown by Figure 5. 13. It can be seen that in the low frequency range, the power spectrum magnitude of loads obtained by the three combinations are similar. As frequency increases, the load obtained by the Reference–Fastest method provides an over estimation the power spectrum magnitude compared to the Reference–Best method. The result agrees with the rainflow matrix plot shown in Figure 5. 11, as the numbers of cycles with relative high load amplitudes (> 1000 N) is considerably more than the corresponding number of cycles obtained from the reference load. The Proposed Method provides load with similar power spectral density curve with respect to the reference signal.

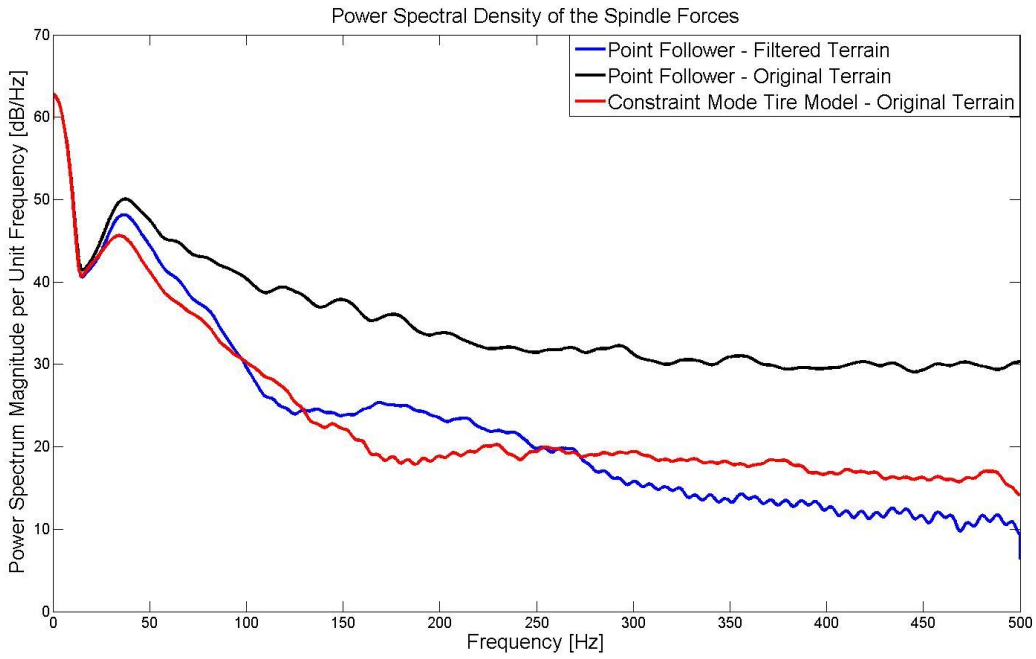

Figure 5. 13. Power Spectrum Density Plot of the loads obtained by the three combinations

The accumulated fatigue damage ratio of the Reference-Fastest (Point Follower with Unfiltered Terrain) and the Proposed Method (Point Follower with Pre-filtered Terrain) to the Reference-Best model is provided in Table 5. 3. The ratio obtained from Proposed Method is much closer to 100% than the ratio obtained from the Reference-Fastest technique. If fatigue damage predictions are generally considered acceptable when they are accurate to a factor of two (e.g., the estimated life is between 50% and 200% of the actual fatigue life), then the Proposed Method yields sufficiently accurate results, while the Reference-Fastest technique is not acceptable. The equivalent force amplitude ratio is also calculated and presented in Table 5. 3. The equivalent force ratio shows the Proposed Method performed as if the loads were predicted consistently at 95% of the Reference-Best loads. The Reference-Fastest technique performed as if the loads were predicted consistently at 30% above the Reference–Best loads. Therefore, it can be concluded that in these examples the terrain pre-filtering technique provides a very reliable terrain input to point-follower for spindle force prediction.

Table 5. 3. Accumulated Fatigue Damage and Average Force Amplitude Ratio for Rough Terrain

	Reference - Fastest	Proposed Method
Accumulated Fatigue Damage Ratio VS. Reference-Best	540%	70%
Equivalent Force Amplitude Ratio VS. Reference-Best	130%	95%

5.5 Case Study: Probabilistic Terrain

According to the stochastic gridding method developed in Chapter 2, a probabilistic terrain comprising a series of uniformly spaced nodes can be obtained from the measured cloud of terrain points. The node height is represented by a random variable instead of a deterministic value. The dependency relationship between the heights of adjacent nodes is provided by equation 3. 26. Different realizations can be generated as shown in Figure 5. 14. The variations between the realizations reflect the horizontal position uncertainties inherited from the measurement process.

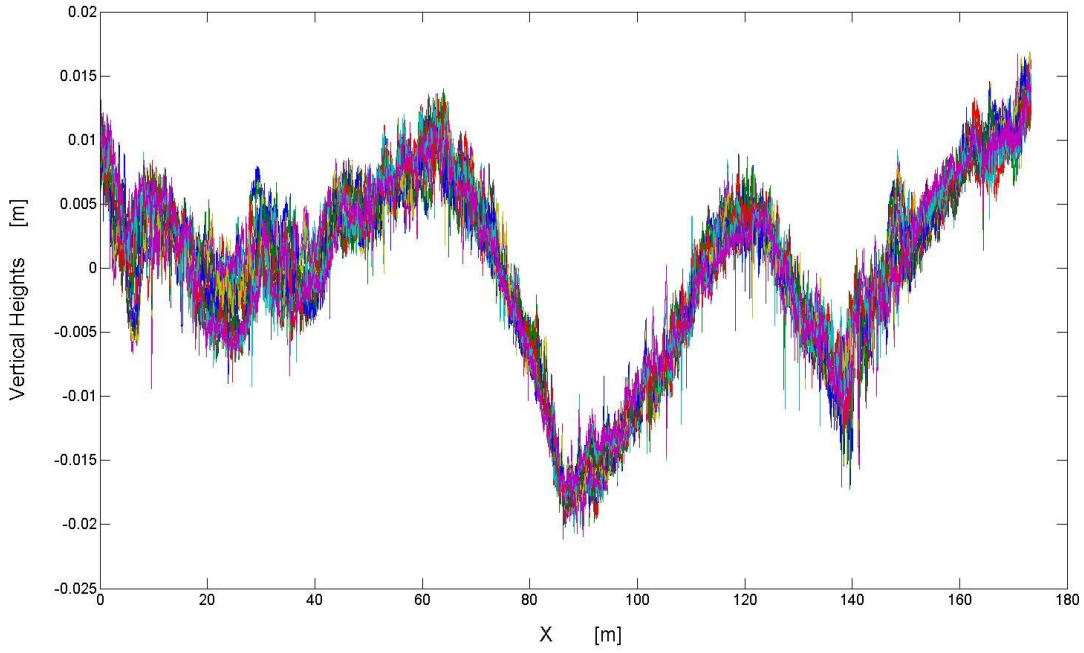

Figure 5. 14. Realizations of a Probabilistic Terrain

The three models shown as Table 5. 1 are simulated over all realizations. The variation between the realizations due to the measurement uncertainties results in the obtained spindle load variation. The consequent fatigue damage differences are expressed by an error bar plot given in Figure 5. 15. The horizontal length of the profile is divided into segments; each segment is 12.5 m. The fatigue damage of each loads corresponding to each segment is computed. The center of the bars represents the mean estimated pseudo-fatigue damage caused the corresponding section of different realizations. The range of the bars denotes the two standard deviations on each side. From the plot it can be seen that the pseudo-fatigue damage caused by the Reference–Best and Proposed Method share similar mean values, while the corresponding value obtained by Reference–Fastest method is noticeably higher. The ranges of the pseudo-fatigue damage obtained by Reference–Best and Proposed Method don't show a statistical difference, while the Reference–Fastest produces much wider ranges over all sections.

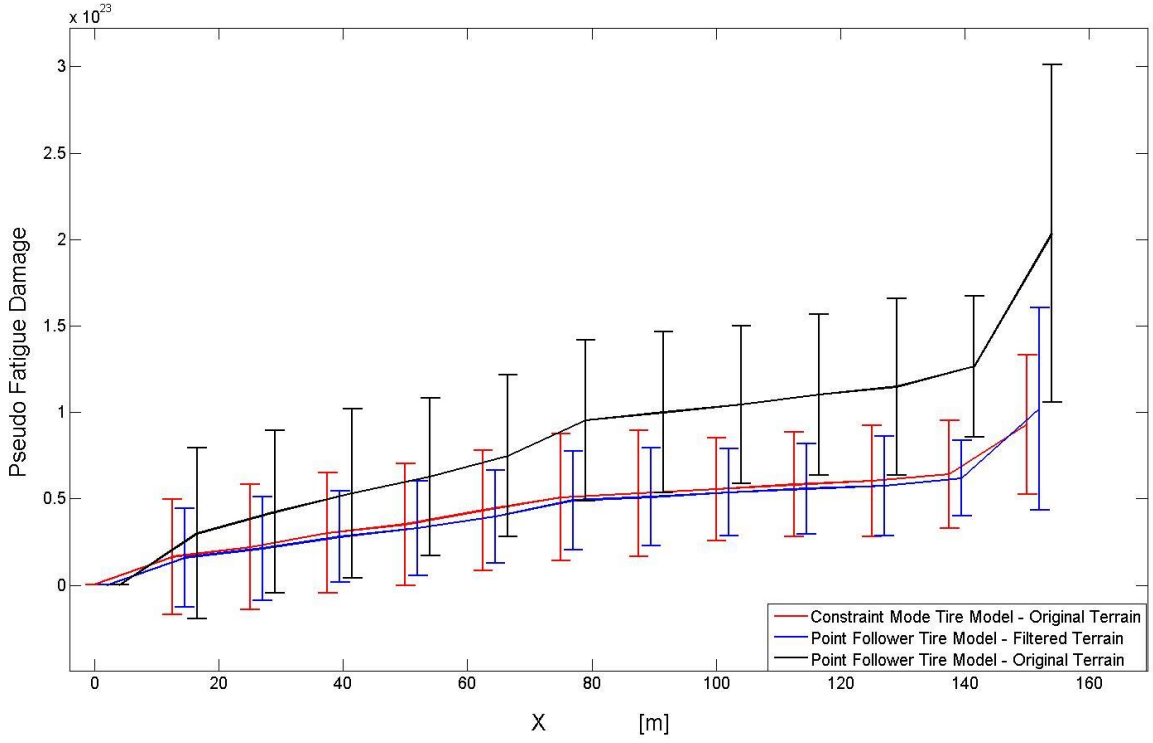

Figure 5. 15. Error bar plot of the fatigue damage variation obtained by three combinations

5.6 Computational Effort Analysis

For the case of the rough terrain, the computational time required to run each of the three modeling techniques on the same computer is shown in Table 5. 4. The reference for this computational efficiency comparison is the Reference-Fastest model. In this way, if the ratio is close to 100%, then the relative time required to simulate the model over this rough terrain using the Proposed Method or the Reference-Best method is close to the time required by the Reference-Fastest method. The most dramatic result is the savings in computational effort. The Reference-Best technique takes more than one thousand times longer to run than the Reference-Fastest technique, while the Proposed Method takes only slightly longer than the Reference-Fastest technique.

Table 5. 4. Ratio of Required Computation Time VS. Reference-Fastest

	Reference – Best	Proposed Method
Rough	120,000%	116%
Smooth	116,300%	103%

5.7. Conclusions

The conclusions from the two case studies in which the Proposed Method (pre-filtering the terrain surface data with a constraint-model tire model under static load conditions followed by simulating the dynamic vehicle model using a point-follower tire model) is used to efficiently predict the spindle loads is simple and dramatic. The Proposed Method can be used to accurately estimate the vehicle response with a tremendous increase in computational speed. These preliminary results show that spindle loads are predicted with 95% accuracy, yet computed 1000 times faster.

6. Conclusion and Future Work

6.1 Summary of Research

The vertical force generated from terrain-tire interaction has long been of interest for vehicle dynamic simulations and chassis development. As the terrain serves as the main excitation to the suspension system through pneumatic tire, proper terrain and tire models are required to produce reliable vehicle response. Due to the high complexity of the tire structure and the immense size of a high fidelity terrain profile, it is not efficient to calculate the terrain-tire interaction at every location. The use of a simpler tire model (e.g. a point-follower tire model) and a pre-filtered terrain profile as an equivalent input will considerably reduce the simulation time. The predicted responses would be nearly identical to those obtained using a complex tire model and unfiltered terrain, with a significant computational efficiency improvement. In this work, a terrain pre-filtering technique is developed to improve simulation efficiency while still providing reliable load prediction. The bridging and enveloping properties are addressed in the pre-filtered terrain profile instead of the tire model. The work is divided into three parts: Terrain, Tire model and the terrain pre-filtering technique development based on the tire model.

First a stochastic gridding method is developed to include the measurement uncertainties in the gridded terrain profile used as input to the vehicle simulation. The gridded terrain profile is composed of a series of nodes, whose heights are evaluated at the surrounding measured terrain points. Each terrain point is assigned a weighting function according to its position relative to the grid node being considered. Empirical Cumulative Distribution Functions are developed based on the weighting function to define the distribution of the nodal height as a random variable and the dependence relationship between adjacent nodes. The obtained uniformly spaced terrain profile with node heights as random variables is considered probabilistic terrain and different realizations can be generated.

Next, a constraint mode tire model is developed to emulate the tire radial displacement and the corresponding force given the terrain excitation. The tire is modeled by a discrete flexible ring and

Hamilton's Principle is applied to derive the equation of motion. The model parameters are reduced to two sets: two shape parameters and one overall stiffness factor. A system identification process to determine the shape parameters through cleat testing is proposed. The stiffness factor can be calculated by an optimization process with respect to the experimental data of a flat plate test. The bridging and enveloping properties of the model are validated over bumps and cracks. The calibrated model is validated against a cleat test result in terms of the ability to provide accurate force prediction. The constraint mode tire model provides a simple and accurate method to emulate the tire radial displacement with respect to terrain excitation, as well as the corresponding force.

Finally, the pre-filtering technique is developed based on the calibrated constraint mode tire model. At each location along the tire's path, the tire center height is adjusted until the spindle load reaches a pre-designated constant load. The resultant tire center trajectory is the pre-filtered terrain profile and serves as an equivalent input to the simple tire model, with the tire bridging and enveloping properties addressed. The vehicle response produced by using the pre-filtered terrain profile and the simple tire model is analyzed for accuracy assessment by a pseudo-fatigue damage measure. The computational efficiency improvement is also examined. With different terrain profile realizations as the original terrain inputs, the effectiveness of the pre-filtering technique can be valid on the probabilistic terrain as well. The pre-filtering technique is demonstrated to significantly improve the simulation efficiency, with acceptable accuracy loss.

6.2 Recommended Future Work

The future work that are out of the scope of this work, but would produce other novel and useful contributions to the field include the following.

- **The choice of *n* in the weighting function used for the stochastic gridding process**

  As shown in the discussion section in chapter 3, the Cumulative Distribution Function as a stochastic description of the nodal height random variable is determined by the assigned weighting functions of surrounding terrain points. The weighting function contains a user defined parameter *n*. As different applications addresses various concern with the horizontal measurement uncertainty, the value of *n* can be adjusted according to the user requirement. The relationship between the generated realizations of the terrain profile and the value of *n* can be further analyzed.

- **Simplification of the system identification process of the constraint mode tire model**

  Chapter 4 shows the system identification process of the constraint mode tire model is divided into two parts: a cleat test to determine the shape parameters and a flat plate test for the overall stiffness factor. Future research can focus on simplifying the process by eliminating the cleat test, and determine all the parameters from the flat plate test data alone.

- **Scalability of the constraint mode tire model to tires with different sizes**

  As shown in Chapter 4, the constraint mode tire model parameters k_0, α_1 and α_2 of are dependent on the size. Therefore if the model is applied on a tire with a different size, the parameters need to be recalibrated. To easily apply the model for tires with different sizes and, future research will focus on the scalability of the model parameters with respect to the tire size. Therefore if the tire sized changes, the model parameters can be easily obtained without recalibration process.

- **Extend the in-plane tire model to out-of-plane model with steering effect**

  The constraint mode tire model developed in this work provides an in-plane tire model for tire-road interaction analysis. Therefore only the vertical force can be predicted through the in-plane radial deformation. Due to its simplicity, the model is not able to provide lateral force prediction. The future work will extend this model to a three dimensional model. Therefore the model can be used for more accurate and complete vehicle dynamic simulation, with steering effect included.

References

1. Duni, E., et al., Vehicle Fatigue Load Prediction based on Finite Element Tire/Road Interaction implemented in an Integrated Implicit-Explicit Approach, in 2008 Abaqus Users' Conference2008. p. 16.

2. Lei, G. and R.J. Yang, On reliability-based optimisation methods for automotive structures. International Journal of Materials & Product Technology, 2006. 25(1-3): p. 3-26.

3. Lu, M.-W. and Y.-L. Lee. Reliability based strength/fatigue design criteria. in Proceedings of the Annual Reliability and Maintainability Symposium. 1996. Piscataway, NJ, USA: IEEE.

4. Michelberger, P. and I. Zobory. Loading conditions of ground vehicles in operation. Analysis of load history. in American Society of Mechanical Engineers, Applied Mechanics Division, AMD. 1990. New York, NY, USA: Publ by ASME.

5. Stadterman, T.J., et al., Dynamic modeling and durability analysis from the ground up. Journal of the IEST, 2003. 46: p. 128-34.

6. Wang, C.J. and D.C. Baker. Reliability analysis of data with no failure from fleet and proving ground endurance tests. 1992. Warrendale, PA, USA: Publ by SAE.

7. Aurell, J. and S. Edlund, Operating Severity Distribution - A Base for Vehicle Optimization. 11th International Association of Vehicle System Dynamics Symposium (IAVSD 1989), 1989. 18: p. 42-56.

8. Gillespie, T.D., M.W. Sayers, and L. Segel, Calibration of Response-Type Road Roughness Measuring Systems. International Journal of Materials and Product Technology, 1980: p. 453-461.

9. Hveem, F.N., Devices for Recording and Evaluating Pavement Roughness, 1960, Highway Research Board Bulletin 264. p. 1-26.

10. Dembski, N., G. Rizzoni, and A. Soliman. Development of a terrain severity measurement system utilizing optical lasers. in Modeling and Simulation for Military Applications. 2006. Orlando (Kissimmee), FL, USA: SPIE.

11. Dembski, N., et al. The development of a terrain severity measurement system. 2006. New York, NY 10016-5990, United States: American Society of Mechanical Engineers.

12. Kern, J.V. and J.B. Ferris, Development of a 3-D Vehicle-Terrain Measurement System Part I: Equipment Setup, in ISTVS: Innovations in Terrain and Vehicle Systems2007, ISTVS: Fairbanks, AK.

13. Liu, F., et al. A Kalman-filter-based multi-sensor terrain profile measurement system: principle, implementation and validation. in Modeling and Simulation for Military Operations III. 2008. Orlando, FL, USA: SPIE.

14. Wagner, S.M., et al., Development of a 3-D Vehicle-Terrain Measurement System Part II: Signal Processing and Validation, in ISTVS: Innovations in Terrain and Vehicle Systems2007, ISTVS: Fairbanks, AK.

15. Chaika, M., D. Gorsich, and T.C. Sun, Some statistical tests in the study of terrain modelling. International Journal of Vehicle Design, 2004. 36(2): p. 132-148.

16. Spangler, E.B. and W.J. Kelly, GMR Road Profilometer-A Method for Measuring Road Profile, 1966, Highway Research Board 121. p. 27-54.

17. Prem, H., A Laser-Based Highway-Speed Road Profile Measuring System, in 10th International Association for Vehicle System Dynamics (IAVSD 1987), Symposium on The Dynamics of Vehicles on Roads and on Tracks 1987: Prague, Czechoslovakia.

18. Ma, R., Chemistruck, Heather., Ferris, John B.. State-of-the-art of terrain profile characterization models. International Journal of Vehicle Design, 2013. 61(1-4): p. 285 - 304 (20).

19. Herr, W.J., Highway Profile Measuring System, 1996: United States of America.

20. Smith, H. and J.B. Ferris. Excitation Event Design and Accuracy Verification Procedure for High Fidelity Terrain Measurement Systems. in Submitted to the SPIE. 2009. Orlando, FL.

21. Detweiler, Z.R. and J.B. Ferris. Uniform Grid Spacing for Three Dimensional High Fidelity Terrain Profiles. in 16th International Conference of the International Society for Terrain-Vehicle Systems. 2008. Turin, Italy.

22. Detweiler, Z.R. and J.B. Ferris, Interpolation methods for High-fidelity three dimensional terrain surfaces. Journal of Terramechanics, 2009.

23. Yanalak, M., Effect of Gridding method on digital terrain model profile data based on scattered data. Journal of Computing in Civil Engineering, 2003. 17(1): p. 58-67.

24. Umsrithong, A., Deterministic and Stochastic Semi-Empirical Transient Tire Models, in Mechanic Engineering2012, Virginia Tech: Blacksburg, VA, USA.

25. Bandel, P.M., C., Simulation model of the dynamic behavior of a tire running over an obstacle. Tire Science and Technology, TSTCA, 1988. 16(2).

26. Zegelaar, P.W.A., The dynamic response of tyres to brake torque variations and road unevennesses, 1998, Delft University of Technology: Netherlands. p. 315.

27. Zegelaar, P.W.A., Pacejka, H. B., The In-plane Dynamics of Tyres on Uneven Roads. Vehicle System Dynamics, 1996: p. 714-730

28. Loo, M., A Model Analysis of Tire Behavior under Vertical Loading and Straight-Line Free Rolling. Tire Science and Technology, 1985. 13(2): p. 67-90.

29. Badalamenti, J.M.D., G. R., Radial-interradial Spring Tire Models, Acoustic, Stress and Reliability in Design. Journal of Vibration, 1988. 110(1): p. 70-75.

30. Gillespie, T.D., Fundamentals of Vehicle Dynamics1992, Warrendale, PA: Society of Automotive Engineers, Inc.

31. Takayama, M.Y., K., Simulation Model of Tire Vibration. Tire Science and Technology, 1984. 11(1): p. 38 – 49.

32. Ferris, J.B., Capturing Planer Tire Enveloping Properties Using Static Constraint Modes, in ASME 2006 International Mechanical Engineering Congress and Exposition (IMECE2006), Dynamic Systems and Control Division 2006: Chicago, Illinois, USA p. IMECE2006-15260 pp. 467-472

33. Guyan, R.J., Reduction of Stiffness ans Mass Matrices. AIAA Jounrnal, 1965. 3(2): p. 380.

34. Guo, K.L., Qing, A Model of Tire Enveloping Properties and its Application on Modeling of Automotive Vibration System. SAE paper, 1998(980253).

35. Serra Jean C., Image analysis and mathematical morphology1983, Orlando, FL, USA: Academic Press, Inc. .

36. Zhang, X., The improvement of the in-plane UniTire Durabiltiy model and the realization in Carsim, 2010, Jinlin University: Changchun, China.

37. Pacejka, H.B., Tire and Vehicle Dynamics2006: Society of Automotive Engineers.

38. Schmeitz, A.J.C., Pacejka H.B., A Semi-Empirical Three-Dimensional Model of the Pneumatic Tyre Rolling over Arbitrarily Uneven Road Surfaces, 2004, TU Delft.

39. Chul, K. and P.I. Ro, An accurate full car ride model using model reducing techniques. Transactions of the ASME. Journal of Mechanical Design, 2002. 124(4): p. 697-705.

40. Müller, T., Ferris, J., Detweiler, Z., and Smith, H., Identifying Vehicle Model Parameters Using Measured Terrain Excitations. SAE Technical Paper, 2009. 2009-01-1197.

41. Ma, R. and J.B. Ferris, Terrain gridding using a stochastic weighting function, in ASME 2011 Dynamic Systems and Control Conference and Bath/ASME Symposium on Fluid Power and Motion Control (DSCC2011) 2011: October 31–November 2, 2011 , Arlington, Virginia, USA p. 375-381

42. Blerman, G.S., Error Modeling for Differential GPS, in Aeronautics and Astronautics1995, Massachusetts Institute of Technology: Boston.

43. Moon, T.K., Mathematical methods and algorithms for signal processing. Todd K. Moon ; Wynn C. Sterling, ed. W.C. Sterling2000. XXXVI, 937 S.

44. Lee, R.C., Stochastic Terrain and Soil Modeling for Off-Road Mobility Studies, in Mechanical Engineering 2009, Virginia Tech: Blacksburg, Virginia, USA.

45. Ma, R., A.A. Reid, and J.B. Ferris, Capturing Plannar Tire Properties Using Static Constraint Modes, in Dynamic Systems and Control Conference and Bath/ASME Symposium on Fluid Power and Motion Control2012: Ft. Lauderdale, FL.

46. Golub, G.H.V.L., Charles F., Matrix Computations Vol. 4.7.7 Circulant Systems. 1996: Johns Hopkins.

47. Joseph, E.S., Charles, R.M., Richard, G.B., Mechanical Engineering Design2003, New York: McGraw-Hill.

Appendix

Disclaimer

Reference herein to any specific commercial company, product, process, or service by trade name, trademark, manufacturer, or otherwise, does not necessarily constitute or imply its endorsement, recommendation, or favoring by the United States Government or the Department of the Army (DoA). The opinions of the authors expressed herein do not necessarily state or reflect those of the United States Government or the DoA, and shall not be used for advertising or product endorsement purposes.

Section 1. Derivation of Circulant Matrix Inverse

For a circulant matrix $[\boldsymbol{\alpha}]$, with $\{a_i\} = [\ a_0 \quad a_1 \quad a_2 \quad \dots \quad a_{n-1}]$ as the characterization vector, the eigenvalue of $[\boldsymbol{\alpha}]$ can be obtained by Discrete Fourier Transform to the vector $\{a_i\}$ as equation A1. 1.

$$\{\lambda_k\} = \mathcal{F}(\{a_i\}) \qquad \text{A1. 1}$$

$$\lambda_k = \sum_{i=0}^{n-1} a_i W_k^i \qquad k = 0,1,2,\dots,n-1$$

$$W_k = e^{-\frac{2\pi k}{n}j}$$

W_k is the k^{th} frequency component. If $k=0$, the corresponding frequency component is a constant.

$$W_k^0 = e^0 = 1 \qquad \text{A1. 2}$$

The frequency component can be expanded with Euler Formula as equations A1. 3.

$$W_k^i = e^{-\frac{2\pi ki}{n}j} = cos\left(-\frac{2\pi ki}{n}\right) + jsin\left(-\frac{2\pi ki}{n}\right) = cos\left(\frac{2\pi ki}{n}\right) - jsin\left(\frac{2\pi ki}{n}\right) \qquad \text{A1. 3}$$

$$W_k^{n-i} = e^{-\frac{2\pi k(n-i)}{n}j} = cos\left(-\frac{2\pi k(n-i)}{n}\right) + jsin\left(-\frac{2\pi k(n-i)}{n}\right)$$

$$= cos\left(\frac{2\pi ki}{n}\right) + jsin\left(\frac{2\pi ki}{n}\right)$$

With the value of terms in the characterization vector $a_0 = 1, a_1 = a_{n-1} = \alpha_1, a_2 = a_{i-2} = \alpha_2, a_3 = a_4 = \cdots = a_{i-3} = 0$, the eigenvalue can be simplified by substituting A1. 3 into equation A1. 1.

$$\lambda_k = a_0 W_0 + a_1 W_1 + a_2 W_2 + 0 + \cdots + 0 + a_{n-2} W_{n-2} + a_{n-1} W_{n-1} \quad \text{A1. 4}$$

$$= 1 + \alpha_1 \left[cos\left(\frac{2\pi k}{n}\right) + jsin\left(\frac{2\pi k}{n}\right) \right]$$

$$+ \alpha_2 \left[cos\left(\frac{4\pi k}{n}\right) - jsin\left(\frac{4\pi k}{n}\right) \right] + \alpha_2 \left[cos\left(\frac{4\pi k}{n}\right) + jsin\left(\frac{4\pi k}{n}\right) \right]$$

$$+ \alpha_1 \left[cos\left(\frac{2\pi k}{n}\right) - jsin\left(\frac{2\pi k}{n}\right) \right]$$

$$= 1 + 2\alpha_1 cos\left(\frac{2\pi k}{n}\right) + 2\alpha_2 cos\left(\frac{4\pi k}{n}\right)$$

By double angle formula, the eigenvalue can be rewritten as equation A1. 5.

$$\lambda_k = 4\alpha_2 cos^2\left(\frac{2\pi k}{n}\right) + 2\alpha_1 cos\left(\frac{2\pi k}{n}\right) + 1 - 2\alpha_2 \quad \text{A1. 5}$$

From equation A1. 5, it can be shown that the eigenvalue is symmetric except the first one as shown by equation A1. 6.

$$\lambda_{n-k} = 4\alpha_2 cos^2\left(\frac{2\pi(n-k)}{n}\right) + 2\alpha_1 cos\left(\frac{2\pi(n-k)}{n}\right) + 1 - 2\alpha_2 = \lambda_k$$
$$k = 0,1,2,\ldots,n-1 \quad \text{A1. 6}$$

$$\lambda_0 = 1 + 2\alpha_1 + 2\alpha_2$$

$\{\beta_i\}$ denotes the characteristic vector of the inverse shape matrix $[\boldsymbol{\alpha}]^{-1}$. It can be obtained by performing an Inverse Discrete Fourier Transform on the eigenvalues of $[\boldsymbol{\alpha}]^{-1}$, i.e. $\left\{\frac{1}{\lambda_i}\right\}$. The characteristic vector $\{\beta_i\}$ can be computed as equation A1. 7

$$\beta_k = \frac{1}{n}\sum_{i=0}^{n-1}\frac{1}{\lambda_i}W_k^{-i} \qquad k = 0,1,2,\dots,n-1 \tag{A1. 7}$$

The first term β_0 can be computed as equation A1. 8.

$$\beta_0 = \frac{1}{n}\sum_{i=0}^{n-1}\frac{1}{\lambda_i}W_0^{-i} = \frac{1}{n}\sum_{i=0}^{n-1}\frac{1}{\lambda_i} \tag{A1. 8}$$

The rest terms of $\{\beta_i\}$ denoted by β_k can be expanded as equation A1. 9.

$$\beta_k = \frac{1}{n}\left[\frac{1}{\lambda_0}W_k^0 + \frac{1}{\lambda_1}W_k^{-1} + \cdots + \frac{1}{\lambda_{n-1}}W_k^{-(n-1)}\right] \tag{A1. 9}$$

$$k = 1,2,\dots,n-1$$

The symmetric term β_{n-k} can be expanded as equation A1. 10

$$\beta_{n-k} = \frac{1}{n}\left[\frac{1}{\lambda_0}W_{n-k}^0 + \frac{1}{\lambda_1}W_{n-k}^{-1} + \cdots + \frac{1}{\lambda_{n-1}}W_{n-k}^{-(n-1)}\right] \tag{A1. 10}$$

$$k = 1,2,\dots,n-1$$

From equation A1. 3, the property shown as equation A1. 11 can be obtained.

$$W_{n-k}^{-i} = W_k^{-(n-i)} \qquad i = 0,1,2,\dots,n-1,\ \ k = 0,1,2,\dots,n-1 \tag{A1. 11}$$

$$W_{n-k}^{-i} = cos\left(\frac{-2\pi(n-k)i}{n}\right) - jsin\left(\frac{-2\pi(n-k)i}{n}\right) = cos\left(\frac{2\pi ki}{n}\right) - jsin\left(\frac{2\pi ki}{n}\right)$$

$$W_k^{-(n-i)} = cos\left(\frac{-2\pi k(n-i)}{n}\right) - jsin\left(\frac{-2\pi k(n-i)}{n}\right)$$

$$= cos\left(\frac{2\pi ki}{n}\right) - jsin\left(\frac{2\pi ki}{n}\right)$$

Combine equation A1. 6 with equation A1. 11, the equality shown as A1. 12 can be obtained.

$$\frac{1}{\lambda_{n-k}} W_{n-k}^{-i} = \frac{1}{\lambda_k} W_k^{-(n-i)} \qquad \text{A1. 12}$$

$$i = 0,1,2,\dots,n-1, \quad k = 0,1,2,\dots,n-1$$

Therefore the terms of the characteristic vector $\{\beta_i\}$ is symmetric except the first term, as shown by equation A1. 13.

$$\beta_k = \beta_{n-k} \qquad \text{A1. 13}$$

$$k = 1,2,\dots,n-1$$

It can be seen that the reformatted eigenvalue shown by equation A1. 5 possesses a parabola form, by using a substituting lumped parameter as equation A1. 14.

$$\lambda_k(\xi) = 4\alpha_2\xi^2 + 2\alpha_1\xi + 1 - 2\alpha_2 \qquad \xi \in [-1,1] \qquad \text{A1. 14}$$

$$\xi = cos\left(\frac{2\pi k}{N}\right) \quad k = 0,1,2 \dots n-1$$

The second derivative of the parabola indicates the concavity of the eigenvalue as ξ changes. Due to the physical constraint applied in 4. 35, the value of α_2 is positive. Therefore the second derivative of the eigenvalue function is positive as shown by A1. 15. Therefore the parabolic curve of $\lambda_k(\xi)$ faces upwards

$$\frac{d^2(\lambda_k(\xi))}{dx\xi^2} = 8\alpha_2 > 0 \qquad \text{A1. 15}$$

The symmetry axis can be found by equation A1. 16.

$$\frac{d(\lambda_k(\xi))}{d\xi} = 8\alpha_2\xi + 2\alpha_1 = 0 \qquad \text{A1. 16}$$

$$\xi = -\frac{\alpha_1}{4\alpha_2}$$

As the parabola curve facing upwards, it corresponding to the minimum value of $\lambda_k(\xi)$ represented as A1. 17.

$$\lambda_k\left(\xi = -\frac{\alpha_1}{4\alpha_2}\right) = \alpha_2\xi^2 + 2\alpha_1\xi + 1 - 2\alpha_2 = \frac{16\alpha_2(1-2\alpha_2) - 4\alpha_1^2}{16\alpha_2^2} = -\frac{\Delta}{16\alpha_2^2} \qquad \text{A1. 17}$$

It can be seen that if the determinant is Δ less than zero, the minimum value of $\lambda_k(\xi)$ is larger than zero. Therefore in this case the value of $\lambda_k(\xi)$ is always larger than zero, regardless of the ξ value.

Section 2. Equation of Motion – 7 Degree of Freedom Vehicle Model

Vertical motion of the sprung mass:

$$m_s\ddot{x}_s + c_f(\dot{z}_{s,fr} - \dot{z}_{u,fr}) + c_f(\dot{z}_{s,fl} - \dot{z}_{u,fl}) + c_r(\dot{z}_{s,rr} - \dot{z}_{u,rr}) + c_r(\dot{z}_{s,rl} - \dot{z}_{u,rl}) + k_f(z_{s,fr} - z_{u,fr}) + k_f(z_{s,fl} - z_{u,fl}) + k_r(z_{s,rr} - z_{u,rr}) + k_r(z_{s,rl} - z_{u,rl}) + m_s g = 0 \quad \text{A2. 1}$$

Pitch motion

$$I_p\ddot{\theta}_s + c_f a(\dot{z}_{s,fr} - \dot{z}_{u,fr}) + c_f a(\dot{z}_{s,fl} - \dot{z}_{u,fl}) - c_r b(\dot{z}_{s,rr} - \dot{z}_{u,rr}) - c_r b(\dot{z}_{s,rl} - \dot{z}_{u,rl}) + k_f a(z_{s,fr} - z_{u,fr}) + k_f a(z_{s,fl} - z_{u,fl}) - k_r b(z_{s,rr} - z_{u,rr}) - k_r b(z_{s,rl} - z_{u,rl}) = 0 \quad \text{A2. 2}$$

Roll motion

$$I_r\ddot{\phi}_s + c_f t_f(\dot{z}_{s,fr} - \dot{z}_{u,fr}) - c_f t_f(\dot{z}_{s,fl} - \dot{z}_{u,fl}) + c_r t_r(\dot{z}_{s,rr} - \dot{z}_{u,rr}) - c_r t_r(\dot{z}_{s,rl} - \dot{z}_{u,rl}) + k_f t_f(z_{s,fr} - z_{u,fr}) - k_f t_f(z_{s,fl} - z_{u,fl}) + k_r t_r(z_{s,rr} - z_{u,rr}) - k_r t_r(z_{s,rl} - z_{u,rl}) = 0 \quad \text{A2. 3}$$

Vertical motion of the unsprung masses

$$m_{u,f}\,\ddot{z}_{u,fr} - c_f(\dot{z}_{s,fr} - \dot{z}_{u,fr}) - k_f(z_{s,fr} - z_{u,fr}) + F_{t,fr} + m_{u,f} g = 0 \quad \text{A2. 4}$$

$$m_{u,f}\,\ddot{z}_{u,fl} - c_f(\dot{z}_{s,fl} - \dot{z}_{u,fl}) - k_f(z_{s,fl} - z_{u,fl}) + F_{t,fl} + m_{u,f} g = 0$$

$$m_{u,r}\,\ddot{z}_{u,rr} - c_r(\dot{z}_{s,rr} - \dot{z}_{u,rr}) - k_r(z_{s,rr} - z_{u,rr}) + F_{t,rr} + m_{u,r} g = 0$$

$$m_{u,t}\,\ddot{z}_{u,rl} - c_r\left(\dot{z}_{s,rl} - \dot{z}_{u,rl}\right) - k_r\left(z_{s,rl} - z_{u,rl}\right) + F_{t,rl} + m_{u,r}g = 0$$

Sprung mass to the motions on each of the four corners.

$$\dot{z}_{s,fr} = \dot{z}_s + a\dot{\theta}_s + t_f\dot{\Phi}_s \qquad \text{A2. 5}$$

$$\dot{z}_{s,fl} = \dot{z}_s + a\dot{\theta}_s - t_f\dot{\Phi}_s$$

$$\dot{z}_{s,rr} = \dot{z}_s - b\dot{\theta}_s + t_r\dot{\Phi}_s$$

$$\dot{z}_{s,rl} = \dot{z}_s - b\dot{\theta}_s - t_r\dot{\Phi}_s$$

Balance the displacement at each of the four corners.

$$z_{s,fr} = z_s + a\theta_s + t_f\Phi_s \qquad \text{A2. 6}$$

$$z_{s,fl} = z_s + a\theta_s - t_f\Phi_s$$

$$z_{s,rr} = z_s - b\theta_s + t_r\Phi_s$$

$$z_{s,rl} = z_s - b\theta_s - t_r\Phi_s$$